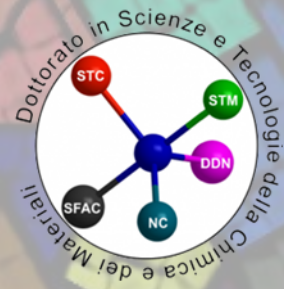




UNIVERSITÀ DEGLI STUDI
DI GENOVA



ISTITUTO ITALIANO
DI TECNOLOGIA



Magnetic nanoparticles for brain diseases

Doctoral Thesis presented by

Niccolò Silvestri

Supervisors:

Dr. Teresa Pellegrino

Prof. Annalisa Relini

Declaration

This dissertation is the result of my own work and includes nothing, which is the outcome of work done in collaboration except where specifically indicated in the text. It has not been submitted, in part or completely, to any university or institution of any degree, diploma, or other qualification.

DATE:

14th of April 2019

Niccolò Silvestri


A handwritten signature in black ink, appearing to read 'Niccolò Silvestri', written in a cursive style.

Table of Contents

| | |
|--|----|
| Thesis abstract..... | 1 |
| Introduction..... | 3 |
| 1. The role of magnetic nanoparticles in nanomedicine | 3 |
| 2. Nanoparticles for neurodegenerative diseases and the importance to overcome the Blood Brain Barrier | 6 |
| References..... | 9 |
| Chapter 1 Synthesis and characterization of divalent metal ions substituted ferrite nanocubes..... | 15 |
| 1.1 Introduction..... | 15 |
| Basis of nanomagnetism | 15 |
| Hyperthermia: using MNPs for heat generation | 19 |
| Magnetic resonance imaging (MRI): using MNPs as image contrast agents | 22 |
| MPI: using MNPs as image tracer | 24 |
| Improving the magnetic properties of MNPs..... | 26 |
| 1.2 Results and discussion | 29 |
| 1.2.1 Optimization of CoFeNCs synthesis..... | 29 |
| 1.2.2 Water transfer of CoFeNCs with polymer coating technique..... | 31 |
| 1.2.3 SAR characterization & AC Hysteresis loops of CoFeNCs | 34 |
| 1.2.4 CoFeNCs in Matrigel environment: simulation of a tumor injection | 35 |
| 1.2.5 Synthesis of Zinc ferrite nanocubes | 38 |
| 1.2.6 Synthesis of zinc-cobalt ferrite and manganese-cobalt ferrite nanocubes | 39 |
| 1.2.7 Structural and magnetic characterization..... | 43 |
| 1.2.8 SAR and AC magnetic measurements | 48 |
| 1.2.9 SAR and AC magnetic measurements of the ferrite nanocubes in viscous media .. | 51 |
| 1.2.10 Automatized synthesis of MNBs: large scale synthesis | 53 |
| 1.2.11 SAR and AC magnetic measurements of MNBs | 54 |
| 1.2.12 Relaxivity characterization | 56 |
| 1.2.13 Relaxometry measurements for MPI imaging application | 57 |
| 1.2.14 Cytotoxicity of the nanocubes | 60 |
| 1.3 Conclusions and outlook..... | 62 |
| 1.4 Experimental section..... | 63 |
| 1.5 References..... | 71 |

| | |
|--|-----|
| Chapter 2. Nanocubes for Blood Brain Barrier transportation and neurodegenerative diseases treatment | 79 |
| 2.1 Introduction..... | 79 |
| 2.1.1 Neurodegenerative Brain diseases | 79 |
| 2.1.2 Blood Brain Barrier..... | 82 |
| 2.1.3 Nanoparticles: brain drug delivery..... | 83 |
| 2.2 Results and discussions..... | 86 |
| 2.2.1 Nanoparticles for BBB permeation study | 86 |
| 2.2.2 PEG functionalization..... | 88 |
| 2.2.4 TAT functionalization..... | 89 |
| 2.2.5 BBB model study..... | 90 |
| 2.2.6 Main features affecting NPs transportation through the BBB..... | 92 |
| MNP's coating..... | 92 |
| MNP's composition..... | 93 |
| 2.2.7 NPs passage across the BBB..... | 95 |
| 2.2.8 Evaluation of BBB recovery..... | 98 |
| 2.2.9 Insulin fibrils degradation by Ferulic acid | 99 |
| 2.3 Conclusion and outlook | 101 |
| 2.4 Experimental section..... | 102 |
| 2.5 References..... | 109 |
| Appendix..... | 116 |
| List of abbreviations | 122 |
| Acknowledgements..... | 126 |
| Curriculum vitae | 127 |

Thesis abstract

The present dissertation presents my doctoral work developed during the last three years at the Italian Institute of Technology (IIT) and the University of Genoa. The work was focused on the development of different ferrite nanoparticles and their magnetic characterization. Another objective of this work was the use of these magnetic nanoparticles for magnetic hyperthermia as a suitable mean to enhance the blood brain barrier passage.

The first chapter deals with the synthesis and characterization of different divalent ions substituted ferrite nanocubes (NCs). In particular, through non-hydrolytic synthesis, cobalt ferrite, zinc ferrite and mixed ferrite NCs, *i.e.* cobalt-manganese and cobalt-zinc, were obtained. The size and the composition were controlled by modifying the synthesis parameters, obtaining cubic-shaped nanoparticles with a cube edge ranging from 5 nm to 65 nm at different ions stoichiometry. The full characterization of these NCs was carried out to find the combination of composition and size that better suits their application in magnetic hyperthermia treatment (MHT), magnetic resonance imaging (MRI) and magnetic particle imaging (MPI). Additionally, their use to prepare magnetic clusters by controlling the aggregation of these nanocubes into polymeric beads, here named magnetic nanobeads, was also studied. In chapter 1 is shown that these nanocubes, especially cobalt ferrite and zinc ferrite, revealed outstanding heating properties in magnetic hyperthermia. The same nanocubes were showing good performances as MRI contrast agent and generates MPI signals that were better than commercially available Resovist magnetic nanoparticles. Thanks to the large portfolio of NCs here prepared, it was possible to correlate their structural and chemical properties to the hysteresis loops measured under alternating magnetic field (AMF), probing heat losses as a function of media viscosity, concentration and aggregation status. The results obtained revealed that among all the different compositions, the zinc ferrite NCs are the most promising material for MHT, MPI and MRI applications, thanks also to his biocompatibility.

In the second chapter, the functionalization and the exploitation of magnetic nanoparticles for enhancing central nervous system delivery is reported. In particular, the main goal of this study was to increase the NCs transportation through the blood-brain barrier (BBB) for the treatment of neurodegenerative diseases and brain tumors by using magnetic hyperthermia and molecular targeting. To reach this scope two strategies were followed. The first approach consists on the

temporary and local damage of the BBB driven by the heat properties of the iron oxide and cobalt ferrite NCs thus increasing the para-cellular transportation through the BBB. The second approach consists on the functionalization of the same NCs with the trans-activating transcriptional activator peptide (TAT) to enhance the trans-cellular transportation through the BBB. The experiments were carried on a functional *in vitro* model of BBB using bEnd3 cells. First a suitable coating for the nanoparticles was developed. The results showed the importance of coating the NPs with polyethylene glycol (PEG) to increase the stability in biological media, enhancing the passive passage through the BBB. Then, the heating performances of both iron oxide and cobalt ferrite NCs were compared to induce thermal damage to the BBB. Due to their ability to heat up using lower NPs dose, cobalt ferrite NCs were chosen over iron oxide ones for further studies. The experiments of BBB transportation of these nanoparticles in presence of magnetic hyperthermia revealed a double fold dose increase in the passage when the barrier was thermally damaged. Nevertheless, the complete recovery from the temporarily induced damage was demonstrated. Concerning the second BBB transportation approach, the TAT coated NPs were successfully prepared. Further experiments will be done to test them on the BBB model. Finally, being most of the neurodegenerative disorders characterized by peptide fibrils accumulation in to the brain, a preliminary study focused on the use of Ferulic acid (FA) as a potential compound for disassembling aggregated insulin fibrils in a protein plaque model was followed. The effect of the FA on the fibrils was found to be concentration dependent, increasing with the increase of compound concentration. Further studies should be done to delivery this compound to the brain.

Introduction

1. The role of magnetic nanoparticles in nanomedicine

Nanomedicine that makes use of nanoparticles/nanostructures for medical purposes, is gaining great interest in the scientific community. These nanosystems can be engineered to possess various functions, making them potentially useful as multi-purposes nano-tools for medical applications.¹ The class of nanomaterials is very broad and includes many inorganic nanoparticles (*e.g.* gold,² silica,³ iron oxide,⁴ silver⁵ or semi-conducting materials⁶), and organic based nanomaterials (*e.g.* lipid nanoparticles⁷, polymeric nanoparticles⁸, dendrons⁹ etc.). The nanomaterials have tunable sizes ranging from a few nanometers up to tens of nanometers which place them at a scale smaller or comparable to those of a cell (10–100 μm), a virus (20–450 nm), a protein (5–50 nm) or a gene (2 nm wide and 10–100 nm long).¹⁰ Their surface is normally coated with polymers or bioactive molecules for improved biocompatibility¹¹, selective targeting of biologic molecules^{12,13} and cells recognition.^{14–16} In the nanomedicine scenario, magnetic nanoparticles (MNPs) became interesting thanks to their physical properties.¹⁷ First, a fundamental feature of the MNPs is their large ratio of surface area to volume, which can be orders of magnitude greater than that of bulk materials.¹⁸ When the particles size decreases, the number of surface atoms become larger with respect to the total number of atoms constituting the NP, which implies that surface and interface effects become more important affecting NPs interactions.^{19,20} Moreover, having higher surface area available per nanoparticle, even the loading efficiency with payloads molecules such as drugs becomes significantly higher than larger carriers, such as micrometer or mesoscale carriers.¹⁵ Then, they can be manipulated by an external magnetic field, which can permeate the human tissue. The combination of these two factors opens the way for many applications involving, in particular, the transport and/or the accumulation²¹ of the MNPs or the biological magnetic tag.²² The main limitation to these applications, involving low intensity static magnetic fields, is represented by the decrease of the magnetic field strength with the distance to the target (the effective depth in the human body is about 10 cm).²³ Moreover, energy transfer from a time-varying magnetic field to MNPs can occur under certain frequency regime and field intensity. It enables the conversion of energy accumulated by the NPs into heat dissipation, which made them suitable for local magnetic hyperthermia treatment (MHT).²⁴ These and others interesting applications

are made possible in nanomedicine thanks to the particular properties of MNPs. For example: 1) targeted drug delivery; 2) biological separation; 3) biosensing; 4) magnetic resonance imaging (MRI); 5) in gene transcription; 6) neural stimulation; 7) magnetic particles imaging (MPI).^{18,19,25–29} This work was focused on the application of MNPs in MHT, MPI and MRI. The design and synthesis of MNPs should be planned considering some benchmarks important for their application. For the MHT, the MNPs should have a specific absorption rate (SAR) as high as possible, for the lowest dosage allowed, while applying field and frequency parameters in the range deemed safe for human body. In particular the product between these two parameters should be kept below $5 \cdot 10^9 \text{ Am}^{-1}\text{s}^{-1}$ to avoid potential side effects.^{30,31} The SAR value express the heating efficiency of the magnetic nanoparticles being defined as the power absorbed per mass of the heat mediator. The MNPs can be used for MPI an emerging imaging technique.³² MPI has the ability to directly detect MNPs, with no background signal originating from surrounding tissues, resulting in superb contrast.^{29,33,34} The heat generation mechanism in magnetic hyperthermia relies on the same Brownian and Néel relaxation principles for magnetization reversal, which also dictate the signal generation in MPI. Thus, NPs with good magnetic properties for MHT results ideal for the application in MPI. For this reason, recent studies are looking at the interesting possibility to merge the MHT with the MPI, in the so called hMPI, in which imaging and treatment are done with the same device.^{35–37} Then, the MNPs can be exploited as contrast agents for MRI diagnosis, thanks to their ability to enhance proton relaxation of specific tissues. Their properties, inducing magnetic field-inhomogeneities can reduce the longitudinal (T1) and transverse (T2) relaxation times of the surrounding protons, responsible for the MRI image formation.³⁸ Most of the MNPs are T2 agents thanks to their difference in susceptibility with the surrounding media, giving a negative contrast to the MRI images.³⁹ In all these applications, MNPs should be close to the superparamagnetic state, at body temperature, with low magnetostatic interactions, to avoid unwanted behaviors like agglomeration.^{40,41} Lastly, they should be biocompatible with negligible cytotoxic effects.^{42,43} The magnetic properties of the NPs can be optimized by choosing a synthesis method that enable to tune with high control the magnetic relevant parameters that regulate their heating ability and relaxivity. This list of parameters includes: the saturation magnetization (M_s), the remnant magnetization (M_r), the susceptibility (χ), the coercivity (H_c) and the surface anisotropy (K_s).^{44–48} Currently, several methods including coprecipitation,⁴⁹ thermal decomposition,^{48,50} micelle synthesis,⁵¹ hydrothermal synthesis⁵² are exploited to synthesize MNPs with much focus on the synthesis of iron oxide nanoparticles (IONPs). Several synthesis of IONPs prepared by different routes have been reported and

investigated as indeed these nanoparticles are the most promising materials for clinical applications, given their biocompatibility, body tolerance and the proven *in vivo* biodegradability and transformation.^{53–56} Unfortunately, the roughly spherical shaped iron oxide NPs obtained by co-precipitation method, that are currently approved by Food and Drug Administration (FDA) for medical applications,⁵⁷ are characterized by low values of M_s (due to large surface spin disorder),⁵⁸ low control over the size and size distribution which reduce their performance for both MHT and MRI applications. An effective approach to maximize the SAR of IONPs is to tune and control their shape anisotropy for obtaining cubic NPs by thermal decomposition synthesis.⁵⁹ The increased shape anisotropy gave to the NPs important quality as lower surface spin disorder, higher M_s and higher crystallinity.^{60,53,54} Monodisperse iron oxide nanocubes (NCs) have M_s values that are closer to that of bulk magnetite (90 emu/g).⁴⁰ Additionally, compositional tuning has been reported as an alternative and effective strategy to enhance the magnetic properties of MNPs, obtained by the partial or complete replacement of the Fe^{2+} ions in magnetite (Fe_3O_4) NPs with other divalent metal ions like Co^{2+} , Mn^{2+} and Zn^{2+} .^{48,58,63–68} Moreover, the manipulation of MNPs and their aggregation into controlled clusters could play a significant role on the heating performance of NPs. Controlled aggregation in a centrosymmetric 3D configuration (bead-like assembly) was reported to lower SAR values but is useful for MRI and magnetic separation of DNA, molecules and proteins moieties.^{69–72} Currently, the *state of the art* in terms of hyperthermia performances for clustered structures is held by bacterial magnetosome chains, that are about 50 nm cubic-shape IONPs individually coated with a lipid shell, naturally aligned in chain-like morphologies on protein filaments. Since there are evidences that the current understanding of the physical parameters controlling magnetic heating at the nanoscale still needs to be improved, this work was focused on the study of physical parameters that affect NPs heating efficacy, in particular on the viscosity (η) that is the less present in literature.^{42,73–75} The effect of media viscosity change is far more pronounced in anisotropic systems, like cobalt ferrite than in iron oxide NPs.^{41,75} This effect is ascribed to the magnetic relaxation processes (i.e. Néel or Brownian mechanisms). Whereas Néel relaxation is related to the reorientation of the particle magnetic moment, Brownian relaxation is related to the particle rotation for reorienting its magnetic moment. The relaxation processes are affected by different parameters such as the NPs size, anisotropy, magnetic dipolar interaction and magnetic field intensity.^{76–79}

2. Nanoparticles for neurodegenerative diseases and the importance to overcome the Blood Brain Barrier

The nanomaterials used for the neurodegenerative diseases treatment are the ones commonly used in drug delivery (*e.g.* quantum dots, liposomes, solid lipid NPs, gold NPs, IONPs) with particular attention given to size, surface charge and surface chemistry.⁸⁰ Most of the neurodegenerative diseases are defined pathologically by abnormal accumulation into the brain of specific protein species (*e.g.* β amyloid plaques in Alzheimer's disease (AD)).⁸¹ Nowadays, most of the study for the treatment of these pathologies are based on the delivery of compound to reduce or eliminate the diseases impairment. *Mourtas et al.* developed nanoliposomes carrying a curcumin derivate that bind and inhibits the β amyloid aggregation.⁸² *Liu et al* produced polystyrene NP functionalized with an iron chelator (2-methyl-N-(2'- aminoethyl)-3-hydroxyl-4-pyridinone) showing their ability to protect neurons from toxicity related to the peptide aggregation.⁸³ Moreover, *Picone et al.* showed that solid lipid NPs loaded with Ferulic Acid (FA), decrease reactive oxygen species (ROS) generation, restore mitochondrial membrane potential and reduce cytochrome *c* release and intrinsic pathway apoptosis activation.⁸⁵ Further, FA modulate the expression of Peroxiredoxin, an anti-oxidative protein, and attenuate phosphorylation of extracellular signal-regulated protein kinases 1 and 2 (ERK1/2), which can mediate cell proliferation and apoptosis activated by $A\beta$ oligomers.⁸⁵ FA is a natural compound that arises from the metabolism of phenylalanine and tyrosine in plants.⁸⁴ It is reaching attention thanks to his antioxidant properties.^{85,86} All these promising strategy for neurodegenerative diseases treatment are limited by the presence of the Blood Brain Barrier (BBB). The BBB prevents drugs, NPs and imaging agents penetration, limiting their application due to poor access to the Central Nervous System (CNS).¹⁵ Thus, research efforts are focused on developing effective strategies to overcome this barrier and deliver drugs to the CNS.⁸⁷ The BBB is a selective barrier formed by tight junctions (TJ) between cerebral capillary endothelial cells, and represents a critical regulator of the brain homeostasis by exclusion of harmful xenobiotics.⁸⁸ The endothelial layer is so tight that precludes the passage through intercellular junctions (para-cellular passage), limiting the possibility of exchanges between the brain and the blood only through passages across the cellular body (trans-cellular passage).⁸⁹ However, the BBB is not only a mechanical fence but also a dynamic biological entity, in which active metabolism and carrier-mediated transports occur (Figure 1).⁹⁰

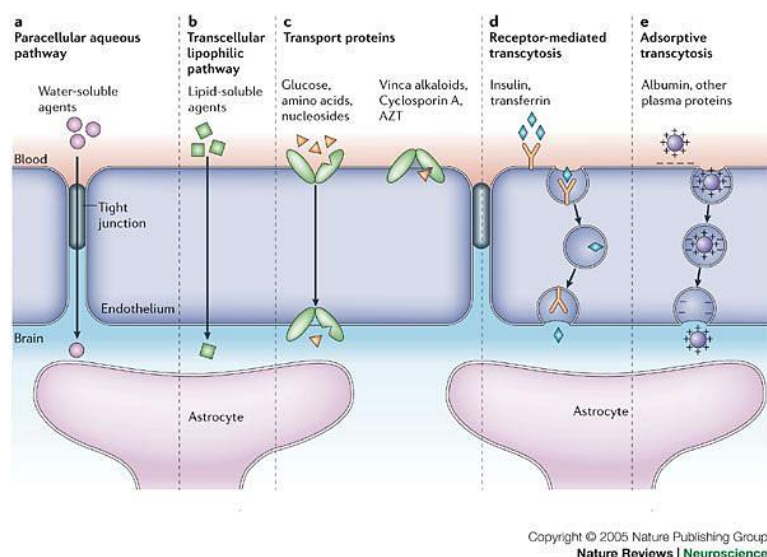


Figure 1 A schematic diagram of the endothelial cells that form the blood–brain barrier (BBB). The main routes for molecular traffic across the BBB are shown. **a**) Normally, the tight junctions severely restrict penetration of water-soluble compounds, including polar drugs. **b**) However, the large surface area of the lipid membranes of the endothelium offers an effective diffusive route for lipid-soluble agents. **c**) The endothelium contains transport proteins (carriers) for glucose, amino acids, purine bases, nucleosides, choline and other substances. Some transporters are energy-dependent (for example, P-glycoprotein) and act as efflux transporters. AZT, azidothymidine. **d**) Certain proteins, such as insulin and transferrin, are taken up by specific receptor-mediated endocytosis and transcytosis. **e**) Native plasma proteins such as albumin are poorly transported, but cationization can increase their uptake by adsorptive-mediated endocytosis and transcytosis. Reproduced, with permission, from reference 57.

Different approaches have been tested to allow pharmaceuticals to overcome the barrier. These explorative strategies have been ranging from invasive techniques, *e.g.*, through osmotic opening of the BBB⁹¹, to chemical modifications of drugs.⁹² These taking advantage of carrier-mediated transports, or exploiting the so-called “Trojan horse” technology, it use the receptor mediated passage system attaching drugs that are not able to cross the BBB alone to molecules which can easily go through.⁹³ Recently, superparamagnetic NPs were exploited as local heat sources to trigger the opening of the TJ thanks to their ability to convert electromagnetic energy into thermal energy.⁹⁴ Moreover, the same heat may be exploited to target and dissolve the fibrils plaques, common in disorders like Alzheimer or Parkinson, or for tumor ablation.^{95–97} Some recent studies revealed encouraging results in this direction.^{98,99} The heating property of magnetic NPs was used by *Tabatabaei et al.* to increase the local temperature to 38–39 °C and consequently the flux of NPs trough the BBB.^{98,100} In this temperature range, it is possible to observe a reversible disruption of the barrier on the surface of the brain. Particularly, the authors showed that large dye molecules are able to cross the BBB after application of MHT and that the barrier is capable to fully recover after treatment. This provides the possibility to access the brain tissue with higher spatial precision, advanced control and lower immune reaction. Nevertheless, in this *in-vivo* study commercial available MNPs were used with low

magnetic properties. For this reason, to have a local heat increase they were forced to administer a huge amount of MNPs (60 μ L at 12g/L). Another promising strategy to overcome the BBB, is the NPs functionalization with the Trans-activating transcriptional activator (TAT) peptide (derived from HIV virus). Such functionalization could be exploited to merge the molecular targeting approach (TAT-based) with the physical one (local heat by magnetic NPs). This subject will be discussed in detail in chapter 2.

References

1. Kim, B. Y. S., Rutka, J. T. & Chan, W. C. W. Nanomedicine. *N. Engl. J. Med.* 1–22 (2014). doi:10.1056/NEJMra1313875
2. Saha, K., Agasti, S. S., Kim, C., Li, X. & Rotello, V. M. Gold Nanoparticles in Chemical and Biological Sensing. *Chem. Rev.* **112**, 2739–2779 (2012).
3. Slowing, I. I., Vivero-Escoto, J. L., Wu, C.-W. & Lin, V. S.-Y. Mesoporous silica nanoparticles as controlled release drug delivery and gene transfection carriers. *Adv. Drug Deliv. Rev.* **60**, 1278–1288 (2008).
4. Kim, D. *et al.* Synthesis of Uniform Ferrimagnetic Magnetite Nanocubes. 454–455 (2009).
5. Chernousova, S. & Epple, M. Silver as Antibacterial Agent: Ion, Nanoparticle, and Metal. *Angew. Chemie Int. Ed.* **52**, 1636–1653 (2013).
6. Katz, E., Willner, I. & Wang, J. Electroanalytical and Bioelectroanalytical Systems Based on Metal and Semiconductor Nanoparticles. *Electroanalysis* **16**, 19–44 (2004).
7. Ordóñez-Gutiérrez, L. *et al.* Repeated intraperitoneal injections of liposomes containing phosphatidic acid and cardiolipin reduce amyloid- β levels in APP/PS1 transgenic mice. *Nanomedicine Nanotechnology, Biol. Med.* **11**, 421–430 (2015).
8. Soppimath, K. S., Aminabhavi, T. M., Kulkarni, A. R. & Rudzinski, W. E. Biodegradable polymeric nanoparticles as drug delivery devices. *J. Control. Release* **70**, 1–20 (2001).
9. and, S. M. G. & Fréchet*, J. M. J. Convergent Dendrons and Dendrimers: from Synthesis to Applications. (2001). doi:10.1021/CR990116H
10. Q A Pankhurst, J Connolly, Skj. and J. D. Applications of magnetic nanoparticles in biomedicine. *J. Phys. D. Appl. Phys.* **36**, 167–181 (2003).
11. Mazumder, S., Dey, R., Mitra, M. K., Mukherjee, S. & Das, G. C. Review: Biofunctionalized Quantum Dots in Biology and Medicine. *J. Nanomater.* **2009**, 1–17 (2009).
12. Ulbrich, K. *et al.* Targeted Drug Delivery with Polymers and Magnetic Nanoparticles: Covalent and Noncovalent Approaches, Release Control, and Clinical Studies. *Chem. Rev.* **116**, 5338–5431 (2016).
13. Roney, C. *et al.* Targeted nanoparticles for drug delivery through the blood-brain barrier for Alzheimer’s disease. *J. Control. Release* **108**, 193–214 (2005).
14. Parak, W. J., Pellegrino, T. & Plank, C. Labelling of cells with quantum dots. *Nanotechnology* **16**, R9–R25 (2005).
15. Doane, T. L. & Burda, C. The unique role of nanoparticles in nanomedicine: Imaging, drug delivery and therapy. *Chem. Soc. Rev.* **41**, 2885–2911 (2012).
16. Lewin, M. *et al.* Tat peptide-derivatized magnetic nanoparticles allow in vivo tracking and recovery of progenitor cells. *Nat. Biotechnol.* **18**, 410–414 (2000).
17. Skomski R. Nanomagnetism. *J. Phys.: Condens. Matter* **15** R841 (2003).
18. Lin, X. M. & Samia, A. C. S. Synthesis, assembly and physical properties of magnetic nanoparticles. *J. Magn. Magn. Mater.* **305**, 100–109 (2006).

19. Lu, A. H., Salabas, E. L. & Schüth, F. Magnetic nanoparticles: Synthesis, protection, functionalization, and application. *Angew. Chemie - Int. Ed.* **46**, 1222–1244 (2007).
20. Wu, W., He, Q. & Jiang, C. Magnetic iron oxide nanoparticles: Synthesis and surface functionalization strategies. *Nanoscale Res. Lett.* **3**, 397–415 (2008).
21. Giri, S., Trewyn, B. G., Stellmaker, M. P. & Lin, V. S.-Y. Stimuli-Responsive Controlled-Release Delivery System Based on Mesoporous Silica Nanorods Capped with Magnetic Nanoparticles. *Angew. Chemie Int. Ed.* **44**, 5038–5044 (2005).
22. Adams, J. D., Kim, U. & Soh, H. T. Multitarget magnetic activated cell sorter. *Proc. Natl. Acad. Sci. U. S. A.* **105**, 18165–70 (2008).
23. Arruebo, M., Fernández-Pacheco, R., Ibarra, M. R. & Santamaría, J. Magnetic nanoparticles for drug delivery. *Nano Today* **2**, 22–32 (2007).
24. Silva, A. C. *et al.* Application of hyperthermia induced by superparamagnetic iron oxide nanoparticles in glioma treatment. *Int. J. Nanomedicine* **6**, 591–603 (2011).
25. Ito, A., Shinkai, M., Honda, H. & Kobayashi, T. Medical application of functionalized magnetic nanoparticles. *J. Biosci. Bioeng.* **100**, 1–11 (2005).
26. Jinhao, G. A. O., Hongwei, G. U. & Bing, X. U. Multifunctional magnetic nanoparticles: design, synthesis, and biomedical applications. *Acc. Chem. Res.* **42**, 1097–1107 (2009).
27. Hergt, R., Dutz, S., Müller, R. & Zeisberger, M. Magnetic particle hyperthermia: Nanoparticle magnetism and materials development for cancer therapy. *J. Phys. Condens. Matter* **18**, (2006).
28. Laurent, S. *et al.* Magnetic Iron Oxide Nanoparticles: Synthesis, Stabilization, Vectorization, Physicochemical Characterizations, and Biological Applications (vol 108, pg 2064, 2008). *Chem. Rev.* **108**, 2064–2110 (2008).
29. Bauer, L. M., Situ, S. F., Griswold, M. A. & Samia, A. C. S. High-performance iron oxide nanoparticles for magnetic particle imaging-guided hyperthermia (hMPI). *Nanoscale* **8**, 12162–12169 (2016).
30. Hergt, R., Dutz, S. & Röder, M. Effects of size distribution on hysteresis losses of magnetic nanoparticles for hyperthermia. *J. Phys. Condens. Matter* **20**, (2008).
31. He, S. *et al.* Maximizing Specific Loss Power for Magnetic Hyperthermia by Hard–Soft Mixed Ferrites. *Small* **14**, 1–9 (2018).
32. Gleich, B. & Weizenecker, J. Tomographic imaging using the nonlinear response of magnetic particles. *Nature* **435**, 1214–1217 (2005).
33. Goodwill, P. W. *et al.* X-Space MPI: Magnetic nanoparticles for safe medical imaging. *Adv. Mater.* **24**, 3870–3877 (2012).
34. Saritas, E. U. *et al.* Magnetic particle imaging (MPI) for NMR and MRI researchers. *J. Magn. Reson.* **229**, 116–126 (2013).
35. Aoki, M., Banura, N., Nishimoto, K., Mimura, A. & Hamakawa, K. Usefulness of magnetic particle imaging for monitoring the therapeutic effect of magnetic hyperthermia. **53**, 252409 (2015).
36. Murase, K., Takata, H., Takeuchi, Y. & Saito, S. Control of the temperature rise in magnetic hyperthermia with use of an external static magnetic field. *Phys. Medica* **29**, 624–630 (2013).

37. Kuboyabu, T. *et al.* Magnetic Particle Imaging for Magnetic Hyperthermia Treatment: Visualization and Quantification of the Intratumoral Distribution and Temporal Change of Magnetic Nanoparticles & *Open J. Med. Imaging* **06**, 1–15 (2016).
38. Na, H. Bin, Song, I. C. & Hyeon, T. Inorganic nanoparticles for MRI contrast agents. *Adv. Mater.* **21**, 2133–2148 (2009).
39. Ni, D., Bu, W., Ehlerding, E. B., Cai, W. & Shi, J. Engineering of inorganic nanoparticles as magnetic resonance imaging contrast agents. *Chem. Soc. Rev.* **46**, 7438–7468 (2017).
40. Dennis, C. L. & Ivkov, R. Physics of heat generation using magnetic nanoparticles for hyperthermia. *Int. J. Hyperth.* **29**, 715–729 (2013).
41. Rosensweig, R. E. Heating magnetic fluid with alternating magnetic field. *J. Magn. Magn. Mater.* **252**, 370–374 (2002).
42. Fortin, J. P. *et al.* Size-sorted anionic iron oxide nanomagnets as colloidal mediators for magnetic hyperthermia. *J. Am. Chem. Soc.* **129**, 2628–2635 (2007).
43. Di Corato, R. *et al.* Magnetic hyperthermia efficiency in the cellular environment for different nanoparticle designs. *Biomaterials* **35**, 6400–6411 (2014).
44. Mehdaoui, B. *et al.* Optimal size of nanoparticles for magnetic hyperthermia: A combined theoretical and experimental study. *Adv. Funct. Mater.* **21**, 4573–4581 (2011).
45. Walter, A. *et al.* Mastering the shape and composition of dendronized iron oxide nanoparticles to tailor magnetic resonance imaging and hyperthermia. *Chem. Mater.* **26**, 5252–5264 (2014).
46. Smolensky, E. D. *et al.* Scaling laws at the nanosize: The effect of particle size and shape on the magnetism and relaxivity of iron oxide nanoparticle contrast agents. *J. Mater. Chem. B* **1**, 2818–2828 (2013).
47. Zhao, Z. *et al.* Octapod iron oxide nanoparticles as high-performance T2 contrast agents for magnetic resonance imaging. *Nat. Commun.* **4**, 1–7 (2013).
48. Sathya, A. *et al.* Co_xFe_{3-x}O₄ Nanocubes for Theranostic Applications: Effect of Cobalt Content and Particle Size. *Chem. Mater.* [acs.chemmater.5b04780](https://doi.org/10.1021/acs.chemmater.5b04780) (2016). doi:10.1021/acs.chemmater.5b04780
49. Gupta, A. K. & Gupta, M. Synthesis and surface engineering of iron oxide nanoparticles for biomedical applications. *Biomaterials* **26**, 3995–4021 (2005).
50. Guardia, P. *et al.* One pot synthesis of monodisperse water soluble iron oxide nanocrystals with high values of the specific absorption rate. *J. Mater. Chem. B* **2**, 4426 (2014).
51. Hyeon, T. Chemical synthesis of magnetic nanoparticles. *Chem. Commun.* **0**, 927–934 (2003).
52. T. J. Daou, *,† *et al.* Hydrothermal Synthesis of Monodisperse Magnetite Nanoparticles. (2006). doi:10.1021/CM060805R
53. Zhang, H., Huang, H., He, S., Zeng, H. & Pralle, A. Monodisperse magnetofluorescent nanoplatforms for local heating and temperature sensing. *Nanoscale* **6**, 13463–13469 (2014).
54. Gazeau, F., Lévy, M. & Wilhelm, C. Optimizing magnetic nanoparticle design for nanothermotherapy. *Nanomedicine* **3**, 831–844 (2008).

55. Lartigue, L. *et al.* Cooperative organization in iron oxide multi-core nanoparticles potentiates their efficiency as heating mediators and MRI contrast agents. *ACS Nano* **6**, 10935–10949 (2012).
56. Kolosnjaj-Tabi, J. *et al.* Heat-generating iron oxide nanocubes: Subtle ‘destructorators’ of the tumoral microenvironment. *ACS Nano* **8**, 4268–4283 (2014).
57. Anselmo, A. C. & Mitragotri, S. A Review of Clinical Translation of Inorganic Nanoparticles. *AAPS J.* **17**, 1041–1054 (2015).
58. Song, Q. & Zhang, Z. J. Controlled synthesis and magnetic properties of bimagnetic spinel ferrite CoFe₂O₄ and MnFe₂O₄ nanocrystals with core-shell architecture. *J. Am. Chem. Soc.* **134**, 10182–90 (2012).
59. Guardia, P. *et al.* Water-soluble iron oxide nanocubes with high values of specific absorption rate for cancer cell hyperthermia treatment. *ACS Nano* **6**, 3080–3091 (2012).
60. and, Q. S. & Zhang*, Z. J. Shape Control and Associated Magnetic Properties of Spinel Cobalt Ferrite Nanocrystals. (2004). doi:10.1021/JA049931R
61. Yang, H., Hasegawa, D., Takahashi, M. & Ogawa, T. Facile synthesis, phase transfer, and magnetic properties of monodisperse magnetite nanocubes. *IEEE Trans. Magn.* **44**, 3895–3898 (2008).
62. Salas, G., Veintemillas-Verdaguer, S. & Morales, M. D. P. Relationship between physico-chemical properties of magnetic fluids and their heating capacity. *Int. J. Hyperth.* **29**, 768–776 (2013).
63. Behdadfar, B., Kermanpur, A., Sadeghi-Aliabadi, H., Morales, M. D. P. & Mozaffari, M. Synthesis of aqueous ferrofluids of Zn xFe 3-xO 4 nanoparticles by citric acid assisted hydrothermal-reduction route for magnetic hyperthermia applications. *J. Magn. Magn. Mater.* **324**, 2211–2217 (2012).
64. Zargar, T. & Kermanpur, A. Effects of hydrothermal process parameters on the physical, magnetic and thermal properties of Zn_{0.3}Fe_{2.7}O₄ nanoparticles for magnetic hyperthermia applications. *Ceram. Int.* **43**, 5794–5804 (2017).
65. Sansom, C. L. *et al.* Synthesis and characterization of Mn_{0.5}Zn_{0.5}Fe₂O₄ and Fe₃O₄ nanoparticle ferrofluids for thermo-electric conversion. *J. Magn. Magn. Mater.* **335**, 159–162 (2013).
66. Phong, P. T., Nam, P. H., Manh, D. H. & Lee, I. J. Mn_{0.5}Zn_{0.5}Fe₂O₄ nanoparticles with high intrinsic loss power for hyperthermia therapy. *J. Magn. Magn. Mater.* **433**, 76–83 (2017).
67. Xu, Y. *et al.* Preparation and magnetic properties of ZnFe₂O₄ nanotubes. *J. Nanomater.* **2011**, 1–6 (2011).
68. Sun, S. *et al.* Monodisperse MFe₂O₄ (M = Fe, Co, Mn) nanoparticles. *J. Am. Chem. Soc.* **126**, 273–279 (2004).
69. Niculaes, D. *et al.* Asymmetric Assembling of Iron Oxide Nanocubes for Improving Magnetic Hyperthermia Performance. *ACS Nano* **11**, 12121–12133 (2017).
70. Strömberg, M. *et al.* Sensitive molecular diagnostics using volume-amplified magnetic nanobeads. *Nano Lett.* **8**, 816–821 (2008).
71. Bigall, N. C. *et al.* Colloidal ordered assemblies in a polymer shell - A novel type of magnetic nanobeads for theranostic applications. *Chem. Mater.* **25**, 1055–1062 (2013).
72. Materia, M. E. *et al.* Mesoscale Assemblies of Iron Oxide Nanocubes as Heat Mediators and Image Contrast Agents. *Langmuir* **31**, 808–816 (2015).
73. Jordan, A. *et al.* Inductive heating of ferrimagnetic particles and magnetic fluids: Physical evaluation of their potential

- for hyperthermia. *Int. J. Hyperth.* **25**, 499–511 (2009).
74. Cabrera, D., Camarero, J., Ortega, D. & Teran, F. J. Influence of the aggregation, concentration, and viscosity on the nanomagnetism of iron oxide nanoparticle colloids for magnetic hyperthermia. *J. Nanoparticle Res.* **17**, (2015).
 75. Cabrera, D. *et al.* Unraveling viscosity effects on the hysteresis losses of magnetic nanocubes. *Nanoscale* **9**, 5094–5101 (2017).
 76. Salas, G. *et al.* Modulation of magnetic heating via dipolar magnetic interactions in monodisperse and crystalline iron oxide nanoparticles. *J. Phys. Chem. C* **118**, 19985–19994 (2014).
 77. Dieckhoff, J., Eberbeck, D., Schilling, M. & Ludwig, F. Magnetic-field dependence of Brownian and Néel relaxation times. *J. Appl. Phys.* **119**, (2016).
 78. Yoshida, T. & Enpuku, K. Simulation and quantitative clarification of AC susceptibility of magnetic fluid in nonlinear Brownian relaxation region. *Jpn. J. Appl. Phys.* **48**, (2009).
 79. Mamiya, H. & Jeyadevan, B. Hyperthermic effects of dissipative structures of magnetic nanoparticles in large alternating magnetic fields. *Sci. Rep.* **1**, 1–7 (2011).
 80. Re, F., Gregori, M. & Masserini, M. Nanotechnology for neurodegenerative disorders. *Maturitas* **73**, 45–51 (2012).
 81. Schain, M. & Kreisl, W. C. Neuroinflammation in Neurodegenerative Disorders—a Review. *Curr. Neurol. Neurosci. Rep.* **17**, 25 (2017).
 82. Mourtas, S. *et al.* Curcumin-decorated nanoliposomes with very high affinity for amyloid- β 1-42 peptide. *Biomaterials* **32**, 1635–1645 (2011).
 83. Liu, G., Men, P., Kudo, W., Perry, G. & Smith, M. A. Nanoparticle–chelator conjugates as inhibitors of amyloid- β aggregation and neurotoxicity: A novel therapeutic approach for Alzheimer disease. *Neurosci. Lett.* **455**, 187–190 (2009).
 84. Srinivasan, M., Sudheer, A. R. & Menon, V. P. Ferulic Acid: Therapeutic Potential Through Its Antioxidant Property. *J. Clin. Biochem. Nutr.* **40**, 92–100 (2007).
 85. Picone, P. *et al.* Ferulic acid inhibits oxidative stress and cell death induced by Ab oligomers: Improved delivery by solid lipid nanoparticles. *Free Radic. Res.* **43**, 1133–1145 (2009).
 86. Srinivasan, M., Sudheer, A. R. & Menon, V. P. Recent Advances in Indian Herbal Drug Research Guest Editor: Thomas Paul Asir Devasagayam Ferulic Acid: Therapeutic Potential Through Its Antioxidant Property. *J. Clin. Biochem. Nutr.* **40**, 92–100 (2007).
 87. Modi, G., Pillay, V. & Choonara, Y. E. Advances in the treatment of neurodegenerative disorders employing nanotechnology. *Ann. N. Y. Acad. Sci.* **1184**, 154–172 (2010).
 88. Abbott, N. J., Patabendige, A. A. K., Dolman, D. E. M., Yusof, S. R. & Begley, D. J. Structure and function of the blood–brain barrier. *Neurobiol. Dis.* **37**, 13–25 (2010).
 89. Abbott, N. J., Rönnbäck, L. & Hansson, E. Astrocyte–endothelial interactions at the blood–brain barrier. *Nat. Rev. Neurosci.* **7**, 41–53 (2006).
 90. Masserini, M. Nanoparticles for Brain Drug Delivery. *ISRN Biochem.* **2013**, 1–8 (2013).
 91. Bellavance, M.-A., Blanchette, M. & Fortin, D. Recent Advances in Blood–Brain Barrier Disruption as a CNS

- Delivery Strategy. *AAPS J.* **10**, 166–177 (2008).
92. Brambilla, D. *et al.* Nanotechnologies for Alzheimer’s disease: diagnosis, therapy, and safety issues. *Nanomedicine Nanotechnology, Biol. Med.* **7**, 521–540 (2011).
 93. Pardridge, W. M. Drug Transport across the Blood–Brain Barrier. *J. Cereb. Blood Flow Metab.* **32**, 1959–1972 (2012).
 94. Gupta, A. K. & Gupta, M. Synthesis and surface engineering of iron oxide nanoparticles for biomedical applications. *Biomaterials* **26**, 3995–4021 (2005).
 95. Carradori, D., Gaudin, A., Brambilla, D. & Andrieux, K. *Application of Nanomedicine to the CNS Diseases. International Review of Neurobiology* **130**, (Elsevier Inc., 2016).
 96. Portney, N. G. & Ozkan, M. Nano-oncology: drug delivery, imaging, and sensing. *Anal. Bioanal. Chem.* **384**, 620–630 (2006).
 97. Jain, K. Advances in the field of nanooncology. **8**, 1741–7015 (2010).
 98. Tabatabaei, S. N., Girouard, H., Carret, A.-S. & Martel, S. Remote control of the permeability of the blood–brain barrier by magnetic heating of nanoparticles: A proof of concept for brain drug delivery. *J. Control. Release* **206**, 49–57 (2015).
 99. Dan, M., Bae, Y., Pittman, T. a. & Yokel, R. a. Alternating Magnetic Field-Induced Hyperthermia Increases Iron Oxide Nanoparticle Cell Association/Uptake and Flux in Blood-Brain Barrier Models. *Pharm. Res.* **32**, 1615–1625 (2015).
 100. Kiyatkin, E. A. & Sharma, H. S. Permeability of the blood-brain barrier depends on brain temperature. *Neuroscience* **161**, 926–939 (2009).
 101. Quarta, A., Curcio, A., Kakwere, H. & Pellegrino, T. Polymer coated inorganic nanoparticles: tailoring the nanocrystal surface for designing nanoprobe with biological implications. *Nanoscale* **4**, 3319 (2012).

Chapter 1. Synthesis and characterization of divalent metal ions substituted ferrite nanocubes

1.1 Introduction

Basis of nanomagnetism

Nanomagnetism (*i.e.*, the magnetism observed at the nanoscale) is a key concept to be addressed when designing magnetic nanoparticles (MNPs). The classical types of magnetic behavior; diamagnetic, paramagnetic, ferromagnetic, ferrimagnetic and antiferromagnetic, appears at the nanoscale based on the collective response of the magnetic dipoles inside a NPs in presence of an applied magnetic field (Figure 1).¹ For diamagnetic materials, a zero magnetization is observed in the absence of a magnetic field, that is, there are no magnetic dipoles. But, upon application of a magnetic field, the variation of the magnetic flux induces an spontaneous magnetization opposite to the magnetic field obeying Lenz law. As a result, magnetic dipoles oriented opposite to that of the applied magnetic field are formed inside the material. Paramagnetic materials already present magnetic dipoles, which are randomly distributed in absence of a magnetic field with zero magnetization. However, upon application of an external magnetic field, dipoles aligned in the direction of the magnetic field and a net magnetization is observed. Ferromagnetic materials show a similar behavior having a net magnetic moment in the absence of an external magnetic field. This is due to exchange or super exchange interactions, which keep magnetic dipoles aligned even if the magnetic field is zero. Noteworthy, this interaction may result in an antiparallel arrangement of the dipoles inside the magnetic material at zero field, the so-called antiferromagnetic and ferrimagnetic materials. The above described magnetic behaviors are typically related to multi domain systems, also present at the nanoscale. Yet, when size is decreased under a certain limit the energy balance of the systems result in the formation of single domain particles and superparamagnetism takes place. In the section below a more detail description of this magnetic behavior observable only at the nanoscale is described.²

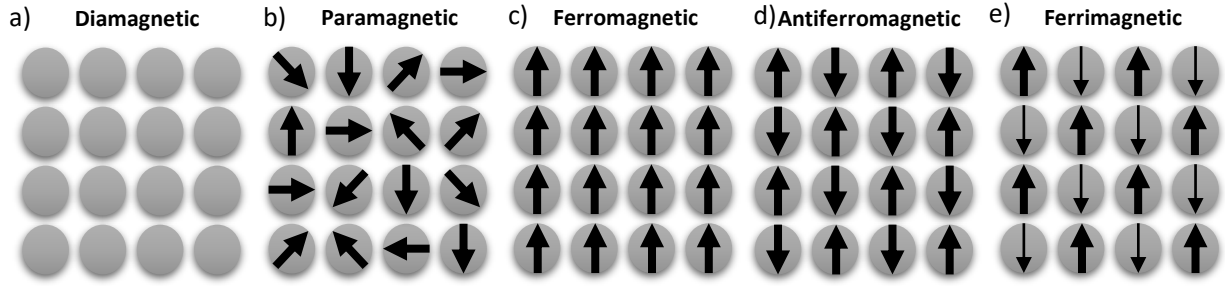


Figure 1 Schematic illustrating the arrangements of magnetic dipoles for five different types of materials. **a)** Diamagnetic materials does not have magnetic dipoles in absence of an external magnetic field, upon application of a field, the material produces a magnetic dipole that is oriented opposite to that of the applied field. **b)** Paramagnetic materials, there exist magnetic dipoles, but these are aligned only upon application of an external magnetic field. **c)** Ferromagnetic materials have net magnetic dipole moments in the absence of an external magnetic field. **d)** In antiferromagnetic and **e)** ferrimagnetic materials, the atomic level magnetic dipole moments are similar to those of ferromagnetic materials but adjacent dipole moments exist that are not oriented in parallel and effectively cancel or reduce, respectively, the impact of neighboring magnetic dipoles within the material in the absence of an applied field.

The research in MNPs for nanomedicine applications is typically focused on developing superparamagnetic NPs.^{1,3-5} The desired MNPs for applications in drug delivery, exhibit no magnetic properties at body temperature after removal of the external magnetic field and for that reason, dipole-dipole magnetic interaction are suppressed eliminating the risk of aggregation. This is the “so called” superparamagnetic (SPM) regime. Furthermore, superparamagnetic NPs provide a strong and quick response to an external magnetic field allowing a precise control over the application of their magnetic properties. Noteworthy, the SPM behavior does strongly depend on the temperature, as described below. As such, below a certain temperature a transition between a SPM to a ferromagnetic state take place. Ferromagnetic NPs are characterized by a typical magnetization curve, which exhibits characteristic positions associated with saturation magnetization (M_s , all the magnetic dipoles are aligned to the external magnetic field, the maximum magnetization is reached), remnant magnetization (M_r , induced magnetization remaining after removal of the applied field) and coercivity (H_c , the intensity of an external coercive field needed to force the magnetization to zero). In contrast to the hysteresis generate in case of ferromagnetic NPs, the response of superparamagnetic NPs show no hysteresis but it follows the same sigmoidal curve (Figure 2).

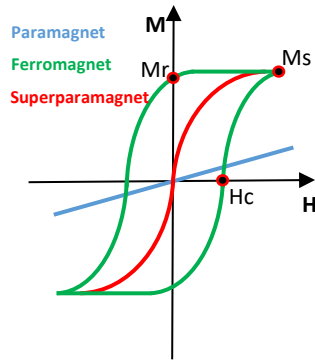


Figure 2 Typical magnetization curve of a paramagnetic, ferro- or ferromagnetic and superparamagnetic materials. From the hysteresis loop of ferromagnet material can be identified the saturation magnetization M_s (the maximum value of M); the remanence magnetization M_r (the residual magnetization at zero field strength); and the coercivity H_c (the external field required to bring magnetization back to zero).

Magnetization is a strong temperature dependent feature being the M_s maximum at 0 K as thermal energy/vibrations (and thus randomization of aligned moments) is reduced. Above the temperature known as the blocking temperature (T_B), both ferromagnetic and ferrimagnetic nanoparticles exhibit a superparamagnetic behavior manifested by rapid random MNP magnetization reversals leading to a zero time-average magnetic moment. The value of T_B , associated with the energy barrier, depends on the characteristic measuring time, which can vary from 100 to 10^{-8} s.⁶ From the relative difference between the measuring time and the relaxation time, arise the magnetic behavior. Thus, if the relaxation time is lower than measuring time, the NPs are considered to be in the SPM regime; if, however, the relaxation time is higher than the measuring time, the NPs are in a “blocked” (ferromagnetic) regime.⁶ If the MNP size is maintained below a critical dimension during the synthesis, they tend to develop as single magnetic domain structures, and at the smallest sizes, they exhibit SPM behavior.^{7,8}

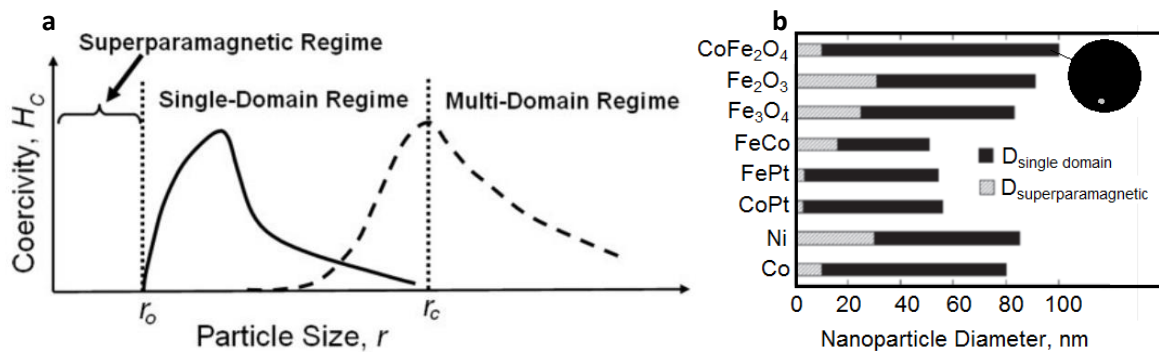


Figure 3 a) Schematic illustrating the dependence of magnetic coercivity on particle size. In the single-domain regime, the coercivity can follow either the solid curve for non-interacting particles or the dashed line for particles that have coupling between them. The coercivity falls to zero for superparamagnetic colloidal particles. Reproduced with permission from reference 51. **b)** On the nanometer length scale magnetic materials, at a given temperature, show distinctly different behavior as a function of size; most noticeably, this is observed in nanoparticles. For diameters $D < D_{sp}$, they exhibit superparamagnetism; for $D > D_{sd}$, they split into multiple domains to minimize their overall energy and in between $D_{sp} < D < D_{sd}$, they are ferromagnetic and single domain. These characteristic sizes depend on their intrinsic properties (saturation magnetization M_s , anisotropy constant k , and exchange stiffness), and can easily be calculated. Critical sizes for the observation of superparamagnetism D_{sp} , and single-domain D_{sd} , behavior in a variety of common ferromagnetic fine particles are shown. Reproduced with permission from reference 52.

The critical size (r_c), which corresponds to a transition from the single- to the multi-domain is associated with the size below which it is energetically favorable for the magnetic grain (or particle) to exist without a domain wall^{9,10}. Thus, that size might be interpreted as the maximum size for a single-domained structure. However, with the broad choice of magnetic materials in use in MNP research, it is challenging to define a discrete transition point for r_c . A domain wall is defined as a transition region between the different magnetic domains of uniform magnetization it develops when a magnetic material forms domains to minimize the magnetostatic energy; the wall energy is the energy required to maintain this wall. When domains are formed, the magnetostatic energy decreases, and the wall energy and the magnetocrystalline anisotropy energy increase. When the NPs size is bigger than the thickness of the domain wall, it is forced to split into domains. Thus, the domain wall thickness (and the critical size, r_c) depends on three parameters: the exchange energy (which is the energy required to keep the spins parallel and is low in case of a thick wall), magnetization and NPs anisotropy (K). In this way, the transition point from SPM to single-domain to multi-domain for MNPs depends upon different parameters. In particular, those are the size and/or shape of the NPs, and the intrinsic material parameters coming from the composition, such as M_s and K . Hence,

it is important to understand the fundamental magnetic properties and their interdependence to be able to optimize the MNPs for particular applications (i.e. MHT, MRI and MPI).

Hyperthermia: using MNPs for heat generation

Among the different definitions of Hyperthermia, it is possible to define it as an abnormally high body temperature. Hyperthermia therapy is a type of treatment in which body tissues are exposed to high temperatures to damage and kill cancer cells, or to make them more sensitive to other therapies such as radio- or chemotherapy.¹¹ Nowadays, the nanomedicine advances allowed the use of engineered MNPs as heating mediators for the application of local MHT.¹² The first use of MNPs for MHT on an animal model date back from 1957.¹³ This pioneer study has paved the way in the last two decades to the first clinical trials of MNP-based hyperthermia led by MagForce Nanotechnology, AG Germany .¹⁴ The heating ability of MNPs under an alternating magnetic field (AMF) can be expressed by the specific absorption rate (SAR), which provides a measurement of the transformation of magnetic energy into thermal energy. The SAR values accounts for the energy rate released to the environment per unit mass of magnetic material (i.e. MNPs):

$$\text{SAR} \left(\frac{\text{W}}{\text{g}} \right) = \frac{C}{m} \cdot \frac{dT}{dt}$$

Where C is the specific heat capacity of water (4185 J/kgK) and m is the concentration (g/L) of magnetic material in solution. This equation is only valid under adiabatic conditions; however, at a first approximation, the slope of the curve (dT/dt) can be measured by taking into account only the first few seconds of the temperature versus time in which a quasi-adiabatic regime is assumed.^{15,16}

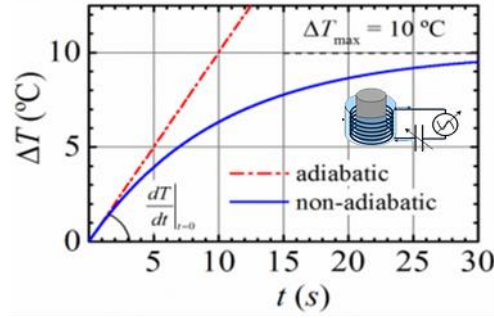


Figure 4 Schematic representation of the heating curve profiles of a MNPs sample placed in AMF, in case of adiabatic condition (red) and non adiabatic condition (blue). The two curves are equal in the first few seconds and then start to diverge. Modified and reproduced with permission from reference 64.

During an MHT experiment, MNPs are exposed to an AMF of amplitude H and frequency f . Thus, the atomic magnetic moments (m) of the MNPs are forced to align with the external field. The degree of alignment depends upon the H magnitude and the NPs properties. Since the external field polarity changes, the direction of m will also change. When the frequency of the changing external field increases, the MNP's magnetic moment may, cease to change “instantaneously”, resulting in a lag in the magnetic response. If the external AMF has sufficient amplitude to force the m to oscillate this opens the hysteresis loops (HLs) as the result of this lag. Hysteresis for MNPs is accompanied by losses, which manifest themselves as heat. The enhanced anisotropy present in these kind of NPs contributes to increase hysteretic losses when they are subjected to AMFs, leading to much higher SAR, or heat.¹⁷ The hysteretic or thermal losses are expressed by the area A of the hysteresis loop:

$$A = \int_{-H}^{+H} \mu_0 M(H) dH$$

Where $M(H)$ is the NP's magnetization. With frequency f as the number of cycles per second, the SAR is given by the product $A \cdot f$. The theoretical and experimental challenge is thus to correlate the characteristics of MNPs and the causes of the lag in magnetic response. The linear response theory, first proposed by Rosensweig¹⁸, it is a good approximation of the MNPs behavior in AMF. This theory is valid under some limitations; it considers the case where thermal fluctuations can reverse the particle magnetic moment with a certain probability. It is only valid at low AMF amplitudes, so that the magnetization responds linearly to the applied field and the energy barrier between two thermodynamically stable directions of the particle

magnetic moment is not substantially modified by the applied field. In this case, the hysteresis loop area is given by:

$$A = \frac{\pi\mu_0 H^2 V M_s^2}{3k_B T} \frac{2\pi f \tau}{[1 + (2\pi f \tau)^2]}$$

In which T is the temperature, k_B is the Boltzmann constant, and τ is the characteristic relaxation time of m . τ is determined by two mechanisms: Néel relaxation with characteristic time τ_N depending exponentially on the volume and anisotropy constant of the material; and Brownian relaxation with characteristic time τ_B depending linearly on the local viscosity and hydrodynamic volume of the MNPs. The effective time constant τ is therefore derive from these equations:

$$\frac{1}{\tau} = \frac{1}{\tau_B} + \frac{1}{\tau_N}$$

$$\tau_N = \frac{\sqrt{\pi}}{2\sqrt{KV/k_B T}} \tau_0 e^{-KV/k_B T}$$

$$\tau_B = \frac{3\eta V_H}{k_B T}$$

Where τ_0 is the inverse of the frequency, K is the magnetic anisotropy constant, V is the NPs volume, k_B is the Boltzmann constant, T is the temperature, η is the viscosity and V_H is the hydrodynamic volume. Given these equations, magnetic relaxation will be dominated by the shortest time.

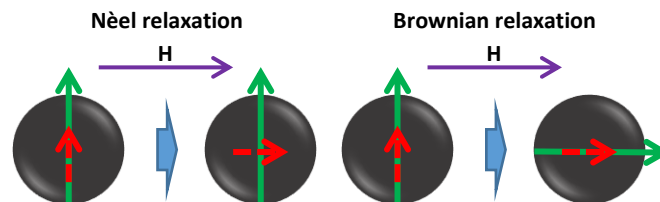


Figure 5 Schematic representation of relaxation processes that influence the heating properties of MNPs Néel relaxation involves internal rotation of the magnetic moment. Instead, Brownian relaxation pertains to the physical rotation of the MNPs. The effective relaxation time is constituted by the collective contribution on both Néel and Brownian relaxation processes.

For example, when τ_N is much shorter than τ_B (*i.e.*, for small enough NPs and anisotropy or for blocked NPs) the Néel fluctuations govern the relaxation and the SAR is maximized in a very narrow size range that depends on both the anisotropy (K) and the field frequency. Being these expressions dependent from NPs size, K , M_s and η it is possible to use them for the optimization of the MNPs characteristics. Interesting, is the square dependence of SAR on the M_s (coming from the expression of initial susceptibility in the linear response model), which will be of paramount importance in optimizing the SAR. The current understanding of the physical parameters controlling magnetic heating at the nanoscale still needs to be improved. Beside all, η is the less studied^{19,20}, but it is crucial for the MNPs application in biological environment. Many recent studies have found a strong reduction in heating efficacy of MNPs when located into cells and tissues.^{21–24} This could be ascribed to the viscosity increase²⁵ and to the MNPs aggregation induced by the cellular biological environment.²⁶ *Cabrera et al.* have recently published an interesting study about the viscosity effect on the heating capacity of IONCs of 14 and 24 nm in cube edge and on cobalt-ferrite nanocubes (CoFeNCs).²⁷ They have showed how not only the MNP size and K favor the Brownian relaxation process, but also low H and large size distribution.

Magnetic resonance imaging (MRI): using MNPs as image contrast agents

MRI is currently one of the routine diagnosis tools in clinic, especially for cancer diagnose.²⁸ It has been the tool for imaging the brain and the central nervous system, for assessing cardiac function, and for detecting tumors. MRI is based on the interaction of nuclear moments of hydrogen protons with static and oscillating magnetic fields (B_0 and B_{rf}). Under a static magnetic field (B_0) and upon application of a transverse radiofrequency (rf) pulse, these protons are perturbed. The subsequent process through which these protons return to their original state is referred to as relaxation. The study of two independent relaxation processes, longitudinal and transverse relaxation, and more specific their T_1 (recovery) and T_2 (decay) relaxation times respectively, is exploited to generate an MRI image. As it is visible in Figure 6 b and c, the T_1 and T_2 relaxation process of protons are shortened when is present a contrast agent. The shortening of the two relaxations gave a brighter image in case of T_1 contrast agent and a darker image under the presence of T_2 contrast agent (Figure 6).

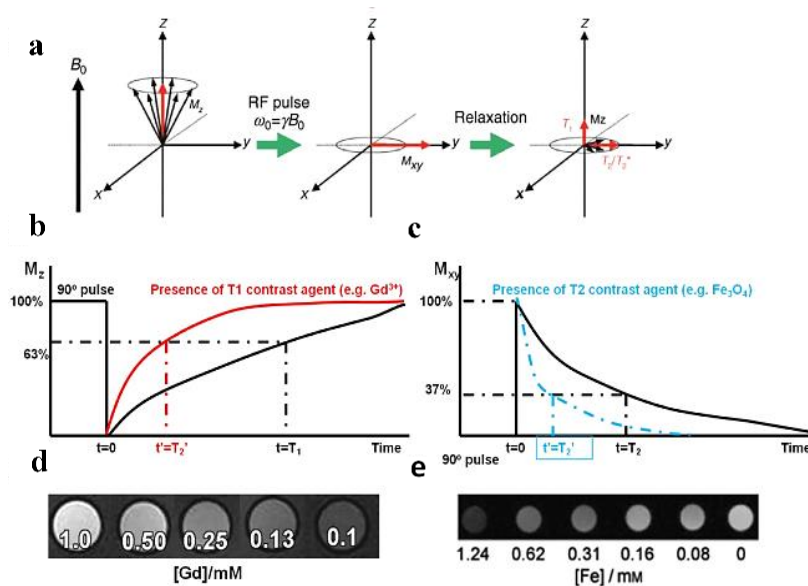


Figure 6 Principle of magnetic resonance imaging. **a)** Spins align parallel or antiparallel to the magnetic field and precess under Larmor frequency (ν_0). After induction of RF pulse, magnetization of spins changes. Excited spins take relaxation process of T_1 and T_2 relaxation. **(b)** and **(c)**) T_1 relaxation of protons is shortened under the presence of T_1 contrast agents (e.g. Gd^{3+}), which will generate a brighter image; **(d)** and **(e)**) T_2 relaxation of protons is shortened under the presence of T_2 contrast agents (e.g. Fe_3O_4 NPs), which will generate a darker image. Reproduced with permission from reference 73.

Local variation in relaxation times of the protons arises from proton density as well as the chemical and physical nature of the tissues within the specimen, give rise to a contrast in the image.^{28–30} MNPs are exploited as contrast agents for MRI diagnosis, thanks to their ability to influence the proton relaxation. They can induce strong magnetic field in-homogeneities, affecting both the longitudinal and transverse relaxation times of surrounding protons. Thus this ends into enhanced contrast localized in the accumulation site (i.e. tumor area).³¹ Anyhow, the shortening of T_1 processes needs a strict interaction between protons and T_1 -agents. Hence, the thickness of the MNPs coating can interfere with these processes.³¹ On the other hand, the effect of MNPs on T_2 shortening is derived by the pronounced susceptibility difference between the NPs and the surrounding media. This results in the formation of microscopic field gradients. The diffusion of protons through these gradients generate the dephasing of the proton magnetic moments, decreasing transverse relaxation times of protons.^{32,33} Nowadays, the most studied T_2 -agents are the superparamagnetic iron oxide NPs, which are used to provide negative contrast enhancement.^{34,35} The efficiency of a contrast agent does also depend on composition, size, shape, and aggregation state of the MNPs.^{34,36–38} The efficacy of the contrast agent can be described by its relaxivity, which is proportional to the measured rate of relaxation over a range of contrast agent concentrations (R_1 ($1/T_1$) and R_2 ($1/T_2$)). Indeed the R_1 and R_2 are obtained

by calculating the slope of the measured relaxation rates. The relaxivity of a sample varies with not only the MNPs properties, but also experimental variables such as field strength, temperature and the medium in which the measurements were done.

Magnetic particle imaging (MPI): using MNPs as image tracer

MPI is an emerging tracer imaging modality, it was first presented by *Gleich and Weizenecker* in 2005 and invented by the same authors few years before when they were at the Philips Research Laboratories in Hamburg.³⁹ Differently from MRI, MPI has the great advantage to detect only MNPs, with no background signal coming from tissue (being diamagnetic), having a near-perfect contrast.⁴⁰ Instead, as MRI, MPI shares the advantage to be penetration depth independent. Moreover, at low frequency of AMF, there is zero depth attenuation, thus making the MPI scan quantitative at any depth.⁴¹ These peculiarity associated with the biocompatibility of iron-based tracers has made this technique a useful alternative to the standard diagnostic imaging system such as MRI, X-Ray and positron emission tomography (PET).⁴⁰ The MPI technique relies on spatially selective saturation of MNPs achieved by a strong magnetic field.^{39,41} A 3D field gradient saturates all the MNPs tracer, leaving at the origin of the gradient a region where the magnetic field is zero, known as field-free region (FFR).⁴² The MNPs inside the FFR are generating the MPI signal, being able to align with the time-varying excitation fields, while those outside of the FFR are blocked by the field gradient.⁴³ The image is formed by shifting the FFR across the imaging field of view (FOV). The FFR passing over the MNPs induces a magnetization reversal, which is detected by the receiver coil.

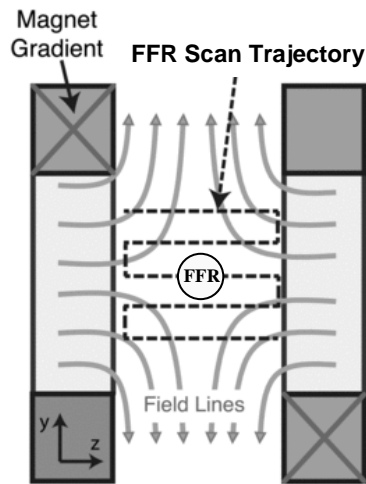


Figure 7 A strong magnetic field gradient forms a sensitive region known as a Field Free Region (FFR) in which the magnetic field is zero. The FFR can be moved in a scan trajectory to cover the imaging field of view (FOV). Modified and reproduced with permission from reference 41.

After the recording of the raw MPI signal by the receiver coil, an MPI image can be reconstructed. There are two principal methods for reconstructing an image in MPI such as harmonic-space MPI and x-space MPI.⁴⁴⁻⁴⁶ In x-space MPI, the image is reconstructed as a convolution of the NPs spatial distribution with the point spread function (PSF), obtained by mapping the instantaneous position of the FFR (following a grid scheme).⁴¹ Moreover, the images resolution is determined by the full-width at half-maximum (FWHM) of the PSF.⁴² This technique produces quantitative images that are linear and shift invariant (LSI), property that is crucial to obtain images of good quality.^{40,47} To evaluate the performance of MNPs in MPI and their dynamic relaxation process it is used a relaxometer that measure the 1-dimensional PSF.⁴⁸ During the signal generation, MPI tracers must undergo a magnetization reversal, which requires overcoming viscous, thermal, and inertial torques by using a combination of Brownian and Néel relaxations.^{42,49} It relies on the same principles responsible of the MNPs heating in MHT. Therefore, a good tracer for MPI will be a good heating mediator in MHT, meaning that the imaging diagnosis and the treatment can be combined using the same MNPs.^{42,50,51}

Improving the magnetic properties of MNPs

The properties of the MNPs can be tuned by their size,^{52,53} surface,^{54,55} shape,⁵⁶⁻⁶⁰ assembly^{37,38,61} and composition.^{2,62} The majority of these characteristics should be obtained during the MNPs synthesis. For this reason, in the last decades a lot of work was done on the non-hydrolytic colloidal syntheses, as they uncovered the possibility to finely control size, composition and shape of MNPs.⁶³ To better understand the effect of composition on the magnetic nature of ferrite based NPs, it has to be investigated the magnetic ordering in its crystal lattice. This family of NPs belong to the crystallographic class of spinels. It can be represented by the general formula MFe_2O_4 , where M could be any of the divalent ions. The spinel ferrite structure has a face-centered cubic arrangement of oxygen atoms, with M^{2+} and Fe^{3+} occupying any of two different crystallographic sites. These sites have tetrahedral or octahedral oxygen coordination, which are often termed A and B-sites, respectively. In the unit cell, there are 8 A-sites and 16 B-sites, where the magnetic moments of the cations are aligned parallel with respect to each other. Between the A and B-sites, the magnetic ordering is anti-parallel and as there are twice as many B- sites than A-sites, there is a net moment of spins yielding ferrimagnetic ordering for the crystal.⁶⁴ IONPs has an inverse spinel structure, the 8 bivalent cations occupy 8 B sites and the 16 trivalent cations are distributed between 8 A and 8 B sites.⁶⁵ The peculiar properties of ferrites are strictly related to the distribution of cations between octahedral and tetrahedral sites in the spinel structure. The control of cation distribution provides a means to tailor their properties. In this way the, magnetic properties of iron oxide based NPs can be increased adding M^{2+} ions with higher idealized magnetic moment (i.e Mn) or adding non-magnetic ions (*i.e* Zn) lowering the antiferromagnetic coupling interactions between the Fe^{3+} ions in the A and B sites resulting in a net increase in magnetization.⁶⁶ Nowadays the most studied ferrite MNPs are the spherical IONPs due to their proved biocompatibility.^{67,68} The food and drug administration (FDA) has approved some spherical shaped for medical applications.⁶⁹ Unfortunately, these NPs are plagued by low values of M_s (due to large surface spin disorder)⁷⁰ which reduce their magnetic performance. It has been reported that non-spherical IONPs could improve their usefulness for bio-applications.^{57,69-71} Of particular interest are the cubic shape NPs resembling magnetosomes⁷², have demonstrate extremely high relaxivity as negative MRI contrast agents³⁷, high value of the SAR⁷¹ and high signal in MPI.⁴² Further, doping of other inorganic ions (as Co^{2+} , Zn^{2+} , Mn^{2+}) offers a great way to adjust the physical properties of magnetic ferrite NPs and their usefulness in applications.⁶² Among the family of spinel ferrites, cobalt ferrite has been widely

studied due to its interesting properties, which are strong magneto-crystalline anisotropy, moderate saturation magnetization, high coercivity, excellent chemical stability, good mechanical hardness and the highest value of magneto-striction.^{73,74} *Sathya et al.* had published a work on the synthesis of Co substituted ferrite NCs with tunable size and Co stoichiometry. These NCs of 20 nm exhibit outstanding r_2 relaxivity values ($985 \text{ mM}^{-1}\text{s}^{-1}$ at 0.5 T magnetic field and 19.95 MHz frequency) and SAR value of $915 \pm 10 \text{ W/g}_{(\text{Co+Fe})}$ at low frequency (105 kHz).⁷⁵ However, *Cabrera et al.* had recently showed that the heating ability of these NCs was suppressed when placed in a viscous environment²⁷, this and the intrinsic toxicity of cobalt⁷⁶ could limit their *in vivo* application. However, the toxicity of cobalt could be controlled by the NPs concentration and used for induce apoptosis in carcinogenic cells. The potential key advantage of Zn and Mn ferrite NPs is the reduced toxicity over Co. The Food and Drug Administration has set the reference daily intake (RDI) doses for Fe, Zn and Mn at 18, 15 and 2 mg/day, instead the Co RDI is 5-8 $\mu\text{g/day}$.⁷⁷ Concerning the zinc ferrite NPs, there are many studies on the synthesis and characterization for their application as contrast agent in MRI.⁷⁸⁻⁸² Despite to their poor size and shape distributions they showed good relaxivity values and improved sensitivity of detection.^{81,83} *Noh et al.* reported an interesting work on 40 nm $\text{Zn}_{0.4}\text{Fe}_{2.6}\text{O}_4$ NCs exhibiting high M_s (165 emu/g) and a maximum SAR of 4060 W/g.⁵⁴ Moreover, these NCs showed good performances as MPI tracer.⁴² Beyond that, some study were done in which a double ions substitution was done, in particular MnCo ferrite and ZnCo ferrite.⁸⁴⁻⁸⁷ It has been shown that the substitution of Co^{2+} by Zn^{2+} in CoFe_2O_4 NPs ($\text{Co}_{1-x}\text{Zn}_x\text{Fe}_2\text{O}_4$) could improve the properties of NPs, such as chemical stability, corrosion resistivity, magneto-crystalline anisotropy, magneto-striction and magneto-optical properties.⁸⁸⁻⁹⁰ *Ben Ali et al.* observed a significant decrease of coercivity from 2000 Oe to 170 Oe with increasing the zinc substitution.⁹¹ This variation can be attributed to the reduction of domain wall energy caused by the weak magneto-crystalline anisotropy of the zinc.⁹² They also reported a M_s for CoFe_2O_4 of about 61 emu/g with an average NPs size of 11.7 nm, while the value reported in the literature for bulk sample is about 81 emu/g.⁹³ However, the substitution of cobalt by zinc shows an increase in saturation magnetization up to reach about 75 emu/g for $\text{Co}_{0.7}\text{Zn}_{0.3}\text{Fe}_2\text{O}_4$.⁹¹ This is supported by the findings of *Wang et al.*; they showed that only moderate Zn substitution can enhance M_s and magnetic susceptibility.⁹⁴ Moreover, *Mameli et al.* showed a high M_s of 94 emu/g obtained by 7 nm ZnCo ferrite NPs having the same stoichiometry of above ($\text{Co}_{0.7}\text{Zn}_{0.3}\text{Fe}_2\text{O}_4$).⁹⁵ While, the influence of the Mn substitution on magnetic properties of the CoFeNPs has not been widely studied so far, especially for using in biomedical applications, *Topkaya et al.* reported that the M_s for $\text{Mn}_x\text{Co}_{1-x}\text{Fe}_2\text{O}_4$ NPs remains

almost the same when x is between 0 and 0.4. This results was similar to the ones achieved by *Ranvah et al.*^{96,97} Afterwards, with the increase in the Mn concentration ($x = 0.6$), the magnetization reaches a maximum value of about 60 emu/g.^{86,98} This higher M_s value can be suitable for biomedical applications. The reason of the increasing of the saturation magnetization at higher stoichiometry of Mn than Co may be that the substitution of Mn ions by Co ions in octahedral sites of the inverse spinel ferrite structure⁶⁵ increases the magnetization as the magnetic moments of Mn^{+2} and Co^{+2} are 5 and 3 μ_B , respectively.

1.2 Results and discussion

1.2.1 Optimization of CoFeNCs synthesis

The experimental parameters were set considering previously reported synthesis by our group, to obtain CoFeNCs of 15-27 nm in cube-edge (see experimental section).⁶³ Despite the high SAR value measured in water for CoFeNCs at this size range, their strong interparticle interactions might limit their application in biological environment. Therefore, the goal of this study was to synthesize smaller NCs (size <15 nm and a Co to Fe ratio of about 0.6) in order to reduce such interactions between NCs. There are several parameters affecting the cube's size and the cobalt to iron ratio in their composition. Particular attention was given to the vacuum control. In fact, it was found a correlation between the vacuum levels reached at the end of the degassing step and the quality of the NCs. Using a vacuum pump with higher performances (increased level of vacuum and power) than before, allowed reaching vacuum values close to 15 μ Bar instead of the common 25 μ Bar in the same lapse (1.5 h). The resulting CoFeNCs obtained using this pump were more stable over time in organic solvent, preventing aggregation, with a well-defined cubic shape (Figure 8b).

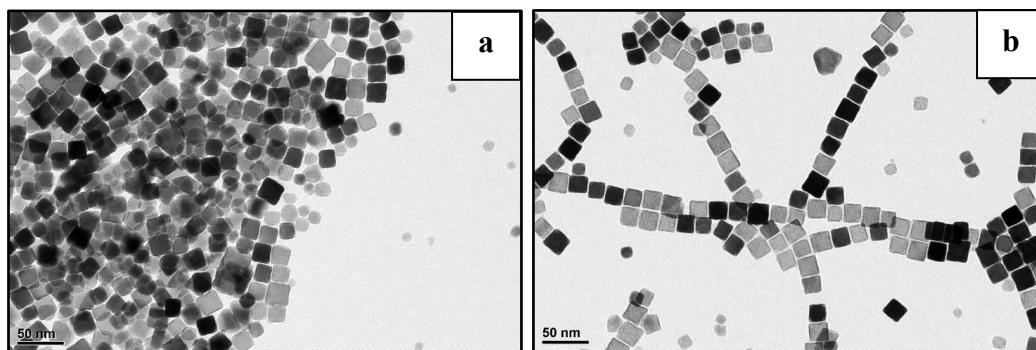


Figure 8 TEM images of CoFeNCs synthesized using: **a)** 25 μ Bar and **b)** 15 μ Bar of vacuum level. Both samples are 18 nm in cube-edge with a standard deviation of **a)** ± 4 nm **b)** ± 2 nm.

Moreover, when the solution was kept at 305°C a turbulent boiling (refluxing of the solution along the condenser) could be observed during the last hour of the synthesis. This resulted in low quality NCs in terms of shape and size distribution. Such behavior was ascribed to a poor temperature distribution inside the solution and the extremely high boiling point for the correct growth of the crystals. Therefore, the amount of squalane was increased to 12 mL (from 10 mL)(Figure 9a). This solvent has a higher boiling point than the dibenzyl ether used as co-

solvent. Thus, increasing the amount of squalane the boiling point of the mixture was increased and less refluxing was observed. To have a better temperature distribution a bigger flask (100 mL) rather than the standard 50 mL flask was used, allowing a larger surface contact between the solution and the outer heating mantle.

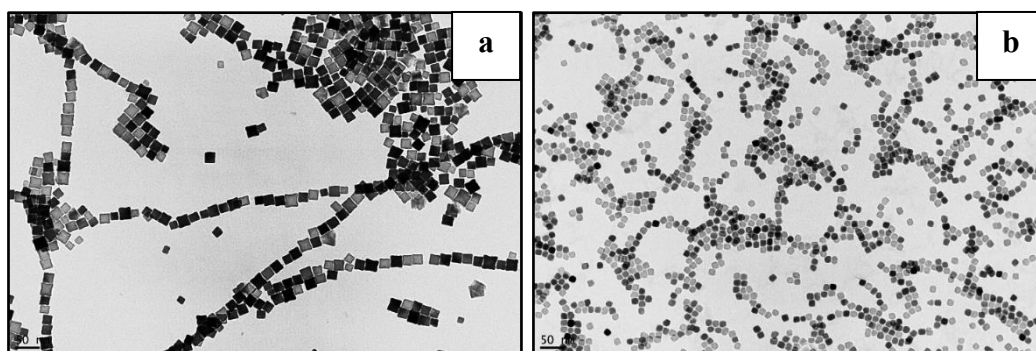


Figure 9 TEM images of CoFeNCs with **a**) higher amount of squalene (12 mL instead 10 mL) and **b**) with bigger flask (100 mL instead 50 mL). The NCs size are 16 ± 2 nm and 12 ± 1 nm, respectively.

The sample synthesized in the 100 mL flask (Figure 9b) exhibits a uniform shape and size distribution. Noticeable, the size measured for these CoFeNCs, 12 ± 1 nm (see Figure A1 in appx.), is smaller than the expected one (18 ± 2 nm), considering the synthesis done with the 50 mL flask under the same conditions (Figure 10a).

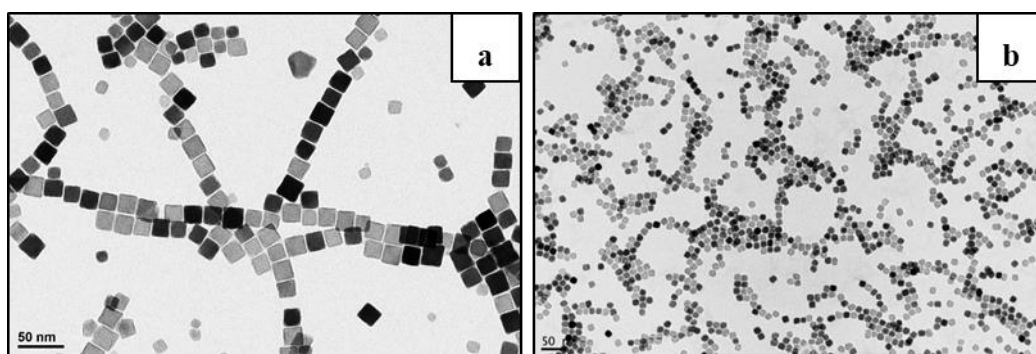


Figure 10 TEM images of CoFeNCs synthesized using: **a**) 50mL flask and **b**) 100mL flask the other synthesis parameters were the same. Both samples are in cube-edge with a size of **a**) 18 ± 2 nm and **b**) 12 ± 1 nm.

The optimized synthesis was repeated four times to assess the reproducibility, obtaining particles of about 12 nm with a standard deviation of 3nm. Finally, a set of syntheses were performed to obtain NCs of different sizes below 15 nm. Another parameter essential for the control over size was the N₂ flow. The nitrogen pressure into the schlenk line was set to 2 Bar

and the flow was controlled by counting the bubbles per minute into the bubbler connected to the synthesis flask placed at the exit of the gas stream. Using fast flow rate (more than 120 bubble per minute) the NCs size was 15 nm (Figure 11a). When the flow rate was drastically decreased to few bubbles per minute (5-10 bubbles per min), CoFeNCs of 8 nm were obtained (Figure 11d). Setting the bubble rate to an intermediate speed, specifically 80 and 40 bubbles per minute, the NCs reached a size of 14 nm and 12 nm (Figure 11b and c), respectively.

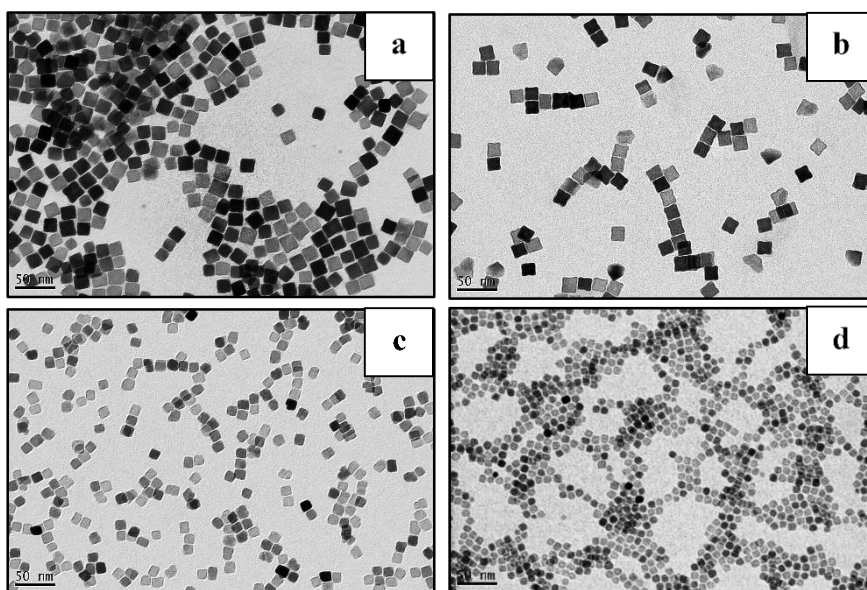


Figure 11 TEM images of CoFeNCs synthesis controlling the nitrogen flow rate: **a)** >120 bubbles per minute, **b)** 80 bubbles per minute, **c)** ~40 bubbles per minute and **d)** 5 bubbles per minute leading to 15 ± 2 , 14 ± 2 , 12 ± 1 and 8 ± 1 nm NCs.

1.2.2 Water transfer of CoFeNCs with polymer coating technique

The design of advanced colloidal NPs for biological applications should involve the exploitation of suitably coatings to enable the water transfer and the further functionalization with functional molecules. At the same time, the outer coating has to protect the NPs surface from degradation in the physiological environment, provide biocompatibility and confer compelling colloidal stability in biological environment while enabling proper outer functionalization (e.g. PEG and/or targeting molecules).⁹⁹⁻¹⁰¹ The water transfer protocol with amphiphilic polymer developed by our group,¹⁰⁰ gives excellent results with spherical, cubic and rod-shape iron oxide NPs. In case of CoFeNCs (and for the other ferrite NCs in this chapter) some modifications have been performed in order to obtain a colloidal stable solution. The procedure starts with mixing the NPs and the poly(maleic anhydride-*alt*-1-octadecene)

(PMAO) in chloroform. Then, the chloroform of the obtained solution has to be evaporated to re-disperse in water the NPs capped in the polymer shell. The evaporation step is critical to obtain a high quality coating of the NPs. In this way, to gently evaporate the chloroform and provide individually coated NCs with the PMAO, the pressure of the rotavapor was decreased following a three steps evaporation: 800 mBar for 30 minutes, 700 mBar for 30 minutes and finally 600 mBar until complete solvent evaporation was achieved. In addition, the water bath temperature was kept at 50 °C with a continuous rotation at 140 rpm. This caution prevents CoFeNCs aggregation rendering them well dispersed in aqueous medium. The optimized procedure, reported in the experimental section, is suitable for CoFeNCs with a cubic edge from 8 to 18 nm. After ultracentrifugation, the nanoparticles were found as a uniform layer in the 40% phase of the sucrose gradient, meaning that the polymer coated CoFeNCs maintained a good size distribution and were individually coated (Figure 12a). From Figure 4b is possible to detect the excess of PMAO in ultracentrifuge tube as a blue band under UV light on the top of the sucrose gradient. There were no NCs co-localization with the polymer layer, confirming that NPs were well purified.

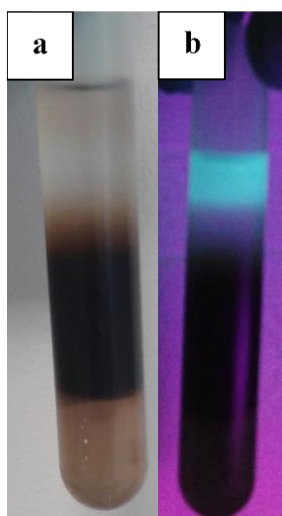


Figure 12 Pictures of CoFeNCs in sucrose gradient after ultracentrifugation: CoFeNCs sample is visible thanks to the dark color of the nanoparticle in the middle gradient of **a**) sucrose under visible light and **b**) excess of polymer(PMAO) is detected under UV light as a blue band.

Moreover, to reduce the overall time spent for washing the NCs, a pressure ultrafiltration concentrator (Vivacell 250, Sartorius) was used instead of the standard filter for centrifugation (Amicon tube, Millipore). This device allowed the dispersion of the samples in bigger volumes (max 250 mL) during the washing step and avoiding the particle aggregation that often

occurred when concentrating the samples with the standard filters. The modified procedure allowed the water transfer of larger volumes of CoFeNCs improving the sample's quality. In the end well dispersed NCs in water, not aggregated and completely free from excess of polymer were obtained. In Figure 13 is visible the characterization of a CoFeNCs sample (12 ± 2 nm). As it is visible the sample is single coated and well dispers in water (Figure 13 a). The image of the agarose gel after the electrophoresis show a defined band with no tail, indicating a narrow size distribution of the NPs (Figure 13 b-c). This result was confirmed by the DLS measurements, in which the PDI is low (0.145) and the hydrodynamic size by intensity is 31 ± 1 nm (Figure 13 d-e).

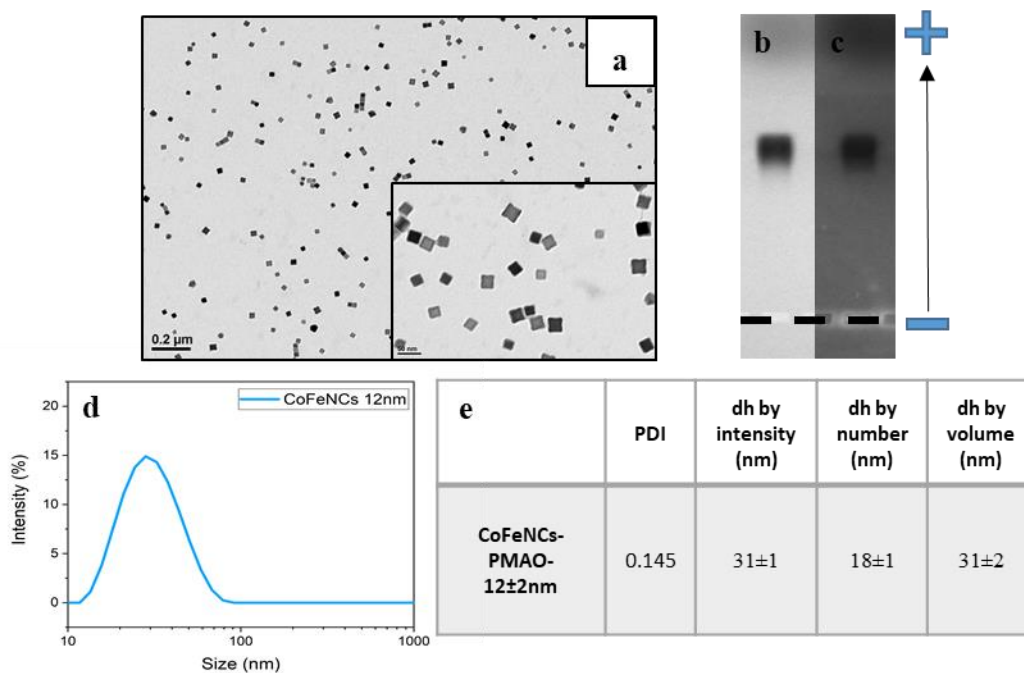


Figure 13 TEM images of the **a**) polymer coated CoFeNCs sample in water, **b-c**) image of electrophoresis run characterization at 100V for 45min in TBE the sample was loaded on a 2% agarose gel. Images were taken under visible and UV light DLS characterization: **d**) graph of distribution of hydrodynamic diameter by intensity and **e**) DLS data table (each value is the result of three measurements repetition).

1.2.3 SAR characterization & AC Hysteresis loops of CoFeNCs

Since the goal of this study was to exploit the potential of CoFeNCs for magnetic hyperthermia providing an efficient heat treatment, their magnetic properties were investigated. Thus, the SAR and AC Hysteresis loops (ACHLs) values for CoFeNCs of different sizes (8-11-14-15 nm) were recorded (see Figure A5 and A6 in appx.). IONCs of 15 nm were used as reference. Interestingly, the best SAR performances were obtained for the smaller CoFeNCs at 100 kHz (Figure 13a), which were four times higher than those recorded for IONCs. The heat ability seems to decrease with particles size increase. The SAR data recorded when the 300 kHz frequency was applied showed a similar trend (Figure 14b). The invariance of CoFeNCs SAR with respect to the frequency was already noticed by *Sathya et al.* in case of bigger NCs (17 and 20 nm).⁶³ Comparing the values obtained for the CoFeNCs with those for IONCs, it was clear their different response to the AMF. CoFeNCs did not show significant variations in the SAR obtained for different frequencies while IONCs revealed an increase of almost 4-folds in the SAR once the frequency was increased. On the contrary, the CoFeNCs were more sensitive to the field raise. These results render the CoFeNCs interesting for applications in which low frequency AMF is required.

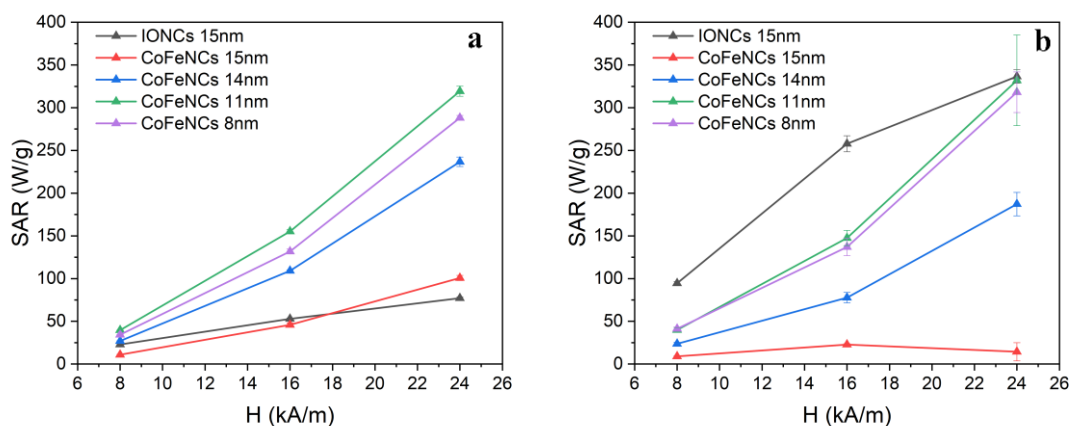


Figure 14 SAR measurements graphs of different sizes of CoFeNCs (15±2, 14±2, 11±1 and 8±1 nm) and IONCs (15±2 nm). The measurements were done with a field of 8-16-24 kA/m and a) 100kHz, b) 300kHz.

The response of the NCs to the AMF applied frequency was even more evident from their ACHLs. The ACHLs were recorded by an AC magnetometer. Herein, hysteresis loops at

24 kA/m and frequency ranging from 50 kHz to 300 kHz for 12 nm CoFeNCs and 15 nm IONCs are reported (Figure 15 a and b). The loops for the CoFeNCs were closing and becoming flat with the increase of frequency from 50 kHz to 300 kHz (Figure 15a). This might be explained by their difficulty to follow the AC magnetic field and it is consistent with the dynamic hysteresis simulations done by *Verde et al.*¹⁰² On the other hand, for the IONCs the ACHLs recorded were opening with the increase in the frequency applied (Figure 15b). These results are in accordance with those obtained from the SAR measurements.

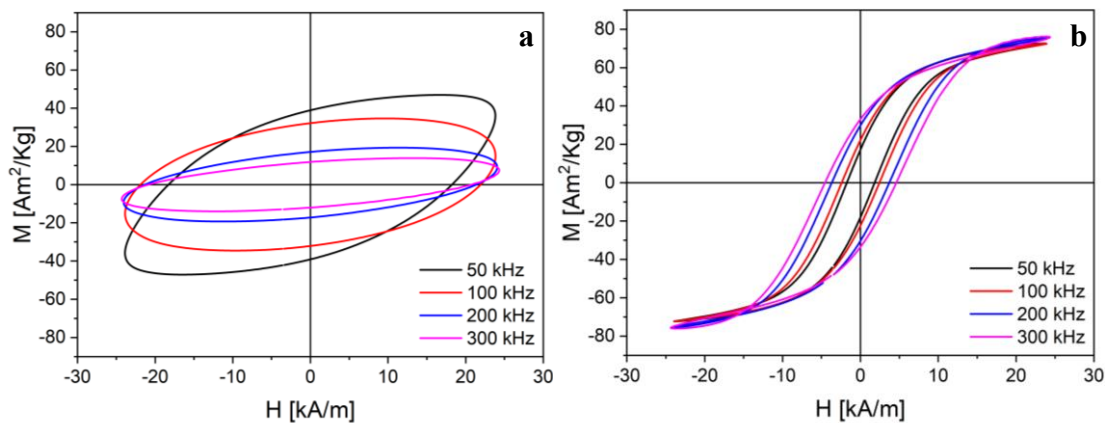


Figure 15 AC hysteresis loops of **a)** CoFeNCs 12±1 nm and **b)** IONCs 15±2 nm recorded at fixed field 24kA/m and different frequency: 50 kHz, 100 kHz, 200 kHz and 300 kHz.

1.2.4 CoFeNCs in Matrigel environment: simulation of a tumor injection

To evaluate the behavior of the CoFeNCs when placed in the biological environment, an experiment was designed in which the NCs were embedded in a Matrigel matrix. A Matrigel matrix is a gel protein mixture and it simulates the conditions found by the NCs when injected at the tumor mass. Thus, a Matrigel cast (500 μ L) was prepared, leaving a hole in the centre to place the NCs solution. Once it was jellified after 1 h at 37 °C, the NCs (17±2 nm, 2 μ L at 11 g/L) were added and then the mold was closed using another volume of 500 μ L of gelatin protein mixture. The model was left jellify for 1 h at 37°C and then subjected to three MHT cycles of 30 min each (120 kHz – 20 kA/m) (Figure 16). It was also tried, the direct injection of NPs into the jellified Matrigel. In this case, first was produced a cylindrical Matrigel gel and was left jellify for 1 h at 37°C. Then, the NPs were injected into the gel using a small needle. Unfortunately, the stiffness of the protein matrix was too high and it breaks under the syringe pressure, resulting in the NPs leakage.

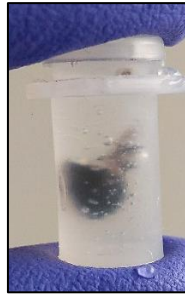


Figure 16 Image of the tumor mass model simulated with Matrigel. The black spot in the center of the cylinder is formed by the CoFeNCs($17\pm 3\text{nm}$, $2\ \mu\text{L}$ at $11\ \text{g/L}$) embedded into the gelatin protein mixture ($1\ \text{mL}$).

From Figure 17 it is possible to observe the infrared images of the matrigel placed into the MHT applicator. No temperature increase was recorded for the CoFeNCs-matrigel sample during the MHT treatment, even when the highest frequency was applied (300 kHz). This suggests that the high viscosity of the matrigel drastically affects the heating ability of Co ferrite NCs even when they have a 17 nm cube edge.²⁷ The actual decrease in temperature measured during MHT exposure time, observable in the figure, was given by the cooling system of the device and the equilibration of the sample with the room temperature ($21\ ^\circ\text{C}$).

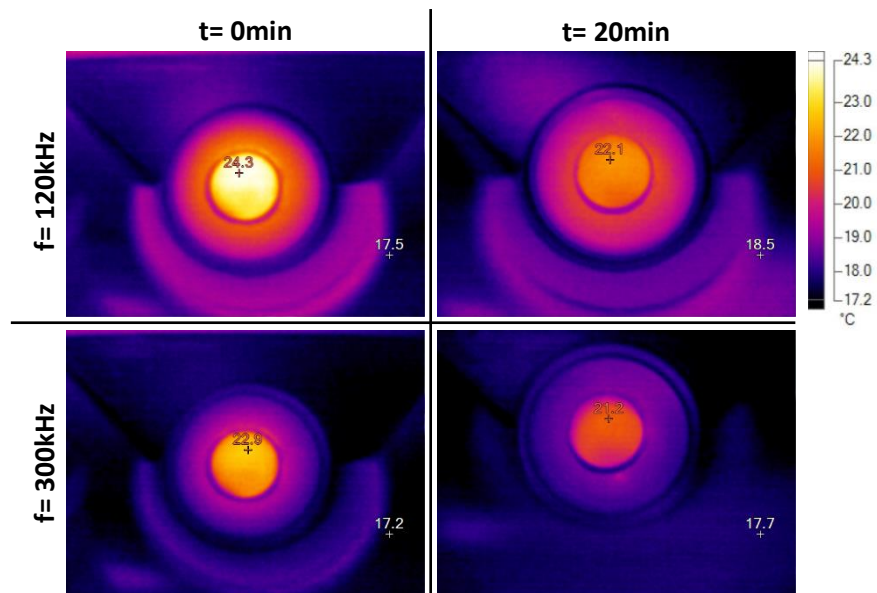


Figure 17 Infrared images of the Matrigel model loaded with CoFeNCs($17\pm 3\text{nm}$, $2\ \mu\text{L}$ at $11\ \text{g/L}$) placed into the MHT applicator. The images are taken at time 0 and after 20 min during the application of a field of $20\ \text{kA/m}$ and two different frequency 120 and 300 kHz. The red marker represent the highest temperature on the images and the white is the control temperature outside the device.

After the MHT, the model was fixed in resin and cut to be analyzed by TEM. The images at TEM were need to understand the aggregation state of the NPs in to the Matrigel matrix. No aggregations of NPs were observed but it was shown that the 17 nm CoFeNCs were forming organized chain-like structures under the MHT (Figure 18).

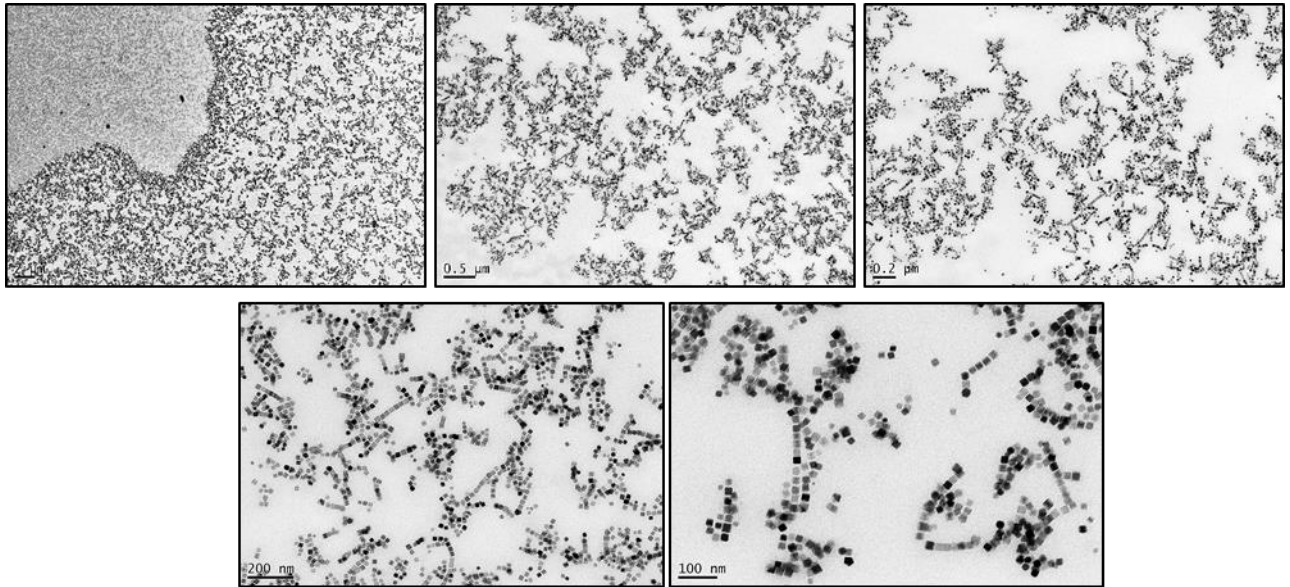


Figure 18 TEM images of the CoFeNCs ($17\pm 3\text{nm}$) in Matrigel. The images differs for the magnification. It is visible the formation of chain-like structures and no other aggregation occurs.

1.2.5 Synthesis of Zinc ferrite nanocubes

The synthesis of ZnFeNCs ($\text{Zn}_x\text{Fe}_{3-x}\text{O}_4$) was a follow-up of the optimized synthesis of CoFeNCs. The relevant parameters fixed for the synthesis of CoFeNCs made easier the replacement of cobalt ions to zinc ions for the zinc-substituted ferrite. The goal of the work was to obtain nanocubes under 15 nm in size with optimal size and shape distribution. Given the successful results obtained for the synthesis of CoFeNCs from 8-15 nm, the procedure was reproduced under the same conditions for the trials with the new Zn divalent ions. The ZnFeNCs were obtained but there was still space for refinement to improve their size and shape distributions. Therefore, a series of synthesis were done (Figure 19), varying systematically the amount of surfactant (Decanoic acid) from 6 mmol to 8 mmol while all the other parameters (1 mmol of $\text{Fe}(\text{acac})_2$, 0.5 mmol of $\text{Zn}(\text{acac})_2$, 13 mL of dibenzyl ether and 12 mL of squalane) were kept constant as detailed in the experimental section.

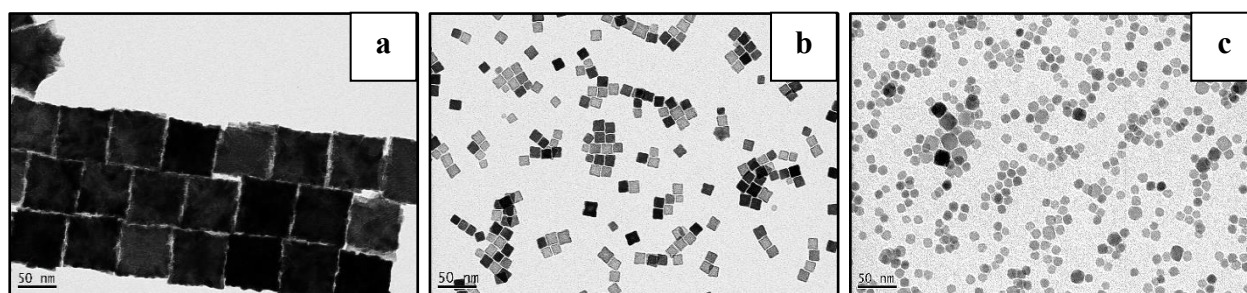


Figure 19 TEM images of ZnFeNCs synthesis varying the amount of decanoic acid: **a)** 6mmol **b)** 7mmol and **c)** 8mmol lead to $65\pm 5\text{nm}$, $12\pm 1\text{nm}$ and $8\pm 6\text{nm}$ ZnFeNCs.

As it is visible from Figure 19, the surfactant plays a fundamental role in the NCs growth. When 6 mmol of decanoic acid were used (Figure 19a), the synthesis gave NCs with good size and shape distribution but bigger than expected (65 nm). This sample showed an irregular surface probably coming from the agglomeration of the seeds in the early stage of the synthesis. On the contrary, when were used 8 mmol the control over quality was lost obtaining NCs with irregular size and cubic shape distribution (Figure 19c). Therefore, the amount of decanoic acid chosen to obtain the desired NCs was set at 7 mmol and the surfactant to metal ratio was kept at 4.7 (Figure 19b). The synthesis was repeated 4 times to evaluate its reproducibility. The obtained particles with average size of 12 nm (see Figure A1 in appx.) and a Zn fraction of about 0.18 ($\text{Zn}_{0.18}\text{Fe}_{2.82}\text{O}_4$) revealed a well-defined cubic shape as intended (Figure 19b).

1.2.6 Synthesis of zinc-cobalt ferrite and manganese-cobalt ferrite nanocubes

The aim of this work was to obtain enlarge the portfolio of NPs having a cubic shape and different composition to then study their performances in MHT, MPI and MRI. Thus, the synthesis of mixed ferrite in which were introduced two metal ions simultaneously (either zinc and cobalt or manganese and cobalt) were tried. The parameters used for the synthesis of CoFeNCs was adopted, the only differences were the use of Mn(II) and Zn(II) acetylacetonates precursors in in addition to the cobalt, maintaining the same ratio between surfactant and metals (4:1). As reported in Figure 20c, the first trial provided 15 nm NCs having a narrow shape distribution and a $Zn_{0.1}Co_{0.19}Fe_{2.71}O_4$ composition. A set of experiments were further done changing the starting concentrations of Zinc(acac)₂ and Cobalt(acac)₂ in the feeding reaction pot, leaving constant all the other parameters, in particular, the amount of Iron(acac)₃ (1 mmol) and the surfactant to metal ratio (4:1).

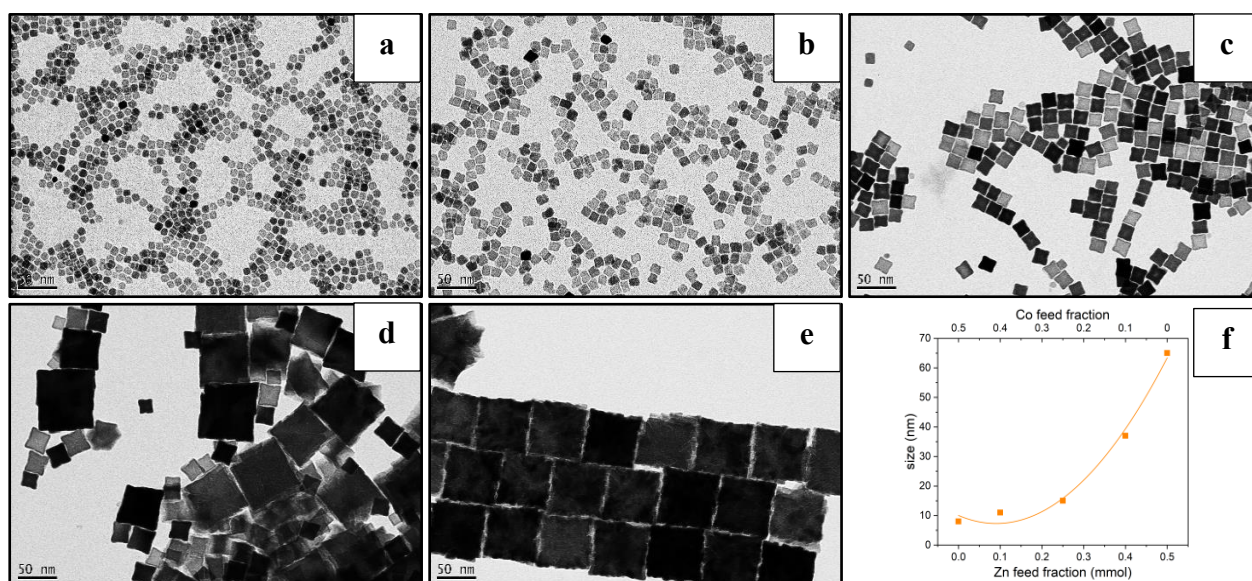


Figure 20 TEM images of ZnCoFeNCs varying the Co to Zn feed molar ratios: **a)** only Co **b)** Co:Zn at 4 **c)** 1 **d)** 0.25 and **e)** only Zn, lead to 8 ± 1 nm CoFeNCs, 11 ± 1 nm ZnCoFeNCs, 15 ± 1 nm ZnCoFeNCs, 40 ± 18 nm ZnCoFeNCs and 65 ± 5 nm ZnFeNCs and **f)** graph of the size trend. The size increase is controllable by tuning the metal precursor's concentrations. Lines are drawn just to guide the eye and do not represent a mathematical fit.

Interestingly, it was found that increasing the amount of zinc precursor in comparison to the cobalt it gave a size increase from 8 to 65 nm (see Figure A2 in appx.). Moreover, the Co to Zn ratio found by elemental analysis, after the synthesis, was nearly doubled from that used as feeding and seemed to be reproducible for all syntheses. This indicates that the two ions can

enter into the NCs in a well-defined amount, which could be predicted during the experiment design. These data suggest that by controlling the metal precursors concentrations it was varied the size of the synthesized NCs and the metal composition of the nanocrystals.

Table 1 Summary of the different synthetic parameters used for the synthesis of ZnCoFeNCs, size and final stoichiometry for the NCs reported in 20.

| Panel of Figure 19 | Iron feed concentration [mmol] | Co/Zn feed ratio (Initial) | Co/Zn ratio by ICP (final) | NCs stoichiometry $Zn_xCo_yFe_{3-(x+y)}O_4$ | Size by TEM [nm] |
|--------------------|--------------------------------|----------------------------|----------------------------|---|------------------|
| a | 1 | - | - | $Co_{0.65}Fe_{2.35}O_4$ | 8 ± 1 |
| b | 1 | 4 | 7.8 | $Zn_{0.06}Co_{0.47}Fe_{2.47}O_4$ | 11 ± 1 |
| c | 1 | 1 | 1.9 | $Zn_{0.1}Co_{0.19}Fe_{2.71}O_4$ | 15 ± 1 |
| d | 1 | 0.25 | 0.8 | $Zn_{0.13}Co_{0.11}Fe_{2.48}O_4$ | 40 ± 18 |
| e | 1 | - | - | $Zn_{0.27}Fe_{2.73}O_4$ | 65 ± 5 |

Following the procedure described above, the Zn precursor was replaced by manganese precursor (we chose as precursor manganese(II) acetylacetonate) and the same set of syntheses were repeated. The results obtained clearly showed an opposite behavior for the presence of Mn comparing to Zn. In this case, the increase of Mn metal precursor led to the decrease the size of the NCs (see Figure A3 in appx.) (see Figure 20). As reported above (Table 1) for the Co to Zn ratio, the Co to Mn ratios in the NCs were doubled with respect to the feeding ratios (Table 2). This result confirms the possibility to predict the final metal ions ratio.

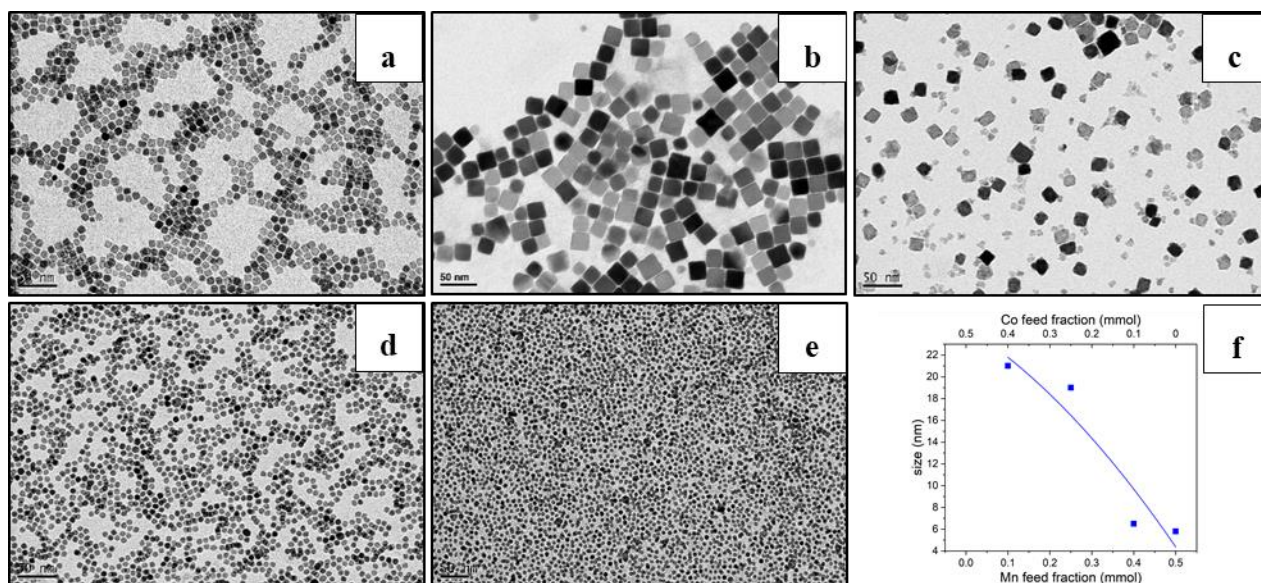


Figure 21 TEM images of MnCoFeNCs varying the Co to Mn feed molar ratios: **a)** only Co used as control **b)** Co:Mn at 4 **c)** 1 **d)** 0.25 and **e)** only Mn, lead to 8 ± 1 nm CoFeNCs, 12 ± 2 nm MnCoFeNCs, double population in which the main one is 19 ± 4 nm MnCoFeNCs, 6.5 ± 0.5 nm MnCoFeNCs and 5.5 ± 0.5 nm MnFeNCs and **f)** graph of the size trend. The size decrease is controllable by tuning the metal precursors concentrations. Lines are guide to the eye.

Table 2 Summary of the different synthetic parameters used for the synthesis of MnCoFeNCs, size and final stoichiometry for the NCs reported in of 21.

| Panel of Figure 20 | Iron feed concentration [mmol] | Co/Mn feed ratio (initial) | Co/Mn ratio by ICP (final) | NCs stoichiometry $Mn_xCo_yFe_{3-(x+y)}O_4$ | Size by TEM [nm] |
|--------------------|--------------------------------|----------------------------|----------------------------|---|------------------|
| a | 1 | - | - | $Co_{0.65}Fe_{2.35}O_4$ | 8 ± 1 |
| b | 1 | 4 | 7.8 | $Mn_{0.06}Co_{0.47}Fe_{2.47}O_4$ | 21 ± 2 |
| c | 1 | 1 | 2.3 | $Mn_{0.16}Co_{0.36}Fe_{2.48}O_4$ | 19 ± 4 |
| d | 1 | 0.25 | 0.43 | $Mn_{0.86}Co_{0.37}Fe_{1.77}O_4$ | 6.5 ± 0.5 |
| e | 1 | - | - | $Mn_{0.6}Fe_{2.4}O_4$ | 5.5 ± 0.5 |

Figure 21c, which represents the results for the synthesis in which the two metal precursors were added at the same concentration (0.25 mmol), shows clearly two populations of NCs one with a mean size of 19 ± 4 nm and one at 6 ± 3 nm. One can speculate about the contemporary nucleation of MnCo ferrite and manganese oxide NPs. Therefore, another set of syntheses was performed modifying the surfactant to metal ratio from 4:1 to 3.33:1 and 3:1, using equal concentrations of metal precursors and leaving constant the $Fe(acac)_3$ (1 mmol).

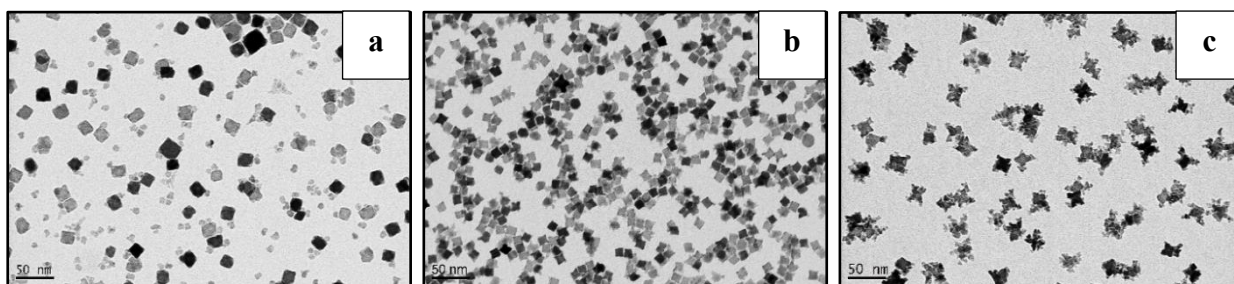


Figure 22 TEM images of MnCoFeNCs varying the surfactant to metal ratio: **a)** 4:1, **b)** 3.33:1 and **c)** 3:1 leading to 19 ± 2 nm, 10 ± 1 nm and 15 ± 4 nm MnCoFeNCs. With the decrease of the surfactant to metal ratio the NCs morphology changes.

The TEM results (Figure 22) showed that by increasing the amounts of the metal precursors the NCs become hetero-structures, in which spherical like structure were forming at the corner of a nanocube.

1.2.7 Structural and magnetic characterization

Structural characterization

In order to characterize structurally the synthesized materials, groups of representative size-dependent X-Ray diffraction (XRD) patterns of the different ferrites nanocubes were analyzed. The position and relative intensity of all diffraction peaks, shown in Figure 23, match well with standard diffraction data of ferrites of magnetite Fe_3O_4 powder (JCPDS card no. 00-001-1111). No impurity phases were visible as reported instead in previous works on cobalt-substituted magnetite NCs prepared by thermal decomposition.¹⁰³

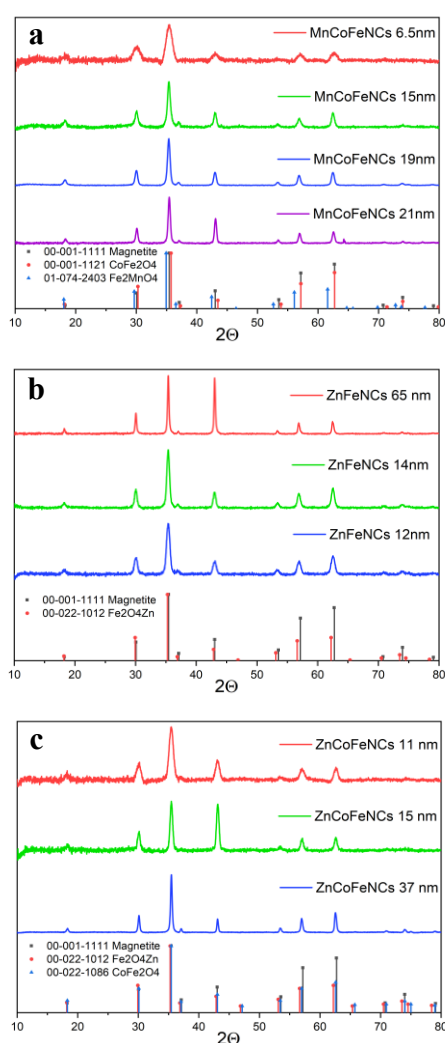


Figure 23 Groups of size-dependent XRD patterns of the different ferrite NCs; a) ZnFeNCs, b) ZnCoFeNCs and c) MnCoFeNCs.

Detailed compositional analyses were then performed by X-ray spectroscopy in scanning transmission electron microscopy (STEM-EDS) on a 12 ± 1 nm $\text{Zn}_{0.2}\text{Fe}_{2.8}\text{O}_4$ nanocubes sample,

on a 15 ± 2 nm $\text{Zn}_{0.1}\text{Co}_{0.19}\text{Fe}_{2.71}\text{O}_4$ nanocubes sample and on 10 ± 1 nm $\text{Mn}_{0.14}\text{Co}_{0.66}\text{Fe}_{2.20}\text{O}_4$ nanocubes sample. The Zn, Co and Mn stoichiometries were estimated over large groups of NCs for each samples (see Table A1 in appx.) and the results match the stoichiometries found by elemental analysis by ICP on samples solutions. The ions distributions within the NCs were analyzed by STEM-EDS elemental mapping (Figure 24). For all samples, EDS elemental maps indicated a homogeneous distribution of Fe within the NCs, whereas the distribution of the other ions was less homogenous and evidenced an enrichment of Zn, Mn and Co closer to the surface.

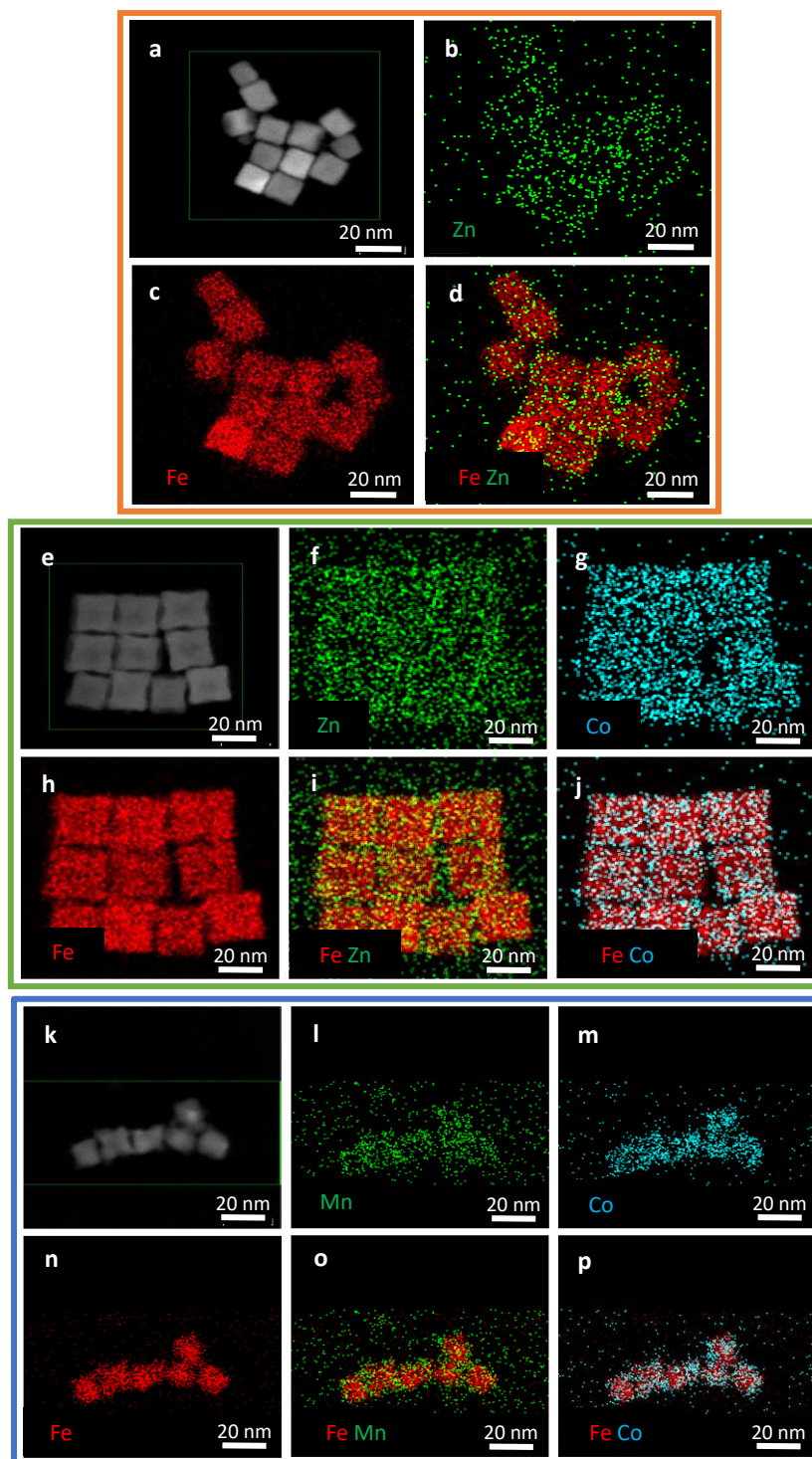


Figure 24 Compositional analysis of three samples of mixed ferrite nanocubes, i.e. $\text{Zn}_{0.2}\text{Fe}_{2.8}\text{O}_4$ (red square), $\text{Zn}_{0.1}\text{Co}_{0.19}\text{Fe}_{2.71}\text{O}_4$ (green square) and $\text{Mn}_{0.14}\text{Co}_{0.66}\text{Fe}_{2.20}\text{O}_4$ (blue square). (a, e, k) Zero-loss filtered TEM image of nanocubes in each sample and (d, i, j, o, p) combination of corresponding EFTEM elemental maps for Fe (red), Co (blue) and Zn or Mn (green). The Fe, Zn, Mn and Co maps are shown separately in (b, c), (f, g, h) and (l, m, n) respectively, for the sake of clarity.

Although no secondary phases were detected from the XRD pattern, it should be said that a low volume fraction of the Co, Zn and Mn-rich phase at the NC surface (which may go

unnoticed in XRD) could still significantly affect the magnetic properties.⁶³ Moreover, High resolution TEM (HRTEM) of the three mixed ferrite samples (Figure 25) are showing ferrite phases that matches those found by XRD, in each samples there are no appreciable changes in lattice parameters along the cubes volume

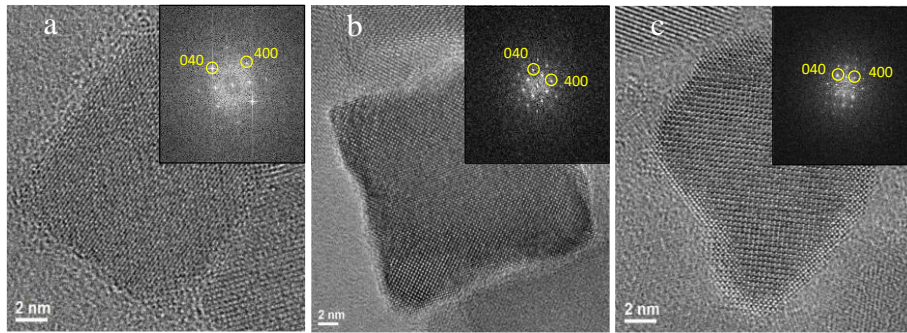


Figure 25 HRTEM images of three samples of mixed ferrite nanocubes, **a)** $Zn_{0.2}Fe_{2.8}O_4$, **b)** $Zn_{0.1}Co_{0.19}Fe_{2.71}O_4$ and **c)** $Mn_{0.14}Co_{0.66}Fe_{2.20}O_4$. It is also reported the 2D fast Fourier transform. The measurements over the crystalline structure matches with the ferrite structure.

Magnetic characterization

Hysteresis loops with finite coercive fields (H_c) and temperature dependent magnetization were recorded on the NCs samples of various sizes and composition (Figure 26). The 12 ± 1 nm ZnFeNCs sample was characterized by a really low coercive field and high saturation magnetization at both 300K and 10K, being superparamagnetic at 300 K.

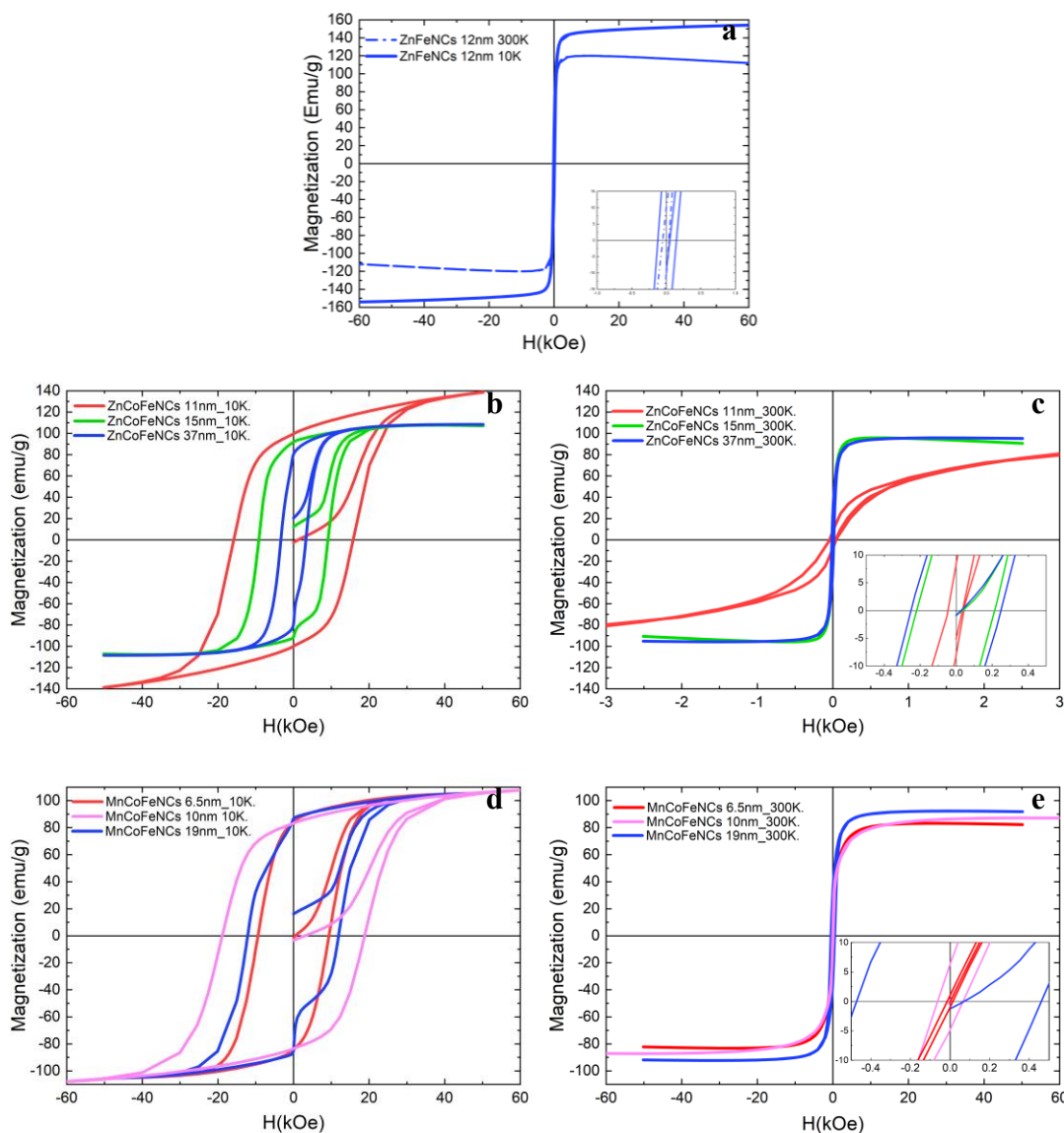


Figure 26 Magnetization vs applied magnetic field curves for different ferrite samples: **a)** ZnFeNCs 12 ± 1 nm, size dependency magnetization curves of ZnCoFeNCs at 10 K **b)** and 300 K **c)**, Size dependency magnetization curves of MnCoFeNCs at 10 K **d)** and 300 K **e)**. All curves were normalized to the amount of material measured using ICP analysis.

Once introduced the cobalt ions into the NCs structure (ZnCoFeNCs) the superparamagnetic behavior was still present at 300 k for the 11 nm sample but a drastically increase of the H_c was

observed (20 kOe). This value is almost two orders of magnitude higher with respect the one recorded for ZnFeNCs (150 Oe). Such increase is ascribed to the increase in magnetic anisotropy related to the presence of cobalt ions in the structure.^{104,105} The H_c trends of the ZnCoFeNCs followed the expected trend, increasing the amount of Co ions the H_c increased at 10 K. These conclusions can only be drawn at 10 K where all samples are far below their superparamagnetic regime. At 300 K, H_c does strongly depend on the size and hence no conclusion can be done comparing NCs of different sizes and compositions. The same trends were found in case of the MnCoFeNCs samples. Moreover, samples between 15 nm and 20 nm (either ZnCo and MnCo ferrites) at low temperature were characterized by a spring-magnet behavior as the result of a soft-hard magnetic coupling. In general, such behavior could be ascribed to the formation of core-shell structures.¹⁰⁶ In the present, no evidence of core-shell structures from TEM has observed. Still it was evident from TEM that the MnCoFeNCs sample had a double population, which could induce such behavior, although is very unlikely. On the other hand, the ZnCoNCs sample had narrow size distributions, with no other impurity phases from XRD analysis, which rules out the possibility of having an important contribution coming from another magnetic structure. Still, since Mn and CoFeNCs are soft and hard magnets respectively, it is very likely that the distribution of Co inside the NC is not homogenous. This is supported by the elemental mapping in which was visible an enrichment of dopant ions on the surface of the NCs. The magnetic characterization of CoFeNCs and MnFeNCs is reported in Figure A4 in appendix.

1.2.8 SAR and AC magnetic measurements

All the following characterizations were performed for the NCs transferred in water. The water transfer was done following the procedure explained in the experimental section (Phase transfer of the NCs in water with poly(maleic anhydride-alt-1-octadecene)). The heating performances of the different ferrite NCs were evaluated by measuring the increase of temperature over time under an applied AC field. The measurements were done using 300 μ L of NCs solution at a fixed concentration of 3 g/L. The evaluation of the SAR performances showed immediately that the NCs composition has a strong influence on the heating performances. The SAR values of cobalt based NCs were almost frequency independent, while SAR increases with the frequency for IONCs and especially for ZnFeNCs (Figure 27).

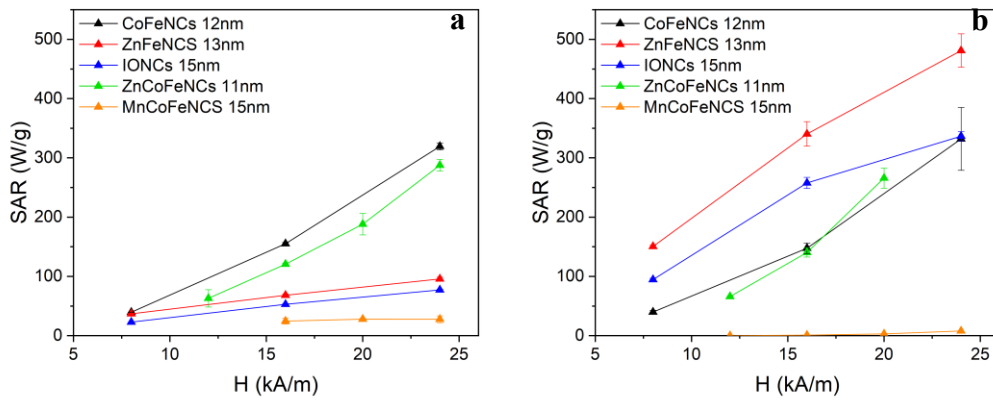


Figure 27 SAR values of the different ferrite nanocubes of comparable sizes at different field, graphs applying: **a)** 100kHz and **b)** 300kHz

A concomitant study of the SAR behavior was performed with AC magnetic hysteresis loops (ACHLs) measurements, for the cases in which the different response to the frequency changes were more evident. Herein, the ACHLs were measured at 24 kA/m varying the frequency of the AMF from 50 kHz to 300 kHz for IONCs, CoFeNCs and ZnFeNCs.

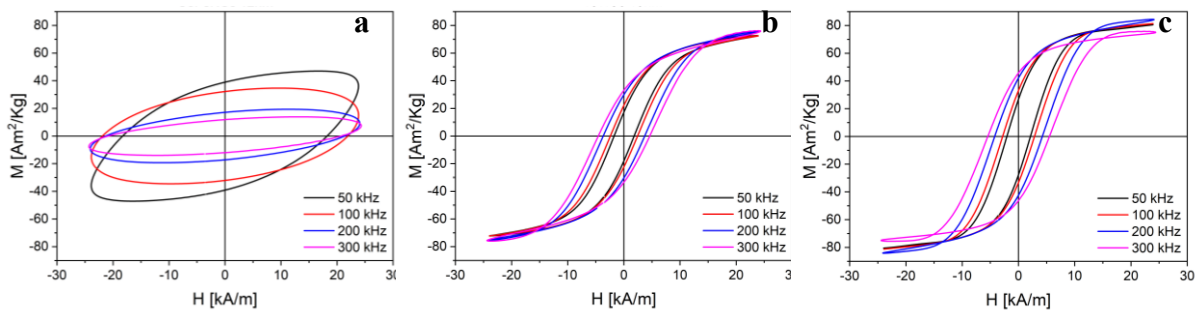


Figure 28 ACHLs of **a)** CoFeNCs 12nm **b)** IONCs 15nm and **c)** ZnFeNCs 13nm recorded at fixed field 24kA/m and different frequency: 50 kHz, 100 kHz, 200 kHz and 300 kHz.

The ACHLs for CoFeNCs seem to close with the increase in frequency and their particular elliptical shape revealed intrinsic difficulties for these NCs to follow the AMF. Contrarily, the ACHLs recorded for the IONCs and ZnFeNCs, were opening with the increase of the frequency applied. These results are important to understand the expected SAR performances to different AMF parameters and to find out the best heating performance expected for each type of NCs. In particular, with a sample in water, CoFeNCs would respond better applying low frequency and high field intensity and vice versa for ZnFeNCs.

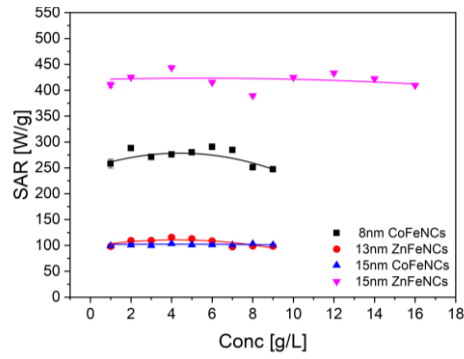


Figure 29 SAR concentration dependence (from 1 g/L to 9 g/L, till 16 g/L for 15 nm ZnFeNCs) at 100 kHz and 24 kA/m of different ferrite nanocubes. The error bars are not visible, being the standard deviation less than 1% of the measured value.

The SAR dependence on the NCs concentration was also studied for the different ferrites. For the concentration range observed, from 1 g/L to 9 g/L (till 16 g/L for 15 nm ZnFeNCs), the samples did not show any significant changes in their SAR values (Figure 29).

1.2.9 SAR and AC magnetic measurements of the ferrite nanocubes in viscous media

To better predict the response of the NCs in biological complex medium, the magnetic behavior of the NCs under viscous conditions was studied. For that purpose the NCs were dispersed in aqueous solutions with increases percentages of glycerol (0 % - 15 % - 36 % - 60 % - 80 %), using a constant concentration of materials (2 g/L).

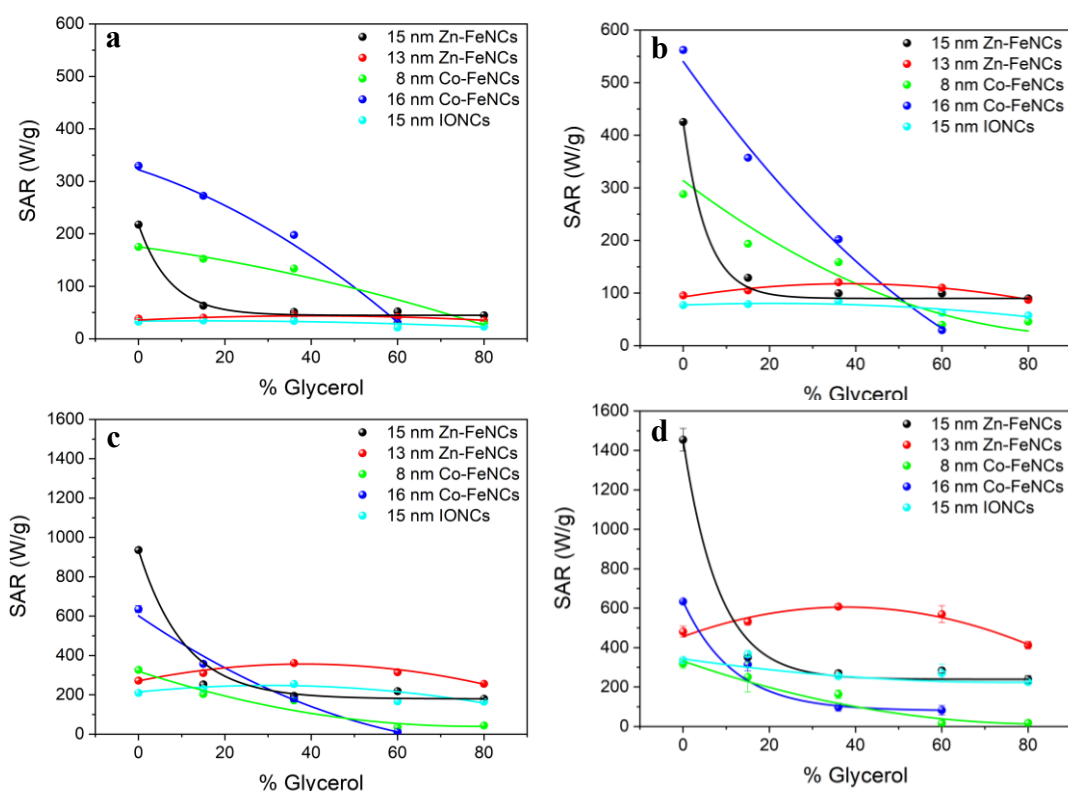


Figure 30 SAR media viscosity dependence measurements of IONCs, CoFeNCs and ZnFeNCs under AMF (24kA/m) at a) 50kHz, b) 100kHz, c) 200kHz and d) 300kHz. The percentages of Glycerol are 0-15-36-60-80% in a water solution at 2g/L of nanocubes. Lines are a guide to the eye. The error bars are not visible, being the standard deviation less than 2% of the measured value in most of the shown data.

The response of the NCs varies with size and composition (Figure 30). CoFeNCs at 16 nm in size are the most sensitive to the increase of viscosity, showing a drastic decrease in their heat ability as it was showed previously by *Cabrera at al.*²⁷ The 8 nm CoFeNCs were less affected by the viscosity changes. The SAR values of the IONCs and the 13 nm ZnFeNCs were almost not perturbed by the presence of glycerol, remaining constant, as shown in Figure 30. Moreover, the 15 nm ZnFeNCs showed an intermediate behavior between the smaller ZnFeNCs and the CoFeNCs. In this case, the SAR drops using 0-15 % of glycerol and remains

constant for the higher viscosities. The behavior revealed from the particles might be ascribed to a prominent Brownian relaxation heating process in the case of the CoFeNCs and a prevalent Néel relaxation process for the IONCs. For what concerns the ZnFeNCs heating process is not so clear. It might be in the middle between the two relaxation processes depending on the NPs size.

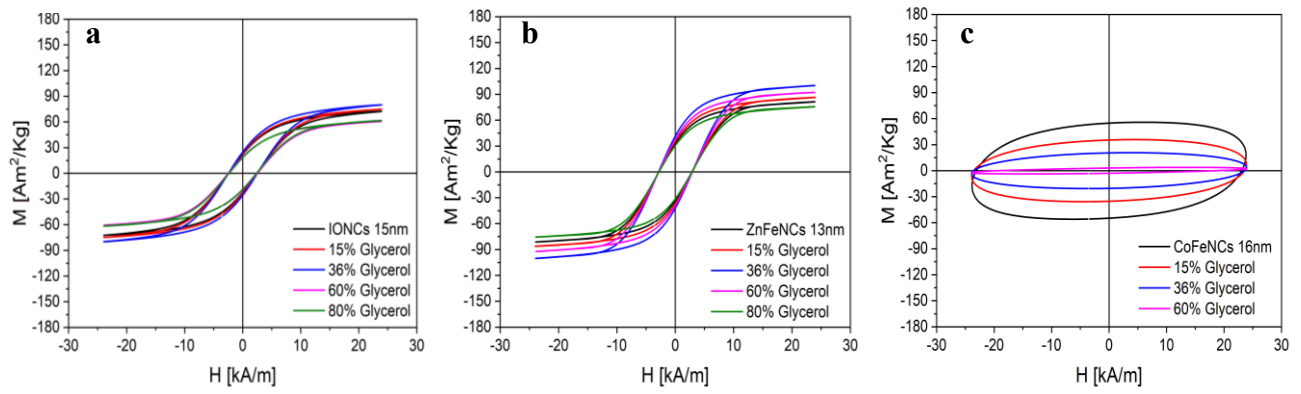


Figure 31 Magnetic AC hysteresis loops viscosity dependence measurements of **a)** ZnFeNCs, **b)** IONCs and **c)** CoFeNCs under AMF(100kHz and 24kA/m). The percentages of Glycerol are 0-15-36-60-80% in a water solution at 2g/L of nanocubes.

The dependence on the media viscosity is clear also from the ACHLs graph (Figure 31). Interestingly, the ACHLs for CoFeNCs close with the increase of viscosity in a similar manner as they show for the increase of frequency, confirming the predominance of the Brownian relaxation heating process.

1.2.10 Automatized synthesis of MNBs: large scale synthesis

One of the main issues associated to the synthesis of MNBs is the difficulty to scale up the process, because it works only for small sample volumes. For that reason, a procedure developed in our group for the production of MNBs³⁷ was adapted to be used by a robotic liquid handler (Nimbus) in an attempt to scale up the synthetic procedure. The modifications from the original protocol were applied due to the implementation of the automatic device. In particular, the NCs were dissolved in THF instead of CHCl₃ and water was used as anti-solvent. The shaking velocity was decreased from 1200 rpm to 450 rpm. Furthermore, the velocity of the anti-solvent dripping was tuned considering the robot requirements.

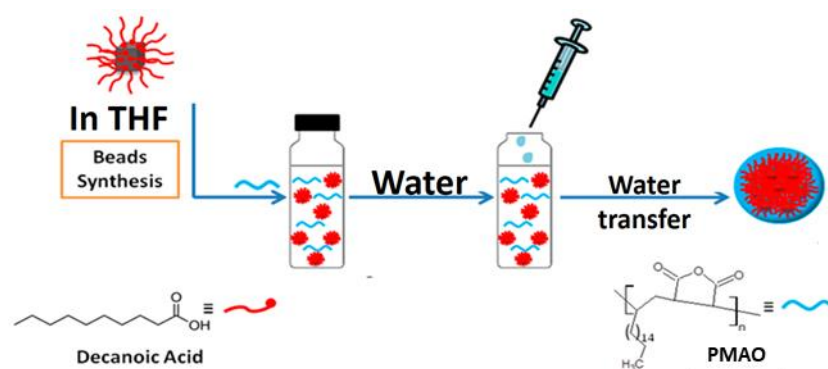


Figure 32 Scheme of MNBs robotic synthesis. The NCs dissolved in THF were mixed with a stock solution of PMAO in the same solvent. Soon after the water (working as anti-solvent) was added to the solution drop by drop inducing the MNBs formation. Modified and reproduced with permission from reference 37

This procedure, carried out by the liquid handler, allows the production of nanobeads starting from different ferrite NCs by adjusting the addition rate of the water, which was set to values between 2.5 and 5 mL/min depending on the type of ferrite NCs. These results confirm the advantage of using the robotic handler for preparing high amounts of MNBs in few minutes. Generally, such amount of materials would take days to be prepared, requiring the operator to repeat manually hundred times the same procedure. Moreover, this protocol allowed to produce MNBs composed by different ferrite NCs. In Figure 33, the TEM images of different ferrite MNBs as synthesized by Nimbus are shown indicating the good quality of the sample prepared. The analysis at DLS (Figure 34) showed results comparable in PDI and hydrodynamic size with the one obtained for the standard procedure.³⁷

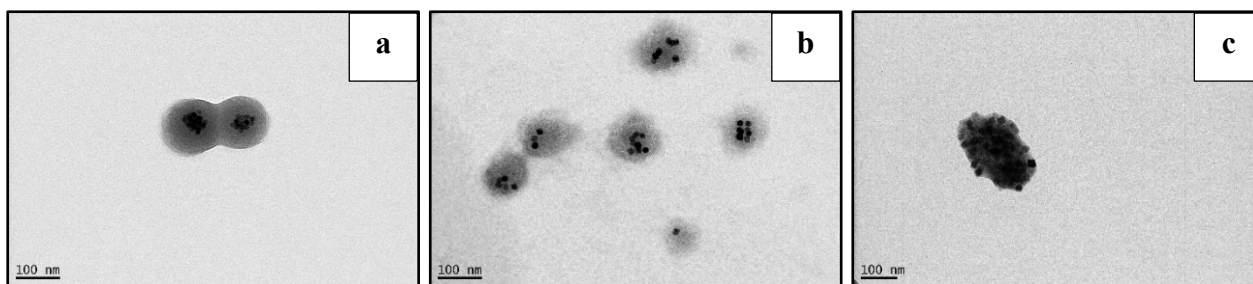
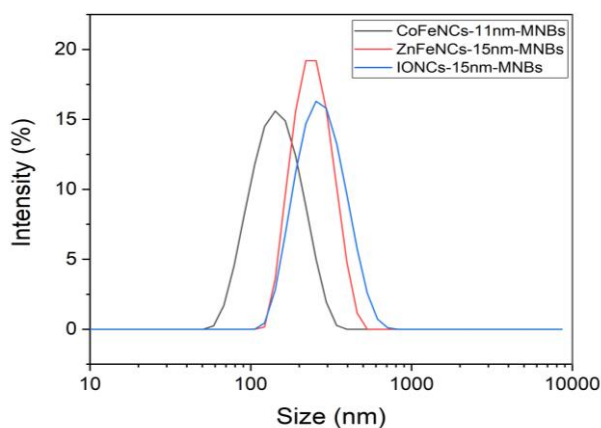


Figure 33 MNBs composed by different ferrite NCs synthesized by automatized procedure (Nimbus): **a**) IONCs, **b**) CoFeNCs and **c**) ZnFeNCs.



| | <i>PDI</i> | <i>dh by intensity (nm)</i> | <i>dh by number (nm)</i> | <i>dh by volume (nm)</i> |
|---------------------------|------------|-----------------------------|--------------------------|--------------------------|
| <i>IONCs-MNBs 15nm</i> | 0.172 | 286±2 | 214±2 | 299±2 |
| <i>Co-FeNCs-MNBs 11nm</i> | 0.334 | 126±3 | 68±2 | 97±4 |
| <i>Zn-FeNCs-MNBs 15nm</i> | 0.250 | 249±2 | 205±2 | 254±2 |

Figure 34 DLS intensity size measurements of magnetic nanobeads composed by IONCs, CoFeNCs, ZnFeNCs and tables of DLS values relative to the same samples (each value is the result of three measurements repetition).

1.2.11 SAR and AC magnetic measurements of MNBs

The magnetic behaviors and the SAR performances of the MNBs produced by the automatic procedure were investigated. The field applied in all the experiments was 24 kA/m. The SAR values for iron oxide MNBs and zinc ferrite MNBs, in result to the ACHLs area reduction, showed a one-half decrease with respect to the measurements done in water and in glycerol. The shapes of the ACHLs did not change (Figure 35).

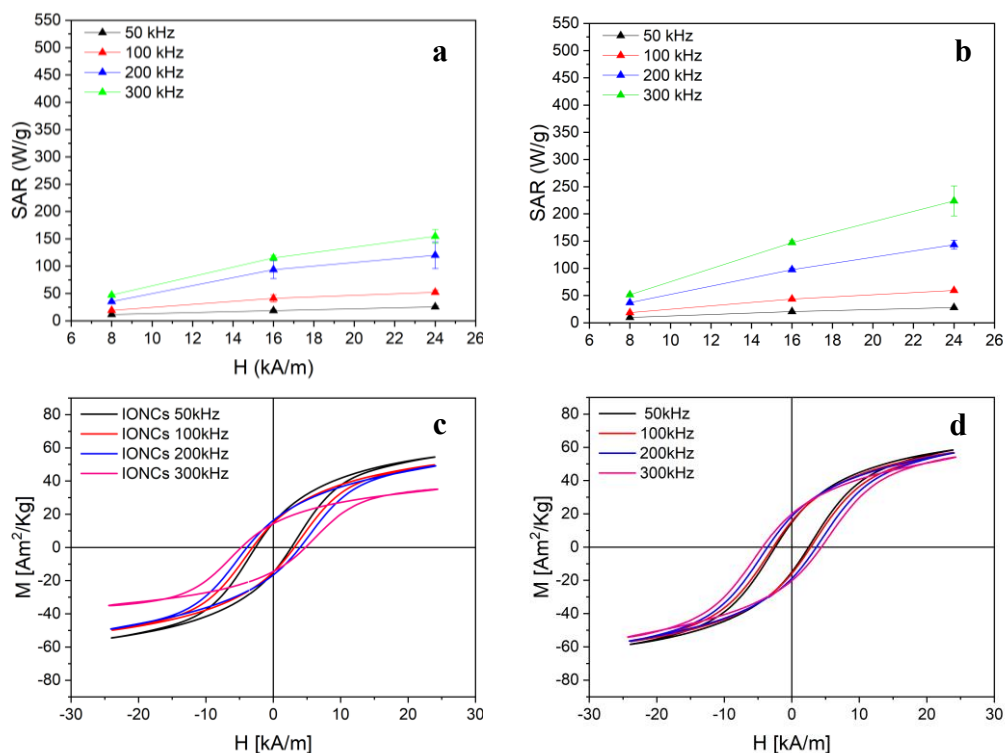


Figure 35 SAR characterization and AC hysteresis loops of **a, c)** IONCs-MNBs and **b, d)** ZnFeNCs-MNBs. The **c, d)** HLs were recorded at 24kA/m.

On the contrary, the recorded values for the cobalt ferrite MNBs (two sizes 11 and 13 nm) were confirming what was seen in the experiments with viscous media and were even worse. The heating ability disappeared and the ACHLs collapse on them self (Figure 36).

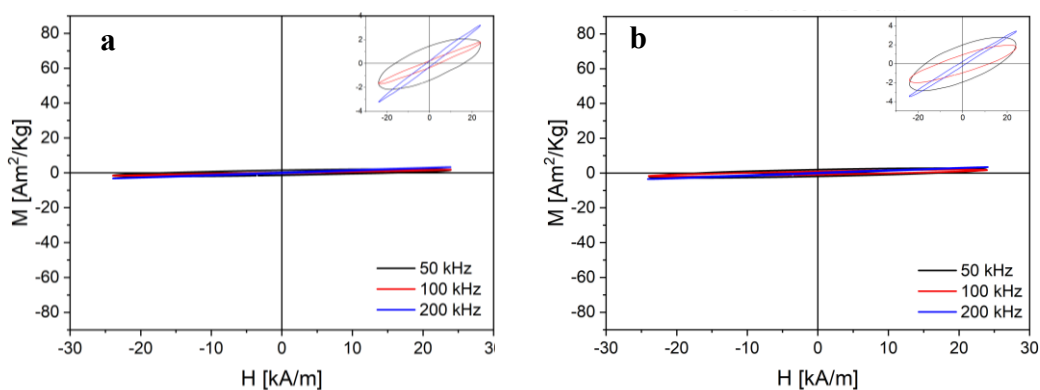


Figure 36 ACHLs of **a)** CoFeNCs 11±1nm MNBs and **b)** CoFeNCs 13±2nm MNBs, recorded at 24kA/m.

1.2.12 Relaxivity characterization

In order to achieve high efficiency of a MRI contrast agent it is crucial to lower the longitudinal (T1) or transverse (T2) relaxation times of the water proton spins in tissues at the lowest contrast agent concentration.³⁴ The relaxivity defined as the slope of the relaxation time rate (either 1/T1 or 1/T2) is a direct measurement of this efficiency. Ferrite nanoparticles, in particular IONPs, are well known MRI contrast agents in which the T2 relaxation times are predominant (shorter than T1).^{37,63} Increasing r2/r1 ratio plays a key role in improving the darker signals of T2-weighted images in MRI (when the r2/r1 is greater than 2, the nanoparticles are better for T2 contrast agent for MRI).¹⁰⁷ The relaxivities of polymer coated (PMAO) nanocubes samples of various stoichiometries and comparable sizes were measured at 1.5 T and 0.5 T (Figure 37). The related experimental measured longitudinal and transvers relaxation rates are visible in Figure A7 and A8 in appendix.

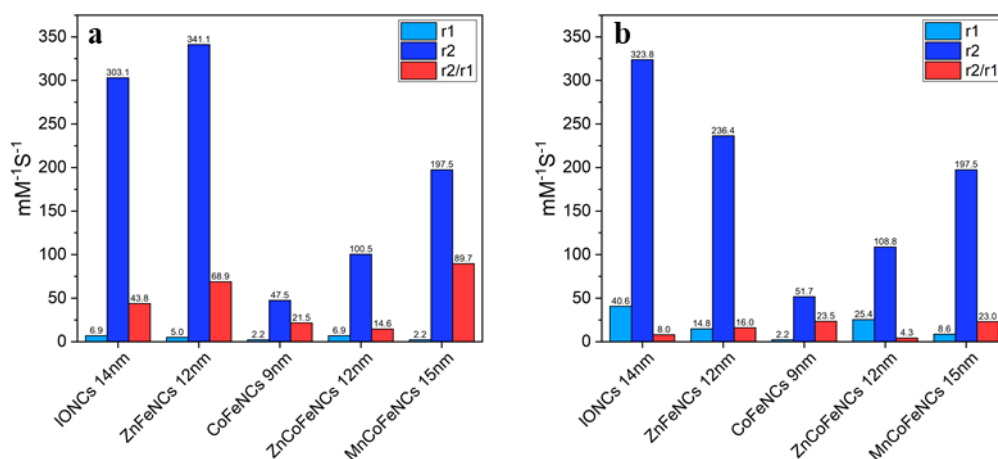


Figure 37 Relaxivity characterization for application in MRI, values recorded at 1.5T **a**) and 0.5T **b**) for the different ferrite samples.

Among all the measured samples, the ZnFeNCs show the highest r2 value under 1.5 T field; but their r2 decreases from 341 mM⁻¹s⁻¹ to 236 mM⁻¹s⁻¹ when 0.5 T field is applied. This is the only sample that showed a significant difference between the two field intensities. The MnCoNCs revealed to have the highest value of the ratio r2/r1 (89.7 mM⁻¹s⁻¹), followed by the ZnFeNCs (68.9 mM⁻¹s⁻¹).

1.2.13 Relaxometry measurements for MPI imaging application

Being MPI an emerging and powerful imaging technique the samples were evaluated for this application. The NCs were exposed to a sinusoidal magnetic field (frequency 16.8 kHz, amplitude 20 mT), which mimics the field free region (FFR) movement across the sample during an MPI experiment. The time dependent magnetization is inductively detected by a receiver coil and gridded to the known instantaneous magnetic field value to generate the PSF.⁴² The samples were prepared to have same volumes with the same coatings. In particular, two sets of samples were measured: the first with the NPs dispersed in chloroform and the second with the water transferred NPs capped in PMOA, using 500 μ L of sample at 1 g/L. Image resolution in MPI is determined by the full-width at half-maximum (FWHM) of the PSF. In order to generate a signal, MPI tracers must undergo a magnetization reversal, which requires overcoming viscous, thermal, and inertial torques by using a combination of Brownian and Néel relaxations.⁴² The ideal PSF, generated by tracers with minimal relaxation, is symmetric, with high signal-to-noise ratio (SNR) and small FWHM, corresponding to high image resolution. A first screen of samples were analyzed directly in chloroform. Only the best samples were then transferred in water for further characterization. All the data were compared with a commercial MRI contrast agent (Resovist, Bayer-Schering Pharma), used as reference (1mg).

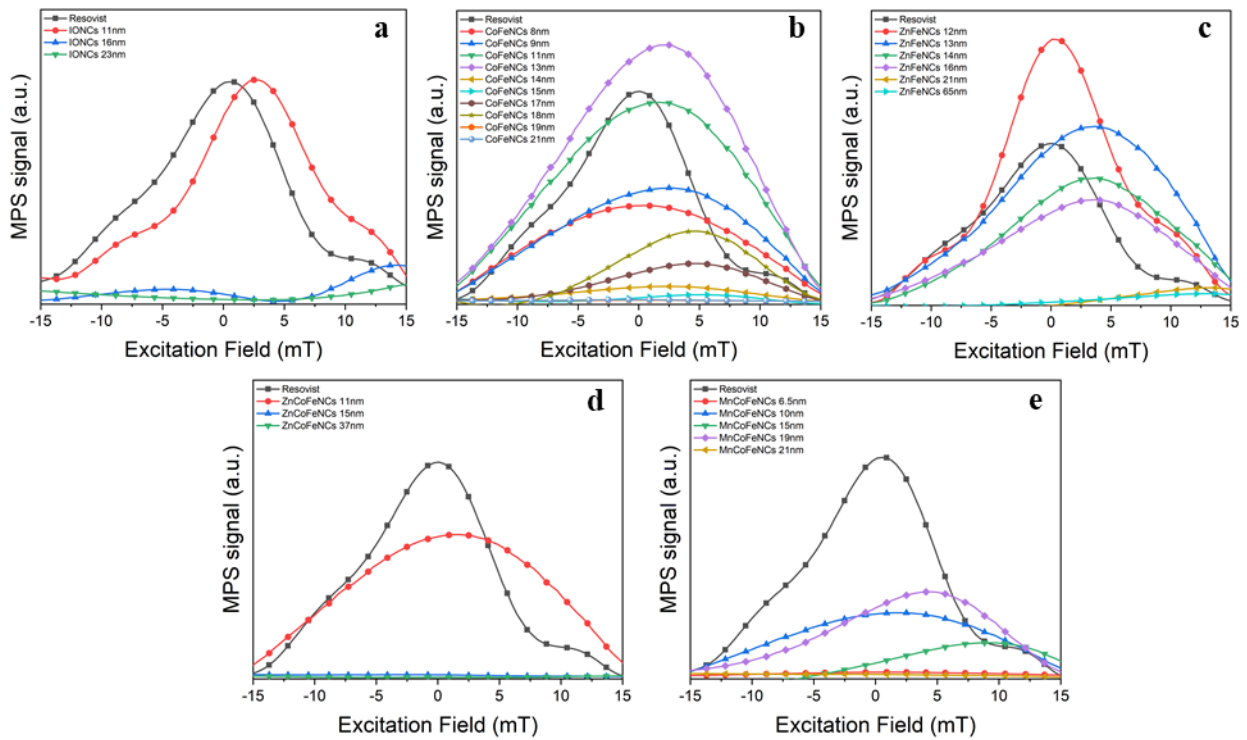


Figure 38 Point spread functions (PSF) of the ferrite nanoparticles, different sizes in chloroform; **a)** IONCs, **b)** CoFeNCs, **c)** ZnFeNCs, **d)** ZnCoFeNCs and **e)** MnCoFeNCs.

In Figure 38 are shown the graphs relative to the PSF of the different ferrite nanocubes analyzed in chloroform. The best results were achieved by the ZnFeNCs samples followed by the CoFeNCs and the IONCs. Among the different ferrite compositions, it is interesting to observe that the NCs with the higher PSF are the ones in the size range between 11 nm and 14 nm as compared to resovist. The best performant samples in chloroform were chosen to evaluate their behavior for MPI in water.

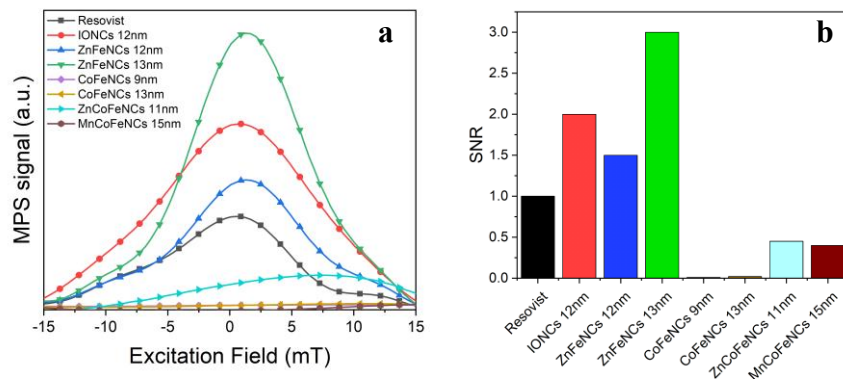


Figure 39 Point spread function **a**) and Signal to Noise Ratio (SNR) **b**) of the chosen NCs samples from the evaluation in chloroform.

The results obtained after the water transfer (Figure 39a reflect the SAR results for the characterization in viscous media. The signal in MPI is sensitive to the environment in which the NPs are, so the polymer shell plays an important role in the signal generation. Moreover, the Brownian relaxation is slower than the field switching cycle and, therefore, it has minimal influence on magnetic particles spectrometry (MPS) signals and so Néel relaxation is the dominant mechanism determining MPI response for small NPs (size $< \sim 15$ nm).¹⁰⁸ Indeed, the samples containing cobalt, which have been proven to have predominant Brownian relaxation process, showed a strong decrease in the MPS signal. On the other hand, the MPS signals for ZnFeNCs and IONCs capped with PMAO are even higher than in chloroform, revealing their dependence to the Néel relaxation process. These differences between the NCs performances are also visible from the SNR graph (Figure 39b), in which ZnFeNCs and IONCs had respectively 3 and 2 fold the SNR value of the Resovist, while the CoFeNCs do not show any signal. Noticeably, the mixed ferrite NCs show a SNR that is one-half of the reference. This might be explained by the insertion of the Zn and Mn ions besides the Co that reduces the dependence from the Brownian relaxation.

1.2.14 Cytotoxicity of the nanocubes

In order to exploit the ferrite nanocubes for biological applications, their cytotoxicity was evaluated *in-vitro* on mouse brain endothelial (bEnd3) and mouse glioblastoma (GL261) cells. The tests were done for CoFeNCs and the ZnFeNCs, the latter was the material that showed the most promising magnetic performances as discussed above. Both the types of ferrite nanocubes were functionalized with an additional PEG shell to ensure good stability in biological media. The results in Figure 40 show at 24 hours a negligible percentage of cell death for both kinds of nanocubes and cell types studied. However, as expected, the continuous exposure to CoFeNCs, especially at higher concentration, promotes cytotoxicity over time.¹⁰⁹ Their toxicity was less prominent on the glioblastoma cells. This may be explained as this carcinogenic cell line is more resistant to the Co induced toxicity with respect to the normal ones.¹¹⁰ Contrariwise, ZnFeNCs did not show any signs of cell toxicity even at the highest concentration of NCs administered.

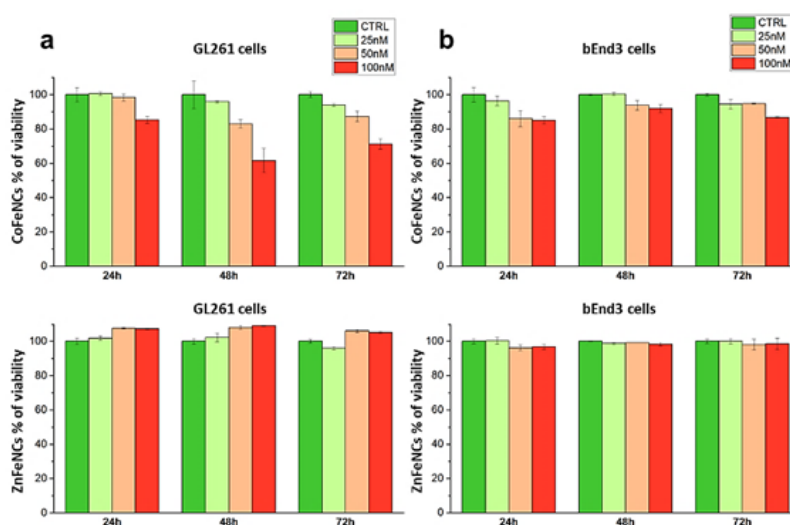
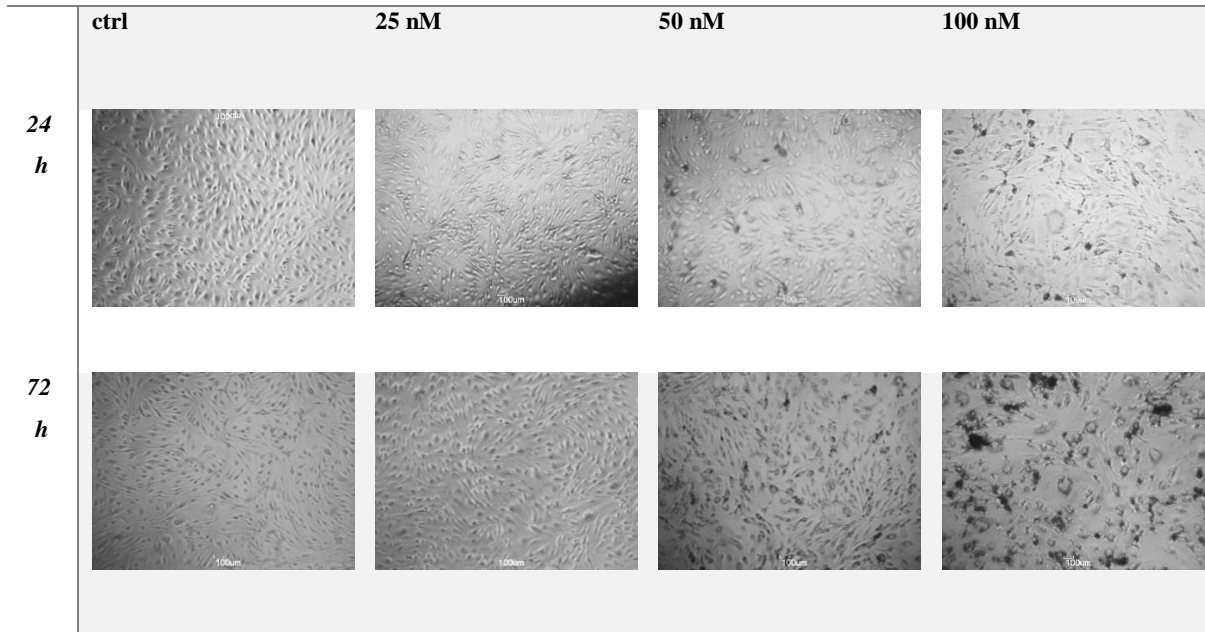


Figure 40 Cytotoxicity of ZnFeNCs(12±1nm) and CoFeNCs(13±2nm) **a)** on GL261 and **b)** bEnd3 cells at 24,48 and 72 hours; using three different concentrations of NCs, 25,50 and 100nM (corresponding to 0.1, 0.2, 0.4 g_{F_o}/L and 0.02, 0.04, 0.08 g_{C_o}/L for the CoFeNCs; 0.14, 0.28, 0.56 g_{F_o}/L and 0.01, 0.02, 0.04 g_{Zn}/L for the ZnFeNCs).

These results are supported by the bEnd.3 cells images acquired with the optical microscope. The picture referred to the highest concentration of CoFeNCs, after 72 h of incubation, shows some agglomerates of NCs sticking on the cells layer. The cells in that condition look disperse, confirming that were suffering not only for the intrinsic toxicity of the CoFeNCs, but also because of the NCs aggregation. In the other hand, the image about the ZnFeNCs at the same incubation conditions looks the same as 24h. In addition, in this case there was a little

aggregation of the NCs but less accentuated than the CoFeNCs and it seems not generate a toxic effect on cells.

CoFeNCs



ZnFeNCs

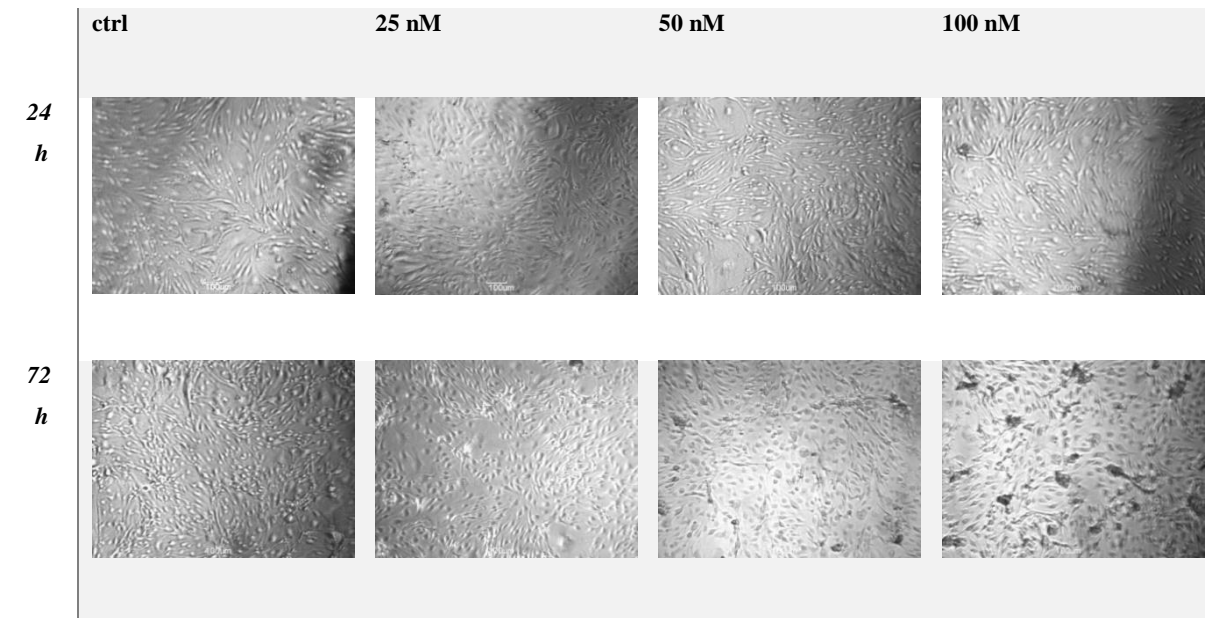


Figure 41 Images at optical microscope(20X magnification) of bEnd.3 cells incubated with ZnFeNCs (12nm) and CoFeNCs (13nm) bEnd3 cells at 24 and 72 hours; using three different concentrations of NCs, 25,50 and 100nM (corresponding to 0.1, 0.2, 0.4 g_{Fe}/L and 0.02, 0.04, 0.08 g_{Co}/L for the CoFeNCs; 0.14, 0.28, 0.56 g_{Fe}/L and 0.01, 0.02, 0.04 g_{Zn}/L for the ZnFeNCs)

1.3 Conclusions and outlook

In this chapter, an optimization for the synthesis of CoFeNCs with improved reproducibility and quality is presented. In particular size and shape distribution were improved, obtaining CoFeNCs in the size range between 8 and 15 nm, which was never reported before. A modified procedure for the polymer coating of the MNCs has been introduced that has allowed increasing the yield and the quality of the NPs transferred in water. These modifications have helped to simplify the protocol allowing to obtain significant amount of NPs in shorter times. The heating ability of CoFeNCs was investigated measuring the SAR performances. Interestingly, the results showed that smaller NCs (8-11 nm) performs better than bigger ones (14-15 nm). Moreover, the SAR values of these NCs were found to be sensitive to the field raise and almost invariant with the frequency. These results render the CoFeNCs interesting for applications in which low frequency AMF is required. Then, convenient sets of one-pot synthesis procedures to obtain ZnFeNCs and mixed ferrite nanocubes (ZnCoFeNCs and MnCoFeNCs) are reported. In addition, the possibility to tune the size and composition of the mixed ferrite NCs by controlling the amount of the metal precursors is discussed. The wide range of nanocubes prepared were subjected to an extensive characterization in order to compare their heating performances for hyperthermia treatment and their potential to be used as contrast agents for MRI and MPI application. The results obtained revealed interesting qualities for ZnFeNCs, especially in the size range under 15 nm, showing the highest performance for all the applications in exam (MHT, MRI and MPI). In particular, the predominance of the Néel relaxation process was demonstrated for ZnFeNCs. While the CoFeNCs showed a predominant Brownian relaxation process losing the ability to heat up once poured in viscous media, capped with a polymeric shell or embedded in the matrigel matrix. Adding another ion with the cobalt (like zinc or manganese), obtaining mixed ferrite NCs could mitigate these losses. However, their performances remain inferior to the one achieved with ZnFeNCs. To complete the study, the biocompatibility of ZnFeNCs was shown *in-vitro* on healthy and carcinogenic murine cells, confirming the suitability of such materials to be applied in the intended biomedical applications (HT, MRI and MPI). Further development of this work will exploit the properties of mixed ferrite nanocubes in order to study how the change of composition at a given size can act on the NCs performances.

1.4 Experimental section

Synthesis of iron oxide nanocubes

Fe₃O₄ nanocubes (IONCs) were synthesized by thermal decomposition following an established procedure with suitable modifications. The protocol relies on the synthesis of particles of 15 nm in size. In a 100 mL three-neck flask connected to a standard Schlenk line, 1 mmole (353 mg) of Fe(acac)₃ and 5.5 mmoles (950 mg) of decanoic acid were dissolved in a mixture of 10 mL squalane and 15 mL benzyl ether. The resulting solution was degassed at 65 °C for 2 h reaching 16-25 μBar vacuum after 2 h. After switching to N₂ flow, the temperature of the mixture was increased to 200 °C at a rate of 5 °C/min and kept at 200 °C for 1.5 h. Then, the reaction temperature was increased to 305 °C at a rate of 7.5 °C/min keeping the mixture refluxing for 1 h. The flask was then cooled down to room temperature (RT) under inert atmosphere. The black colloidal solution was washed 2 times with excess amount of acetone (45 mL) and centrifuged at 4500 rpm for 20 min to collect the particle as black precipitate. The final particles were dispersed in chloroform (8 mL) for further experiments.

Synthesis of cobalt ferrite nanocubes

Co_xFe_{3-x}O₄ nanocubes (CoFeNCs) were synthesized by thermal decomposition following an established procedure, with suitable modifications. The protocol relies on the synthesis of particles of 17 nm in size with 0.65 Co stoichiometry. In a 100 mL three-neck flask connected to a standard Schlenk line, 0.46 mmoles (115 mg) of Co(acac)₂, 1 mmole (353 mg) of Fe(acac)₃ and 6 mmoles (1033 mg) of decanoic acid were dissolved in a mixture of 12 mL squalane and 13 mL benzyl ether. The resulting deep red solution was degassed at 65 °C for 2 h reaching 16-20 μBar vacuum after 2 h. After switching to N₂ flow, the temperature of the mixture was increased to 200 °C at a rate of 5 °C/min and kept at 200 °C for 1.5 h. After, the reaction temperature was increased to 305 °C at a rate of 7.5 °C/min keeping the mixture refluxing for 1 h. The flask was then cooled down to room temperature under inert atmosphere. The black colloidal solution was washed 2 times with excess amount of acetone (45 mL) and centrifuged at 4500 rpm for 20 min to collect the particle as black precipitate. The final particles were dispersed in chloroform (8 mL) for further experiments.

Synthesis of zinc ferrite nanocubes

Zinc ferrite nanocubes ($Zn_xFe_{3-x}O_4$ NCs) were synthesized by thermal decomposition. The protocol rely on the synthesis of particles of 15 nm in size and with 0.2 Zn stoichiometry. In a 100 mL three-neck flask connected to a standard Schlenk line, 0.5 mmoles (131 mg) of $Zn(acac)_2$, 1 mmole (353 mg) of $Fe(acac)_3$ and 7 mmoles (1033 mg) of decanoic acid were dissolved in a mixture of 12 mL squalane and 13 mL benzyl ether. The solution was degassed at 65 °C for 1.5 h reaching 16-20 μ Bar vacuum after 1.5 h. After switching to N₂ flow, the temperature of the mixture was increased to 200 °C at a rate of 5 °C/min and was then kept at 200 °C for 2 h. The reaction temperature was increased to 300 °C at a rate of 7.5 °C/min keeping the mixture refluxing for 1 h. The flask was than cooled down to RT under inert atmosphere. The black colloidal solution was washed 2 times with excess amount of acetone (45 mL) and centrifuged at 4500 rpm for 20 min to collect the particles as black precipitate. The final particles were dispersed in chloroform (8 mL) for further experiments.

Syntheses of zinc-cobalt ferrite and manganese-cobalt ferrite nanocubes

Zinc-cobalt and manganese-cobalt ferrite nanocubes ($Zn_xCo_yFe_{3-(x+y)}O_4$ NCs or $Mn_xCo_yFe_{3-(x+y)}O_4$ NCs) were synthesized by thermal decomposition, following similar protocols. zinc-cobalt-ferrite NCs of 15 nm in size, were synthesized using 0.1 Zn and 0.2 Co stoichiometry. In a 100 mL three-neck flask connected to a standard Schlenk line, 0.25 mmoles (63 mg) of $Zn(acac)_2$, 0.25 mmoles (62 mg) of $Co(acac)_2$, 1 mmole (353 mg) of $Fe(acac)_3$ and 6 mmoles (1033 mg) of decanoic acid were dissolved in a mixture of 12 mL squalane and 13 mL benzyl ether. The solution was degassed at 65 °C for 1.5 h reaching 16-20 μ Bar vacuum after 1.5 h. After switching to N₂ flow, the temperature of the mixture was increased to 200 °C at a rate of 5 °C/min kept at 200 °C for 2 h. The reaction temperature was increased to 300 °C at a rate of 7.5 °C/min keeping the mixture refluxing for 1 h. The flask was than cooled down to RT under inert atmosphere. The black colloidal solution was washed 2 times with excess amount of acetone (45 mL) and centrifuged at 4500 rpm for 20 min to collect the particles as black precipitate. The final particles were dispersed in chloroform (8 mL) for further experiments. For the synthesis of the manganese-cobalt ferrite NCs the same protocol was followed replacing $Zn(acac)_2$ with the $Mn(acac)_2$ hydrate. The contribution of the metal precursors on the size of those NCs is discussed below.

Phase transfer of the NCs in water with poly(maleic anhydride-alt-1-octadecene).

The synthesized, hydrophobic NCs dispersed in chloroform were transferred to water, using poly(maleic anhydride-alt-1-octadecene) (PMAO), following a protocol developed by our group with suitable modifications.^{100,111} NCs of 15 nm in size at a concentration of about 400 nM (were diluted with an excess of chloroform (70 mL) and sonicated for 5 minutes. A certain amount of PMAO polymer solution in chloroform (137 mM, concentration referred to the monomer units) was added, respecting a ratio of 500 molecules of monomer unit per nm² of NC surface. The solvent was evaporated at the Rotavapor (140 rpm, 50 °C) following three steps of evaporation under reduced pressure: 800 mBar for 30 minutes, 700 mBar for 30 minutes and finally 600 mBar until complete solvent evaporation was achieved. The dried sample was then soaked in 20 mL of borate buffer and sonicated at 65 °C for 1 h until complete solubilization was verified. The water soluble NCs were concentrated by an ultrafiltration system. The sample volume was reduced to nearly 3 mL under continuous shaking at 150 rpm for 15 min at RT. Subsequently, the sample was loaded on top of a sucrose gradient (2 mL of 20 %, 3 mL of 40 % and 3 mL of 60 % in an ultra-centrifugal tube, from top to bottom) and centrifuged at 20,000 rpm for 45 min. The excess of polymer (visible under UV lamp) found at the top of the sucrose gradient at 20 % was removed, by collecting it with a syringe. Instead, the nanocubes, usually found in the 40 % to 60 % fraction of the sucrose gradient were collected and further washed with pure water (MilliQ) three times to remove the excess of sucrose and finally concentrated to a final volume of about 4 mL in water.

Poly(ethylene glycol) functionalization

The functionalization of the polymeric shell of nanocubes with poly(ethylene glycol) (PEG) was carried out following a procedure developed in our group, with minor modifications.¹¹² A solution of CoFeNCs of 0.1 μM was mixed with the same volume of 0.125 M 1-ethyl-3-(3-dimethylaminopropyl)carbodiimide hydrochloride (EDC) and a diamine-PEG (NH₂-PEG-NH₂) 0.1 mM solution in pure water. The amount of PEG was kept as 1000 fold excess compared to Co-FeNCs molar concentration. The mixture was vigorously shaken for one minute and left under gently shaking at 150 rpm for 2 h RT. Finally, the solution was diluted 3 times to quench the reaction and washed in pure water using centrifugal filters. The final sample was collected in few microliters of water.

Robotic procedure for Magnetic Nano Beads synthesis

The synthesis of magnetic nanobeads (MNBs) is based on a reported work with substantial modifications to adapt it for the automatic liquid handler (Nimbus - Hamilton).^{37,113} Briefly, to prepare MNBs of IONCs, 7 μL of IONCs (0.12 μM nanoparticles concentration, $d = 15 \text{ nm}$) in tetrahydrofuran (THF) were added in an 8 mL glass vial. Soon after, 180 μL of THF and 20 μL of a stock solution of PMAO in CHCl_3 (50 mM, this concentration refers to the polymer monomer units) were added. The mixture was shaken in the robot orbital shaker at 450 rpm for 60 s at 20 °C. Subsequently, 800 μL of water was added at a flow rate of 5 mL min^{-1} . To wash the MNBs and transfer them in water, the samples were manually collected by keeping them on top of an external magnet (0.3 T) for about 30 min. The supernatant was removed, and the MNBs were dissolved in 500 μL of water. To have enough materials for SAR measurements the above-reported procedure was repeated by the robot 5 times, to a total amount of 120 reactions (24 in each run).

Elemental analysis

Inductively coupled plasma optical emission spectroscopy (ICP-OES) analysis was performed on an iCAP 6000 spectrometer (ThermoScientific) to quantify the concentration of the elements of interest. Briefly, 25 μL samples were digested in 2.5 mL of aqua regia ($\text{HCl}:\text{HNO}_3$ ratio is 3:1 (v/v)) overnight and diluted with 25 mL of milliQ water prior to the measurement.

Transmission electron microscopy

Transmission electron microscopy (TEM) was carried out on a JEOL JEM-1011 with an acceleration voltage of 100 kV. The sample preparation was conducted by drop-casting a droplet of the sample solution onto a 400 mesh ultra-thin carbon-coated copper grid with subsequent removal of the solvent by evaporation at RT. Images were captured and recorded with a 11 Mp fiber optical charge-coupled device (CCD) camera (Gatan Orius SC-1000).

Matrigel samples with CoFeNCs were chemically fixed overnight at 4°C in a fixative solution (4% Paraformaldehyde + 2% Glutaraldehyde) prepared in Na-Cacodylate buffer 0.1M, post-fixed for 2 hours in 1% OsO_4 solution in Na-Cacodylate buffer 0.1M and finally stained overnight in a 1% Uranyl acetate aqueous solution at 4°C. After several washes in water, samples were completely dehydrated with a scale of Ethanol, propylene-oxide and then infiltrated with epoxy Spurr (SPI-Chem) resin. Once the resin has hardened for 48h in oven at

65°C, 70 nm thick sections were cut with a Leica EMU C6 ultra-microtome. Transmission electron microscopy (TEM) images were then collected.

X-Ray Diffraction analysis

XRD patterns were recorded on a Malvern PANalytical Empyrean diffractometer machine. The X-ray source is operated at 40 kV and 150 mA. The diffractometer was equipped with a Cu source and a Göbel mirror to obtain a parallel beam as well as to suppress Cu K β radiation (1.392 Å). The 2-theta/omega scan geometry was used to acquire the data. The samples were prepared by drop casting concentrated NCs solutions onto a zero background silicon substrate. The PDXL software of Rigaku was used for phase identification.

Dynamic Light Scattering and gel electrophoresis

The hydrodynamic size was estimated by using dynamic light scattering (DLS) from Malvern Instruments Zetasizer-nano. The scattered intensity was collected at 173° back scattered geometry with 632 nm laser source. For each sample 3 measurements were taken with 10 acquisitions each. Gel electrophoresis was used to observe the NCs migration in a solid agarose matrix after the water transfer procedure to confirm the absence of free polymer in solution. The free polymer migrates faster than the NCs and can be detected under a UV light. The electrophoresis was run on 1% agarose gel in tris-borate-EDTA(TBE) buffer applying a voltage of 100 V or 45 minutes.

Magnetic characterization

Magnetic measurements were performed on a MPMS superconducting quantum interference device (SQUID) from Quantum Design Inc. Hysteresis curves were recorded within the magnetic field of ± 70 kOe at 5 K and 298 K.

Ac magnetic measurements

The inductive magnetic characterization was carried out with a custom-made device for AC magnetic measurements (IMDEA, Madrid). Hysteresis loops were recorded at different fields (8-16-24 kA/m) and frequency (50-100-200-300 kHz) combination. The experiments were performed with different ferrite NCs, testing their behavior varying the concentration from 2

to 9 gL⁻¹, the viscosity of the media (glycerol at 15 %-36 %-60 %-80 % in volume) and the aggregation state.

Calorimetric measurements of Specific absorption rate

A commercially available magnetic nano-heating device (DM100 Series, nanoscale Biomagnetics) was used to evaluate the SAR values under quasi-adiabatic conditions. The water soluble NCs were exposed to an alternating magnetic field (from 12 up to 32 kA/m) at 3 different frequencies: 105, 220 and 300 kHz. All measurements were performed using 300 µL of sample in water (at a concentration of 4 g/L) and the SAR values were normalized using the iron concentration determined by elemental analysis (g/L). SAR values were calculated according to the following equation:

$$\text{SAR} \left(\frac{\text{W}}{\text{g}} \right) = \frac{C}{m} \cdot \frac{dT}{dt}$$

Where C is the specific heat capacity of water (4185 J/kgK) and m is the concentration (g/L) of magnetic material in solution. To calculate the parameter dT/dt, temperature data points collected within the first 60 seconds were used to obtain the slope of the curve deriving from the linear fitting of these points. Each data point is given as the mean of at least three independent measurements.

Relaxivity Measurements

Water solutions of NCs containing different magnetic material concentrations ranging from 0.001 to 2 mM were prepared. The longitudinal (T1) and transverse (T2) relaxation times were measured at 40 °C using a Minispec spectrometer (Bruker, Germany) mq 20 (0.5 T) and mq 60 (1.5 T). The T1 relaxation profile was obtained using an inversion– recovery sequence, with 20 data points and 4 acquisitions for each measurement. T2 relaxation time was measured using a Carr–Purcell– Meiboom–Gill (CPMG) spin-echo pulse sequence with 200 data points with interecho time of 0.5 ms. The relaxivities r_i ($i = 1, 2$) were determined by the following equation:

$$\frac{1}{T_{i(obs)}} = \frac{1}{T_{i(H_2O)}} + r_i C_m \quad (i = 1, 2)$$

Where C_m is the concentration of magnetic ions. The values are reproducible within 5 % deviation.

MPI relaxometry

Magnetic particle relaxometry experiments were performed using Case Western Reserve University's custom x-space magnetic particle relaxometer. Background signals were acquired prior to testing each sample, and were subtracted from the averaged sample signals ($N = 10$ averages for both background and sample signals). The signal to noise ratio (SNR) was calculated as the point spread function (PSF) peak value divided by the noise level of the relaxometer, which was obtained by acquiring the signal from a sample of deionized water. The full width at half maximum (FWHM), which indicates image resolution, was evaluated by finding the width of the PSF (in mT) at one-half of the peak PSF value. To obtain an estimate of the image resolution, the FWHM is divided by the strength of the static gradient field. A measure of the PSF symmetry is obtained by finding the location of the peak PSF value; a symmetric PSF should have a peak shift of 0 mT.

Cell culture

Mouse cerebral endothelial cells (bEnd.3) were cultured in Dulbecco's Modified Eagle's Medium (DMEM) supplemented with 10 % fetal bovine serum (FBS), 1 % penicillin streptomycin (PS), 1 % pyruvate, 1% non-essential amino acids (100X)(MEM) and 1 % glutamine at 37 °C, 5 % CO₂ and 95 % humidity. Cells were split every 3-4 days, before reaching 100 % confluence. Mouse glioblastoma cells (GL261) were cultured in Dulbecco's Modified Eagle's Medium (DMEM) supplemented with 10 % fetal bovine serum (FBS), 1 % penicillin streptomycin (PS) and 1 % glutamine at 37 °C, 5 % CO₂ and 95 % humidity. Cells were split every 2-3 days, before reaching 100 % confluence.

NCs cytotoxicity studies

Viability of the bEnd3 and GL261 cells upon incubation with NCs were tested. Briefly, cells at a concentration of 10^5 cells per well were seeded in a 24 multiwell plate and allowed to adhere for 24 h. The day after, different NCs concentrations, diluted in fresh medium (100 nM, 50 nM and 25 nM), were added to the cells and incubated for additional 24 h, 48 h or 72 h at 37 °C. At each time point of interest, the cells were detached from the wells, washed several times in PBS and stained with a dead cell dye, the ethidium homodimer-1 (EthD-1) following

the manufacture's protocol and then analyzed by flow cytometry technique with a FACSariaIII (BD-bioscience) device. Loss of membrane integrity is an indicator of cell death in flow cytometric analysis. Cells that exclude a dead cell dye are considered viable, while cells with compromised membranes allow the dye inside the cell to stain an internal component, thus identifying the dead cells. Briefly, was prepared a staining solution diluting 2 μL of dye in 1 mL of phosphate buffer saline(PBS). The cells in each well were incubated with 500 μL of the staining solution for 20 min at RT. Soon after were washed and suspended in 200 μL of PBS and analyzed with FACS to count the dead cells.

1.5 References

1. Jeong, U., Teng, X., Wang, Y., Yang, H. & Xia, Y. Superparamagnetic Colloids: Controlled Synthesis and Niche Applications. *Adv. Mater.* **19**, 33–60 (2007).
2. Kolhatkar, A. *et al.* Tuning the Magnetic Properties of Nanoparticles. *Int. J. Mol. Sci.* **14**, 15977–16009 (2013).
3. Pereira, C. *et al.* Superparamagnetic MFe₂O₄ (M = Fe, Co, Mn) Nanoparticles: Tuning the Particle Size and Magnetic Properties through a Novel One-Step Coprecipitation Route. *Chem. Mater.* **24**, 1496–1504 (2012).
4. Zhang, Y., Kohler, N. & Zhang, M. Surface modification of superparamagnetic magnetite nanoparticles and their intracellular uptake. *Biomaterials* **23**, 1553–1561 (2002).
5. Ming Zhao, *, †, Moritz F. Kircher, †, Lee Josephson, and & Weissleder, R. Differential Conjugation of Tat Peptide to Superparamagnetic Nanoparticles and Its Effect on Cellular Uptake. (2002). doi:10.1021/BC0255236
6. Knobel, M. *et al.* Superparamagnetism and Other Magnetic Features in Granular Materials: A Review on Ideal and Real Systems. *J. Nanosci. Nanotechnol.* **8**, 2836–2857 (2008).
7. Jeong, U., Teng, X., Wang, Y., Yang, H. & Xia, Y. Superparamagnetic Colloids: Controlled Synthesis and Niche Applications. *Adv. Mater.* **19**, 33–60 (2007).
8. Krishnan, K. M. Biomedical Nanomagnetism: A Spin Through Possibilities in Imaging, Diagnostics, and Therapy. *IEEE Trans. Magn.* **46**, 2523–2558 (2010).
9. Craik, D. J. & McIntyre, D. A. Critical Size of Magnetic Particles with High Uniaxial Anisotropy. *Proc. R. Soc. A Math. Phys. Eng. Sci.* **302**, 99–112 (1967).
10. Kittel, C. Physical Theory of Ferromagnetic Domains. *Rev. Mod. Phys.* **21**, 541–583 (1949).
11. Salunkhe, A. B., Khot, V. M. & Pawar, S. H. Magnetic Hyperthermia with Magnetic Nanoparticles: A Status Review.
12. Obaidat, I. *et al.* Magnetic Properties of Magnetic Nanoparticles for Efficient Hyperthermia. *Nanomaterials* **5**, 63–89 (2015).
13. GILCHRIST, R. K. *et al.* Selective inductive heating of lymph nodes. *Ann. Surg.* **146**, 596–606 (1957).
14. Mahmoudi, K., Bouras, A., Bozec, D., Ivkov, R. & Hadjipanayis, C. Magnetic hyperthermia therapy for the treatment of glioblastoma: a review of the therapy's history, efficacy and application in humans. *Int. J. Hyperth.* **34**, 1316–1328 (2018).
15. Usov, N. A. Low frequency hysteresis loops of superparamagnetic nanoparticles with uniaxial anisotropy. *J. Appl.*

- Phys.* **107**, 123909 (2010).
16. Poperechny, I. S., Raikher, Y. L. & Stepanov, V. I. Dynamic magnetic hysteresis in single-domain particles with uniaxial anisotropy. *Phys. Rev. B* **82**, 174423 (2010).
 17. Dennis, C. L. & Ivkov, R. Physics of heat generation using magnetic nanoparticles for hyperthermia. *Int. J. Hyperth.* **29**, 715–729 (2013).
 18. Rosensweig, R. E. Heating magnetic fluid with alternating magnetic field. *J. Magn. Magn. Mater.* **252**, 370–374 (2002).
 19. Jordan, A. *et al.* Inductive heating of ferrimagnetic particles and magnetic fluids: Physical evaluation of their potential for hyperthermia. *Int. J. Hyperth.* **9**, 51–68 (1993).
 20. Cabrera, D., Camarero, J., Ortega, D. & Teran, F. J. Influence of the aggregation, concentration, and viscosity on the nanomagnetism of iron oxide nanoparticle colloids for magnetic hyperthermia. *J. Nanoparticle Res.* **17**, 121 (2015).
 21. Di Corato, R. *et al.* Magnetic hyperthermia efficiency in the cellular environment for different nanoparticle designs. *Biomaterials* **35**, 6400–6411 (2014).
 22. Aires, A., Cabrera, D., Alonso-Pardo, L. C., Cortajarena, A. L. & Teran, F. J. Elucidation of the Physicochemical Properties Ruling the Colloidal Stability of Iron Oxide Nanoparticles under Physiological Conditions. *ChemNanoMat* **3**, 183–189 (2017).
 23. Blanco-Andujar, C. *et al.* Real-time tracking of delayed-onset cellular apoptosis induced by intracellular magnetic hyperthermia. *Nanomedicine* **11**, 121–136 (2016).
 24. Engelmann, U. M. *et al.* Combining Bulk Temperature and Nanoheating Enables Advanced Magnetic Fluid Hyperthermia Efficacy on Pancreatic Tumor Cells. *Sci. Rep.* **8**, 13210 (2018).
 25. Kuimova, M. K. *et al.* Imaging intracellular viscosity of a single cell during photoinduced cell death. *Nat. Chem.* **1**, 69–73 (2009).
 26. Levy, M. *et al.* Nanomagnetism reveals the intracellular clustering of iron oxide nanoparticles in the organism. *Nanoscale* **3**, 4402 (2011).
 27. Cabrera, D. *et al.* Unraveling viscosity effects on the hysteresis losses of magnetic nanocubes. *Nanoscale* **9**, 5094–5101 (2017).
 28. Na, H. Bin, Song, I. C. & Hyeon, T. Inorganic nanoparticles for MRI contrast agents. *Adv. Mater.* **21**, 2133–2148 (2009).
 29. Lee, N. & Hyeon, T. Designed synthesis of uniformly sized iron oxide nanoparticles for efficient magnetic resonance

- imaging contrast agents. *Chem. Soc. Rev.* **41**, 2575–2589 (2012).
30. Schmitz, S. A. *et al.* Magnetic resonance imaging of atherosclerotic plaques using superparamagnetic iron oxide particles. *J. Magn. Reson. Imaging* **14**, 355–361 (2001).
 31. Sun, C., Lee, J. S. H. & Zhang, M. Magnetic nanoparticles in MR imaging and drug delivery. *Adv. Drug Deliv. Rev.* **60**, 1252–1265 (2008).
 32. Lelong, F., Gradeck, M., Maillet, D. & Seiler, N. Experimental study of heat transfer between droplets and wall in Leidenfrost regime. *7th Int. Conf. Multiph. flow* **1**, 1–7 (2010).
 33. Corot, C., Robert, P., Idée, J. M. & Port, M. Recent advances in iron oxide nanocrystal technology for medical imaging. *Adv. Drug Deliv. Rev.* **58**, 1471–1504 (2006).
 34. Jun, Y. W. *et al.* Nanoscale Size Effect of Magnetic Nanocrystals and Their Utilization for Cancer Diagnosis via Magnetic Resonance Imaging. *J. Am. Chem. Soc.* **127**, 5732–5733 (2005).
 35. Bonnemain, B. Superparamagnetic Agents in Magnetic Resonance Imaging: Physicochemical Characteristics and Clinical Applications A Review. *J. Drug Target.* **6**, 167–174 (1998).
 36. Josephson Lee, Lewis Jerome, Jacobs Paula, Hahn Peter, S. D. The effect of iron oxides on proton relaxivity. *Magn. Reson. Imaging* **6**, 647–653 (1988).
 37. Materia, M. E. *et al.* Mesoscale Assemblies of Iron Oxide Nanocubes as Heat Mediators and Image Contrast Agents. *Langmuir* **31**, 808–816 (2015).
 38. Bigall, N. C. *et al.* Colloidal ordered assemblies in a polymer shell - A novel type of magnetic nanobeads for theranostic applications. *Chem. Mater.* **25**, 1055–1062 (2013).
 39. Gleich, B. & Weizenecker, J. Tomographic imaging using the nonlinear response of magnetic particles. *Nature* **435**, 1214–1217 (2005).
 40. Saritas, E. U. *et al.* Magnetic particle imaging (MPI) for NMR and MRI researchers. *J. Magn. Reson.* **229**, 116–126 (2013).
 41. Goodwill, P. W. *et al.* X-Space MPI: Magnetic nanoparticles for safe medical imaging. *Adv. Mater.* **24**, 3870–3877 (2012).
 42. Bauer, L. M., Situ, S. F., Griswold, M. A. & Samia, A. C. S. High-performance iron oxide nanoparticles for magnetic particle imaging-guided hyperthermia (hMPI). *Nanoscale* **8**, 12162–12169 (2016).
 43. Patrick W. Goodwill and Steven M. Conolly. The X-Space Formulation of the Magnetic Particle Imaging Process: 1-D Signal, Resolution, Bandwidth, SNR, SAR, and Magnetostimulation. *IEEE Trans. Med. Imaging* **29**, 1851–1859

- (2010).
44. Knopp, T. *et al.* Model-Based Reconstruction for Magnetic Particle Imaging. **29**, 12–18 (2010).
 45. Rahmer, J., Weizenecker, J., Gleich, B. & Borgert, J. Analysis of a 3-D System Function Measured for Magnetic Particle Imaging. **31**, 1289–1299 (2012).
 46. Weizenecker, J. Three-dimensional real-time in vivo magnetic particle imaging. (2009). doi:10.1088/0031-9155/54/5/L01
 47. Lu, J., Kazmierczak, E., Manton, J. H. & Sinclair, R. Automatic Segmentation of Scaling in 2-D Psoriasis Skin Images. *IEEE Trans. Med. Imaging* **32**, 719–730 (2013).
 48. Goodwill, P. W. *et al.* Ferrohydrodynamic relaxometry for magnetic particle imaging. *Appl. Phys. Lett.* **98**, 5–8 (2011).
 49. Ferguson, R. M., Khandhar, A. P. & Krishnan, K. M. Tracer design for magnetic particle imaging (invited). *J. Appl. Phys.* **111**, 07B318 (2012).
 50. Aoki, M., Banura, N., Nishimoto, K., Mimura, A. & Hamakawa, K. Usefulness of magnetic particle imaging for monitoring the therapeutic effect of magnetic hyperthermia. **53**, 252409 (2015).
 51. Kuboyabu, T. *et al.* Magnetic Particle Imaging for Magnetic Hyperthermia Treatment: Visualization and Quantification of the Intratumoral Distribution and Temporal Change of Magnetic Nanoparticles <i>in Vivo</i>. *Open J. Med. Imaging* **06**, 1–15 (2016).
 52. Hergt, R., Dutz, S. & Röder, M. Effects of size distribution on hysteresis losses of magnetic nanoparticles for hyperthermia. *J. Phys. Condens. Matter* **20**, (2008).
 53. Mehdaoui, B. *et al.* Optimal size of nanoparticles for magnetic hyperthermia: A combined theoretical and experimental study. *Adv. Funct. Mater.* **21**, 4573–4581 (2011).
 54. Noh, S. H. *et al.* Nanoscale magnetism control via surface and exchange anisotropy for optimized ferrimagnetic hysteresis. *Nano Lett.* **12**, 3716–3721 (2012).
 55. Pelaz, B. *et al.* Surface Functionalization of Nanoparticles with Polyethylene Glycol: Effects on Protein Adsorption and Cellular Uptake. *ACS Nano* 150625100151001 (2015). doi:10.1021/acsnano.5b01326
 56. Smolensky, E. D. *et al.* Scaling laws at the nanosize: The effect of particle size and shape on the magnetism and relaxivity of iron oxide nanoparticle contrast agents. *J. Mater. Chem. B* **1**, 2818–2828 (2013).
 57. Allione, M. *et al.* Rod-shaped nanostructures based on superparamagnetic nanocrystals as viscosity sensors in liquid. *J. Appl. Phys.* **110**, 064907 (2011).

58. Walter, A. *et al.* Mastering the shape and composition of dendronized iron oxide nanoparticles to tailor magnetic resonance imaging and hyperthermia. *Chem. Mater.* **26**, 5252–5264 (2014).
59. Itoh, H. & Sugimoto, T. Systematic control of size, shape, structure, and magnetic properties of uniform magnetite and maghemite particles. *J. Colloid Interface Sci.* **265**, 283–295 (2003).
60. Xia, Y., Xiong, Y., Lim, B. & Skrabalak, S. E. Shape-controlled synthesis of metal nanocrystals: Simple chemistry meets complex physics? *Angew. Chemie - Int. Ed.* **48**, 60–103 (2009).
61. Lin, X. M. & Samia, A. C. S. Synthesis, assembly and physical properties of magnetic nanoparticles. *J. Magn. Magn. Mater.* **305**, 100–109 (2006).
62. Xu, Y., Sherwood, J., Qin, Y., Holler, R. A. & Bao, Y. A general approach to the synthesis and detailed characterization of magnetic ferrite nanocubes. *Nanoscale* **7**, 12641–12649 (2015).
63. Sathya, A. *et al.* CoFe_{3-x}O₄ Nanocubes for Theranostic Applications: Effect of Cobalt Content and Particle Size. *Chem. Mater.* [acs.chemmater.5b04780](https://doi.org/10.1021/acs.chemmater.5b04780) (2016). doi:10.1021/acs.chemmater.5b04780
64. Cristina, A. & Samia, S. Structural effects on the magnetic hyperthermia properties of iron oxide nanoparticles. *Prog. Nat. Sci. Mater. Int.* **26**, 440–448 (2016).
65. Carta, D. *et al.* A Structural and Magnetic Investigation of the Inversion Degree in Ferrite Nanocrystals MFe₂O₄ (M = Mn, Co, Ni). *J. Phys. Chem. C* **113**, 8606–8615 (2009).
66. Jang, J. *et al.* Critical Enhancements of MRI Contrast and Hyperthermic Effects by Dopant-Controlled Magnetic Nanoparticles. *Angew. Chemie* **121**, 1260–1264 (2009).
67. Wu, W., He, Q. & Jiang, C. Magnetic iron oxide nanoparticles: Synthesis and surface functionalization strategies. *Nanoscale Res. Lett.* **3**, 397–415 (2008).
68. Gupta, A. K. & Gupta, M. Synthesis and surface engineering of iron oxide nanoparticles for biomedical applications. *Biomaterials* **26**, 3995–4021 (2005).
69. Anselmo, A. C. & Mitragotri, S. A Review of Clinical Translation of Inorganic Nanoparticles. *AAPS J.* **17**, 1041–1054 (2015).
70. Song, Q. & Zhang, Z. J. Controlled Synthesis and Magnetic Properties of Bimagnetic Spinel Ferrite CoFe₂O₄ and MnFe₂O₄ Nanocrystals with Core–Shell Architecture. *J. Am. Chem. Soc.* **134**, 10182–10190 (2012).
71. Guardia, P. *et al.* One pot synthesis of monodisperse water soluble iron oxide nanocrystals with high values of the specific absorption rate. *J. Mater. Chem. B* **2**, 4426 (2014).
72. Martinez-boubeta, C. *et al.* Learning from Nature to Improve the Heat Generation of Iron-Oxide Nanoparticles for

73. Berkowitz, A. E. & Schuele, W. J. Magnetic Properties of Some Ferrite Micropowders. *J. Appl. Phys.* **30**, S134–S135 (1959).
74. Lee, J.-G., Park, J. Y., Oh, Y.-J. & Kim, C. S. Magnetic properties of CoFe₂O₄ thin films prepared by a sol-gel method. *J. Appl. Phys.* **84**, 2801 (1998).
75. Sathya, A. *et al.* Co_xFe_{3-x}O₄ Nanocubes for Theranostic Applications: Effect of Cobalt Content and Particle Size. *Chem. Mater.* [acs.chemmater.5b04780](https://doi.org/10.1021/acs.chemmater.5b04780) (2016). doi:10.1021/acs.chemmater.5b04780
76. Horev-Azaria, L. *et al.* Predictive Toxicology of cobalt ferrite nanoparticles: comparative in-vitro study of different cellular models using methods of knowledge discovery from data. *Part. Fibre Toxicol.* **10**, 32 (2013).
77. Goldhaber, S. B. Trace element risk assessment: essentiality vs. toxicity. *Regul. Toxicol. Pharmacol.* **38**, 232–242 (2003).
78. Ammar, S. *et al.* Magnetic properties of zinc ferrite nanoparticles synthesized by hydrolysis in a polyol medium. *J. Phys. Condens. Matter* **18**, 9055–9069 (2006).
79. Greneche, J. Magnetic properties of nanostructured ferrimagnetic zinc ferrite. **12**, 7795–7805 (2000).
80. Naseri, M. G., Saion, E. B., Hashim, M., Shaari, A. H. & Ahangar, H. A. Synthesis and characterization of zinc ferrite nanoparticles by a thermal treatment method. *Solid State Commun.* **151**, 1031–1035 (2011).
81. Bárcena, C. *et al.* Zinc ferrite nanoparticles as MRI contrast agents. *Chem. Commun.* **0**, 2224 (2008).
82. Chen, Z. P., Fang, W. Q., Zhang, B. & Yang, H. G. High-yield synthesis and magnetic properties of ZnFe₂O₄ single crystal nanocubes in aqueous solution. *J. Alloys Compd.* **550**, 348–352 (2013).
83. Wan, J., Jiang, X., Li, H. & Chen, K. Facile synthesis of zinc ferrite nanoparticles as non-lanthanide T1 MRI contrast agents. *J. Mater. Chem.* **22**, 13500 (2012).
84. Köseoğlu, Y., Baykal, A., Gözüak, F. & Kavas, H. Structural and magnetic properties of Co_xZn_{1-x}Fe₂O₄ nanocrystals synthesized by microwave method. *Polyhedron* **28**, 2887–2892 (2009).
85. Arulmurugan, R., Jeyadevan, B., Vaidyanathan, G. & Sendhilnathan, S. Effect of zinc substitution on Co–Zn and Mn–Zn ferrite nanoparticles prepared by co-precipitation. *J. Magn. Magn. Mater.* **288**, 470–477 (2005).
86. Köseoğlu, Y., Alan, F., Tan, M., Yilgin, R. & Öztürk, M. Low temperature hydrothermal synthesis and characterization of Mn doped cobalt ferrite nanoparticles. *Ceram. Int.* **38**, 3625–3634 (2012).

87. Paulsen, J. A., Ring, A. P., Lo, C. C. H., Snyder, J. E. & Jiles, D. C. Manganese-substituted cobalt ferrite magnetostrictive materials for magnetic stress sensor applications. *J. Appl. Phys.* **97**, 044502 (2005).
88. Vaidyanathan, G. & Sendhilnathan, S. Characterization of $\text{Co}_{1-x}\text{Zn}_x\text{Fe}_2\text{O}_4$ nanoparticles synthesized by co-precipitation method. *Phys. B Condens. Matter* **403**, 2157–2167 (2008).
89. Sanpo, N., Berndt, C. C., Wen, C. & Wang, J. Transition metal-substituted cobalt ferrite nanoparticles for biomedical applications. *Acta Biomater.* **9**, 5830–5837 (2013).
90. Gharibshahian, M., Nourbakhsh, M. S. & Mirzaee, O. Evaluation of the superparamagnetic and biological properties of microwave assisted synthesized Zn & Cd doped CoFe_2O_4 nanoparticles via Pechini sol–gel method. *J. Sol-Gel Sci. Technol.* **85**, 684–692 (2018).
91. Ben Ali, M. *et al.* Effect of zinc concentration on the structural and magnetic properties of mixed Co–Zn ferrites nanoparticles synthesized by sol/gel method. *J. Magn. Magn. Mater.* **398**, 20–25 (2016).
92. SINGHAL, S., JAUHAR, S., CHANDRA, K. & BANSAL, S. Spin canting phenomenon in cadmium doped cobalt ferrites, $\text{CoCd}_x\text{Fe}_{2-x}\text{O}_4$ ($x = 0.0, 0.2, 0.4, 0.6, 0.8$ and 1.0), synthesized using sol–gel auto combustion method. *Bull. Mater. Sci.* **36**, 107–114 (2013).
93. Moyet, R. P., Cardona, Y., Vargas, P., Silva, J. & Uwakweh, O. N. C. Coercivity and superparamagnetic evolution of high energy ball milled (HEBM) bulk CoFe_2O_4 material. *Mater. Charact.* **61**, 1317–1325 (2010).
94. Wang, T. *et al.* Enhancing low-field magnetoresistance in magnetite nanoparticles via zinc substitution. *Phys. Chem. Chem. Phys.* **20**, 17245–17252 (2018).
95. Mameli, V. *et al.* Studying the effect of Zn-substitution on the magnetic and hyperthermic properties of cobalt ferrite nanoparticles. *Nanoscale* **8**, 10124–10137 (2016).
96. Ranvah, N. *et al.* Temperature Dependence of Magnetic Properties of $\text{CoAl}_x\text{Fe}_{2-x}\text{O}_4$. *IEEE Trans. Magn.* **45**, 4261–4264 (2009).
97. Ranvah, N. *et al.* Temperature dependence of magnetic anisotropy of germanium/cobalt cosubstituted cobalt ferrite. *J. Appl. Phys.* **105**, 07A518 (2009).
98. Topkaya, R. *et al.* Surface spin disorder and spin-glass-like behaviour in manganese-substituted cobalt ferrite nanoparticles. *J. Nanoparticle Res.* **14**, 1156 (2012).
99. Orlando, A. *et al.* Iron oxide nanoparticles surface coating and cell uptake affect biocompatibility and inflammatory responses of endothelial cells and macrophages. *J. Nanoparticle Res.* **17**, 351 (2015).
100. Di Corato, R. *et al.* Water solubilization of hydrophobic nanocrystals by means of poly(maleic anhydride-alt-1-octadecene). *Journal of Materials Chemistry* **18**, 1991 (2008).

101. Gupta, A. K. & Gupta, M. Synthesis and surface engineering of iron oxide nanoparticles for biomedical applications. *Biomaterials* **26**, 3995–4021 (2005).
102. Verde, E. L. *et al.* Field dependent transition to the non-linear regime in magnetic hyperthermia experiments: Comparison between maghemite, copper, zinc, nickel and cobalt ferrite nanoparticles of similar sizes. *AIP Adv.* **2**, (2012).
103. Nidhin, M. *et al.* Flower shaped assembly of cobalt ferrite nanoparticles: application as T2 contrast agent in MRI. *RSC Adv.* **3**, 6906 (2013).
104. Cullity, B. D. & Graham, C. D. *Introduction to Magnetic Materials*. (Wiley, 2011).
105. Moumen, N. & Pileni, M. P. New Syntheses of Cobalt Ferrite Particles in the Range 2–5 nm: Comparison of the Magnetic Properties of the Nanosized Particles in Dispersed Fluid or in Powder Form. *Chem. Mater.* **8**, 1128–1134 (1996).
106. López-Ortega, A. *et al.* Strongly exchange coupled inverse ferrimagnetic soft/hard, $\text{MnxFe}_{3-x}\text{O}_4/\text{FexMn}_{3-x}\text{O}_4$, core/shell heterostructured nanoparticles. *Nanoscale* **4**, 5138 (2012).
107. Vuong, Q. L., Berret, J. F., Fresnais, J., Gossuin, Y. & Sandre, O. A universal scaling law to predict the efficiency of magnetic nanoparticles as MRI T2-contrast agents. *Adv. Healthc. Mater.* **1**, 502–512 (2012).
108. Arami, H., Ferguson, R. M., Khandhar, A. P. & Krishnan, K. M. Size-dependent ferrohydrodynamic relaxometry of magnetic particle imaging tracers in different environments. *Med. Phys.* **40**, 071904 (2013).
109. Kwon, Y.-M. *et al.* Dose-dependent cytotoxicity of clinically relevant cobalt nanoparticles and ions on macrophages *in vitro*. *Biomed. Mater.* **4**, 025018 (2009).
110. Horev-Azaria, L. *et al.* Predictive Toxicology of Cobalt Nanoparticles and Ions: Comparative In Vitro Study of Different Cellular Models Using Methods of Knowledge Discovery from Data. *Toxicol. Sci.* **122**, 489–501 (2011).
111. Pellegrino, T. *et al.* Hydrophobic nanocrystals coated with an amphiphilic polymer shell: A general route to water soluble nanocrystals. *Nano Lett.* **4**, 703–707 (2004).
112. Sperling, R. a., Pellegrino, T., Li, J. K., Chang, W. H. & Parak, W. J. Electrophoretic Separation of Nanoparticles with a Discrete Number of Functional Groups. *Adv. Funct. Mater.* **16**, 943–948 (2006).
113. Di Corato, R. *et al.* Magnetic-fluorescent colloidal nanobeads: Preparation and exploitation in cell separation experiments. *Macromol. Biosci.* **9**, 952–958 (2009).

Chapter 2. Nanocubes for Blood Brain Barrier transportation and neurodegenerative diseases treatment

2.1 Introduction

2.1.1 Neurodegenerative Brain diseases

Neurodegenerative brain diseases are adult-onset diseases in which degeneration of specific neuronal populations of the central nervous system plays a central role.¹ In this millennium, neurological disorders are growing due to the aging of the population, with a consequent high social impact due to their prevalence and/or high morbidity and mortality.² From last estimations, there were between 17.80 and 26.70 million patients with Alzheimer's diseases (AD), 7.12 million to 10.68 million patients with vascular dementia (VD), 7 to 10 million patients with Parkinson's disease (PD) and about 350 000 patients with amyotrophic lateral sclerosis (ALS).³ These diseases are all characterized by abnormal accumulation of specific protein species, hence the term "proteinopathy" to describe these disorders.⁴ Other common factors that are potential mediators of the disease process include: increased oxidative stress (reactive oxygen species); impaired energy metabolism; lysosomal dysfunction; inflammation; cytotoxicity; necrosis; and/or apoptosis.⁵ Genetics plays a major role in all these diseases, which in general result from a complex combination of multiple genetic risk and protective factors. Besides the genetic bases, environmental factors (such as diet, pollution, etc.) represent additional individual's risk to develop the disease at a given point in life.⁵⁻⁹ For instance, it is well established that Down's syndrome and Alzheimer's disease are related,¹⁰ and Down's patients have a 100% probability of developing Alzheimer's disease.¹¹ Individuals with Down's syndrome have an extra copy of chromosome 21, which contains the gene for the amyloid precursor protein.¹² Amyloidogenic processing of amyloid precursor protein gives rise to the amyloid β -peptide that is the main constituent of the plaques found in the brains of Alzheimer patients. Amyloid- β is 40 to 42 amino acids in length and is generated by proteolytic cleavage of the much larger amyloid precursor protein (APP), a transmembrane protein constituted by a single membrane-spanning domain .¹³⁻¹⁵

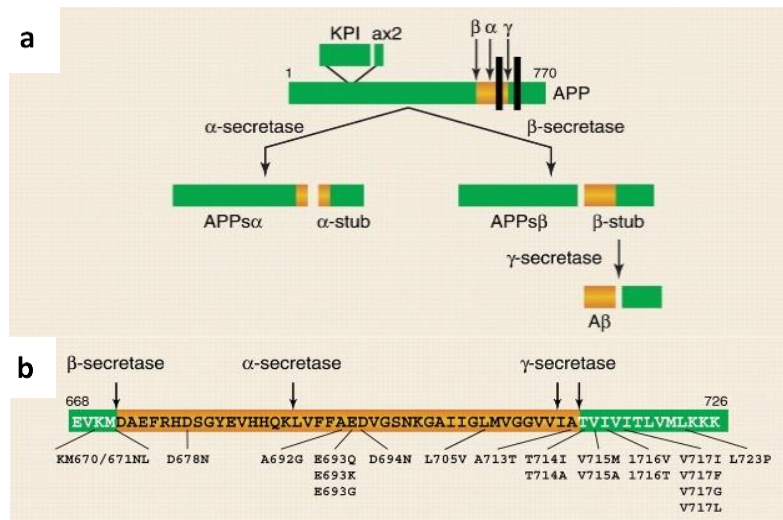


Figure 3 a) Generation of amyloid-β (Aβ) from the amyloid precursor protein (APP). Cleavage by β-secretase generates the N terminus and intramembranous cleavage by γ-secretase gives rise to the C terminus of amyloid-β. Cleavage by α-secretase precludes Aβ formation. **b)** Twenty missense mutations in APP are shown. Single-letter abbreviations for amino acid residues: A, Ala; C, Cys; D, Asp; E, Glu; F, Phe; G, Gly; H, His; I, Ile; K, Lys; L, Leu; M, Met; N, Asn; P, Pro; Q, Gln; R, Arg; S, Ser; T, Thr; V, Val; W, Trp; Y, Tyr. Adapted with permission from reference 7. Copyright 2006, Science.

In the extracellular domain of APP is possible to find the N terminus of amyloid-β, 28 amino acids from the transmembrane region, and its C terminus is located in the transmembrane region. The β-secretase and γ-secretase are the enzymes whose activity gives rise to the N and C termini, respectively. Instead the α-secretase, cleaves between residues 16 and 17, precluding amyloid-β formation. The major species of amyloid-β are 40 or 42 amino acids long, and it is the more amyloidogenic.¹⁶ Apart from several other environmental or genetic factors, oxidative stress (OS) leading to free radical attack on neural cells contributes calamitous role to neurodegeneration. OS is the result of unregulated production of reactive oxygen species (ROS), obtained by a number of different pathways, including direct interactions between redox-active metals and oxygen species via reactions such as the Fenton and Haber–Weiss reactions, or via indirect pathways involving the calcium activation of metal-enzymes such as phospholipases and nitric oxide synthase.¹⁶ The excessive generation of ROS leads to dysregulation of intracellular calcium signaling, and such dysregulation has been observed in neurodegenerative diseases in which aberrant calcium levels stimulate an apoptotic cascade.^{17–21} Another important factor in the neuro-degenerative disorders evolution is represented by the neuro-inflammatory events. The brain is considered an “immunologically protected” organ, as it is provided of an efficient dedicated neuro-immune system. The primary constituents of this system are glial cells (microglia and astrocytes) and their interaction with the peripheral immune system is poorly understood since the immune cells are not able to penetrate the blood brain barrier (BBB).^{22–24} Dysfunction of this barrier is well known to occur in neuro-

inflammatory disorders, including Alzheimer's disease, Parkinson disease and Amyotrophic lateral sclerosis,²⁵ and is mediated by the activation of endothelial cells that display an altered phenotype and a decrease in expression of tight junction proteins. These changes are also observed during ageing²⁶ and they may also explain the increase in susceptibility to neuro-inflammation and neurodegenerative disorders in the elderly population.^{4,27}

2.1.2 Blood Brain Barrier

The blood brain barrier (BBB) is a diffusion barrier of the central nervous system (CNS), essential to maintain his homeostasis and normal functions. The BBB protect the CNS from fluctuation in plasma composition or harmful circulating agents such as neurotransmitters and xenobiotics, limiting and selecting the accesses of the blood-derived molecules.²⁵

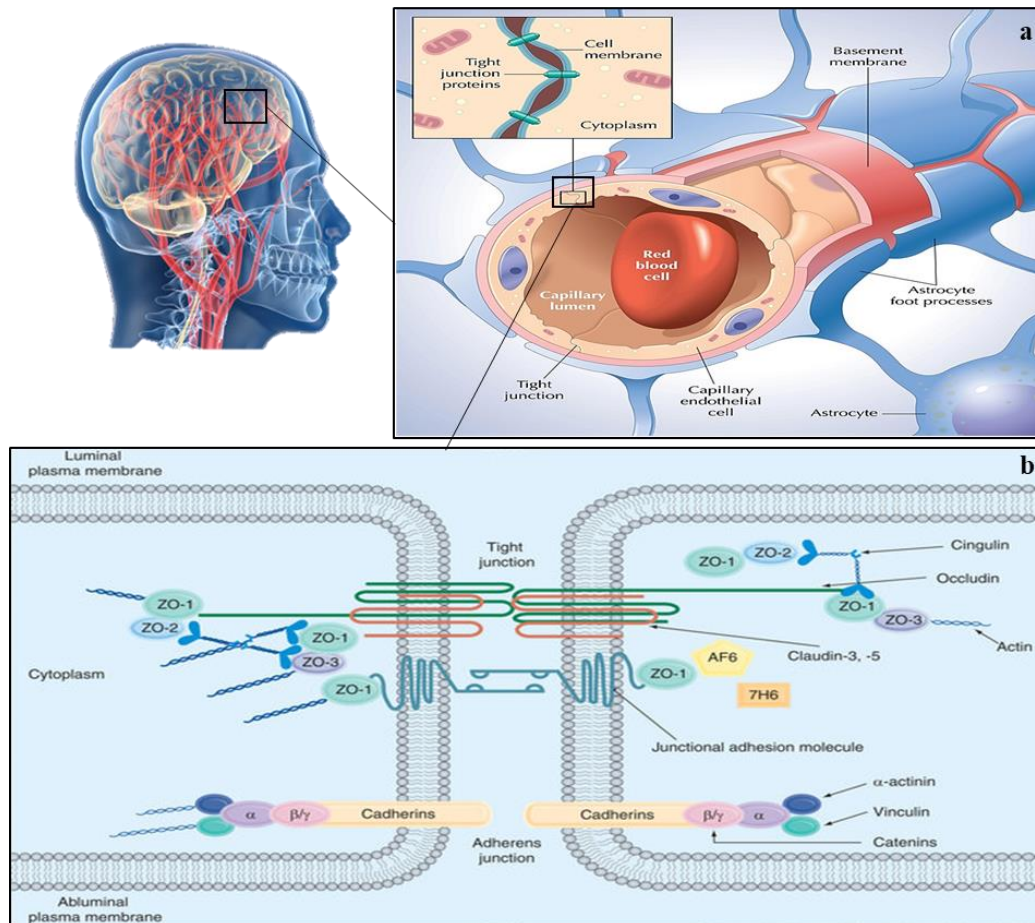


Figure 2 a) Main constituents of the blood–brain barrier. The barrier is formed by specialized endothelial cells connected by multi-protein complexes, tight junctions (TJs), junctional adhesion molecules, astrocytes, pericytes and basement membrane. Astrocytes provide the cellular link to the neurons. **b)** Molecular composition of endothelial TJs. Simplified scheme showing the molecular composition of endothelial TJs. Occludin and the claudins (proteins with four transmembrane domains and two extracellular loops) are the most important membranous components. Within the cytoplasm are many first-order adaptor proteins, including zonula occludens 1, 2 and 3 (ZO-1–3), the ZO-1-associated nucleic acid-binding protein and afadin (AF6). All of these adaptor and regulatory/signaling proteins control the interaction of the membranous components with the actin/vinculin-based cytoskeleton. In epithelial cells, tight and adherens junctions are strictly separated from each other, but in endothelial cells these junctions are intermingled. The most important molecule of endothelial adherens junctions is vascular endothelial cadherin (VE-cadherin). Adapted with permission of J.Perkins and reference ²⁸.

It is composed by specialized endothelial cells connected by multi-protein complexes, tight junctions (TJs), junctional adhesion molecules, astrocytes, pericytes and basement membrane.²⁹ These endothelial cells differ from endothelial cells present in the rest of the body by the absence of fenestrations and more efficient cell-to-cell junctions.^{30,31} In addition, they present higher number of TJ strands as well as the frequency of their ramifications.³² The TJ consists of three integral membrane proteins, namely, claudin, occludin, and junction adhesion molecules, and a number of cytoplasmic accessory proteins including zonula occludens 1-2-3 (ZO-1, ZO-2, ZO-3), cingulin, and others.^{33,34} The cytoplasmic proteins link membrane proteins to actin, which is the primary cytoskeleton protein for the maintenance of structural and functional integrity of the endothelium. Another family of protein, involved in the endothelial cells spacing is the Adherens junctions (AJs), composed of a cadherin–catenin complex and its associated proteins.³³ Endothelial cell TJ junctions limit the paracellular flux of hydrophilic molecules across the BBB, promoting the free diffusion of small lipophilic molecules as well as O₂ and CO₂ across plasma membranes along their concentration gradient.³⁵ The nutrients enter into the brain by different pathways. Among them glucose and amino acids cross the BBB via transporters, whereas larger molecules than small nutrients including for instance insulin, leptin, and iron transferrin are able to pass through the BBB by receptor-mediated endocytosis.^{36–38} Transit restrictions imposed by the BBB represent the most important barrier to overcome in drug delivery to target the CNS.

2.1.3 Nanoparticles: brain drug delivery

Presently, there are no effective therapies for neurodegenerative diseases, even if candidate drugs may be already available. Up to now, the biggest limitation to the penetration of the majority of drugs and imaging agents is due to the presence of the BBB that limits or prevents their entrance, causing unwanted peripheral side effects.³⁹ However, the BBB represents a tough obstacle only in healthy subject. Indeed in some brain diseases, such as Alzheimer's disease or amyotrophic lateral sclerosis the BBB integrity is altered.⁴⁰ An alternative approach to facilitate the overcome of the BBB is by using NPs.⁴¹ NPs may cross the BBB without a functionalization (*e.g.* gold NPs)³⁹ of their surface or may be properly functionalized with molecules able to promote the entrance of drugs and/or contrast agents into the brain.⁴¹ Moreover, NPs possess additional positive features given by the functionalization such as a high chemical and biological stability, feasibility of incorporating either hydrophilic or hydrophobic molecules. Furthermore, NPs can be administered by a variety of routes including

oral, inhalational and parenteral).⁴²⁻⁴⁴ At the present, the use of nanoparticles for drug delivery purposes are under investigation, in cancer therapy but also in the treatment of other neurodegenerative disorders. Among all types of NPs, biocompatible iron oxide nanoparticles (IONPs) with a proper surface coating conjugated to targeting ligands/proteins were proven to act as drug delivery,⁴⁵ magnetic hyperthermia treatment (MHT),⁴⁶ magnetic resonance imaging (MRI)⁴⁷ and magnetic particles imaging (MPI).⁴⁸ In order to target the A β (1-42) peptide, recent studies, have used lipid-based NPs exposing Phosphatidic Acid (PA) as targeting moieties for amyloid fibrils. In these work besides showing the specific binding towards the A β aggregates, the disaggregating effects on A β plaques were also proven.^{49,50} NPs exposing PA can be used also for AD diagnostic purpose, the PA can detect the presence of amyloids moieties in the blood. In addition to the disaggregation effect, it is possible to obtain an antioxidant effect using Ferulic Acid (FA).⁵¹ *Picone and colleagues* were using Solid Lipid Nanoparticles (SLNs) loaded with FA, to decrease ROS generation, restore mitochondrial membrane potential and to reduce cytochrome *c* release (involved in apoptosis process) and reduce intrinsic pathway apoptosis activation. Further, FA modulate the expression of peroxiredoxin, an anti-oxidative protein, and attenuate phosphorylation of ERK1/2 activated by A β oligomers.⁵² The interaction between NPs and amyloid fibril can occur, not only due to their functionalization, but also with the rough NPs (without functionalization), as evidenced by the study of Skaat. They used γ -Fe₂O₃ nanoparticles self-assemble at the surfaces of the amyloid fibrils probably through charge and/or hydrophobic interactions.⁵³ Alzheimer's disease and other neurodegenerative disorders like Parkinson's disease, also cause an alteration of the neuronal activity.^{54,55} *Chen et al.* demonstrated the possibility to exploit MNPs to provide a minimally invasive and remote neural excitation for treatment of these diseases. This takes place through the activation of the heat-sensitive capsaicin receptor TRPV1 by MNPs under hyperthermia treatment.⁵⁶ As shown above, to provide a therapy for these disorders it is necessary to pass the blood brain barrier. Different approaches have been tested to enable the overcome of the barrier and the delivery of drugs. These explorative strategies have been ranging from invasive techniques, *e.g.*, through osmotic opening of the BBB,⁵⁷ to chemical modifications of drugs. These would take advantage of physiological carrier-mediated transports, or exploiting the so-called "Trojan horse" technology, which consists of coupling drugs that are not able to cross the BBB alone to molecules which can easily go through.⁵⁸ To this aim, recent studies of *Tabatabaei et al.* revealed encouraging and innovative results.⁵⁹ They examined the blood-brain barrier's permeability in the presence of moderate heat induced by MNPs in an AMF, taking advantage of the fact that the permeability to drugs of the BBB between tight junctions is known to

increase in response to a physiologically relevant temperature increase (38–39 °C).^{59,60} In this temperature range it is possible to observe a reversible disruption of the barrier on the surface of the brain.⁶¹ In this pioneering study, the aim was to show how the heat generated by the MNPs under the AMF could improve the cross among the BBB of large dye molecules. The authors were also showing that under the MHT, the barrier was not permanent damaged by the thermal treatment but it was capable to naturally recover the BBB function. This provides the possibility to access the brain tissue with higher spatial precision, advanced control and lower immune reaction. This method is the most encouraging mechanism to facilitate the transcellular transport of NPs from the blood to the brain. Nevertheless, in this *in-vivo* study commercial available MNPs were used with low magnetic properties. For this reason, to have a local heat increase they were forced to administer a huge amount of MNPs (60µL at 12g/L). Other strategy currently under study are receptor- and adsorptive-mediated transcytosis.⁶² In the latter case, *Sancini and colleagues* have shown that it is possible to functionalize nanoliposomes (NL) with a modified HIV Transactivating Transcriptional Activator (TAT) peptide, which was covalently attached to NL surface *via* a thiol-maleimide reaction. The TAT-peptide can enhance the BBB crossing by the NP, based on the evidence that its coupling to NP can facilitate their efficient translocation through the cell membrane, bypassing the endocytic pathway.^{63,64}

As explained above (also in the previous chapter), the MNPs must have the combined features of good magnetic properties, biocompatibility and interactive functions at the surface⁶⁵ for passing the BBB and to be used for diseases treatments. The surface of these particles can be modified through the creation of few atomic layers of a polymer⁶⁶, a metal (*e.g.*, gold)⁶⁷ or oxide surfaces (*e.g.*, silica or alumina)⁶⁸, suitable for further functionalization by the attachment of various bioactive molecules.⁴⁰ They can be either dispersed in a large volume of a polymeric bead or occur as core in colloidal reagent with a biodegradable shell.^{69,70} The MNPs, with suitable surface characteristics, have a high potential in many applications both *in-vitro* and *in-vivo*. As discussed up to now, functionalized MNPs are the most promising way to overcome the BBB and provide a specific and effective treatment for neurodegenerative disease.

2.2 Results and discussions

2.2.1 Nanoparticles for BBB permeation study

This chapter is referred to experiments carried out in the first part of the Ph.D. period. The goal of this study was to increase the MNPs transportation through the BBB. To reach the scope two strategies were followed: the first one is based on the local damages of the barrier driven by the heat up properties of the MNPs and the second is based on the functionalization of the MNPs with TAT to increase the trans-cellular transportation. These two strategies could be merged and used in combination. At the starting point of my Ph.D., the MNPs candidates for these tasks were cubic shaped iron oxide (IONCs) and cubic-shaped cobalt ferrite (CoFeNCs). A lot of work was done to decrease the size of these NCs below 16 nm (Chapter 1), in particular for CoFeNCs. The main reason was practical, because bigger magnetic NCs means that are more interacting each other, being far from the critical size in which they are superparamagnetic. During the functionalization, the interactions were playing a crucial role as the NPs aggregation easily occurred when working with NCs bigger than 15 nm. Without stable and individually coated NPs, the heat performance as well as their surface functionalization was compromised. Once were obtained the NCs in the requested size range with good size and shape distributions (Figure 3 a and b), the CoFeNCs starts to show their potential with respect to the iron oxide ones. The SAR performances of the cobalt substituted MNPs were 5 times higher than the iron oxide NCs at low frequency (100 kHz) (Figure3c). This result highlight the possibility to decrease drastically their dose to provide an effective MHT and at the same time, the concentration reduction could mitigate the possible cytotoxic effect given by the cobalt ions.

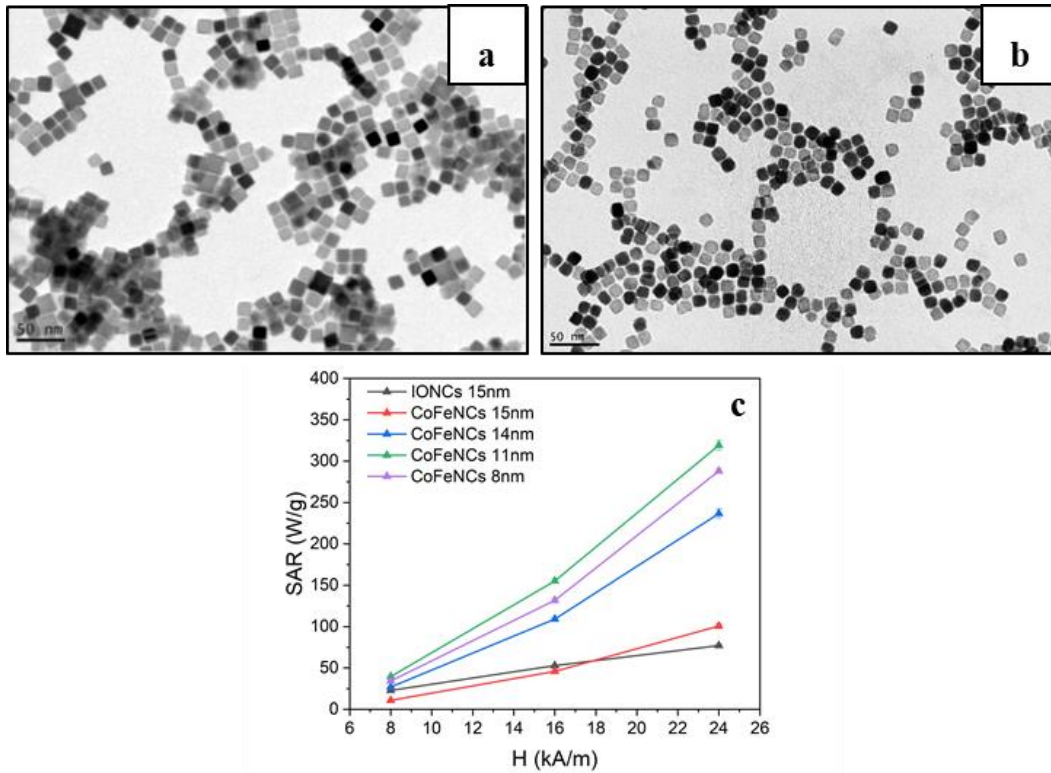


Figure 3. TEM images of **a)** IONCS 15 ± 2 nm and **b)** CoFeNCs 12 ± 1 nm as synthesized. These samples were used for the BBB transportation experiments after proper functionalization. **c)** SAR measurements graph of different sizes of CoFeNCs (8-11-14-15nm) and IONCs (15nm). The measurements were done with a field of 8-16-24 kA/m and 100kHz frequency.

2.2.2 PEG functionalization

The PEGylation of the NPs is commonly adopted to increase their stability in water or biological media.^{66,71–73} After the water transfer with PMAO (described in detail in the previous chapter), the NCs (either IONCs and CoFeNCs) were functionalized with Poly(ethylene) glycol diamine 2000 (NH₂-PEG-NH₂, MW2000) following a procedure developed by *Sperling et al.* with minor modifications.⁷⁴ This protocol is based on the reaction between the carboxyl groups present on the surface of the polymeric shell of the NCs and the amine terminated groups of the diamine PEG chain. They form a covalent bound via standard bioconjugation chemistry using 1-ethyl-3-(3-dimethylaminopropyl) carbodiimide hydro-chloride (EDC). By attaching the PEG molecules to the NPs, the resulting conjugate increases in size with respect to the polymer coated NPs. As it is visible from Figure 4a and b, the hydrodynamic diameter (dh) pass from 40 to 91nm when the PEG was attached and the intensity peak was shifted. The increase in size can be easily detected by their comparative migration on an agarose gel in electrophoresis. Negatively charged PMAO NCs migrate towards the positive pole; they become more retarded the larger the number of NH₂-PEG-NH₂ molecules attached, also because the positive charge of the amine groups reduce the overall negative charge (Figure 4c).

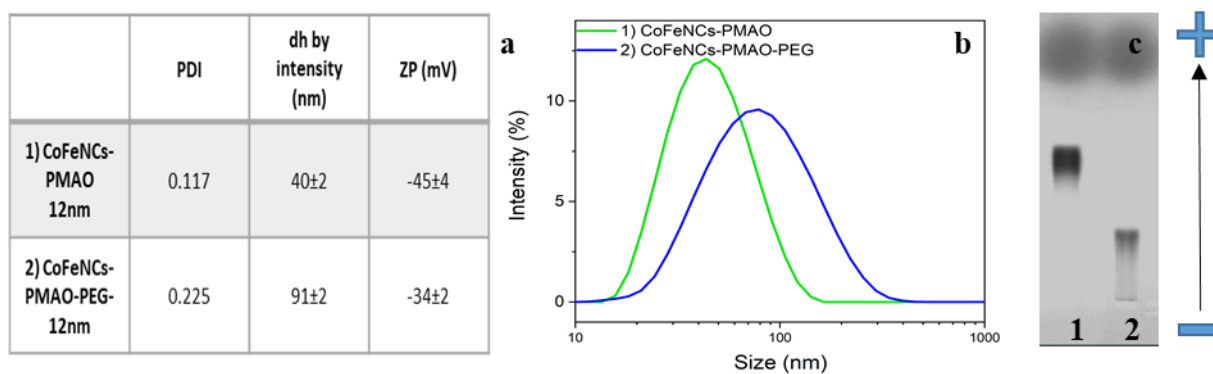


Figure 4. a) DLS table, b) Hydrodynamic size graph by intensity and c) gel electrophoresis in TBE at 100V for 45min of a 2% agarose gel loaded with CoFeNCs polymer coated with PMAO and PEGylated in water (each value is the result of three measurements repetition).

2.2.4 TAT functionalization

The TAT functionalization was done with the aim to increase the cell penetration of the NCs into the cells.⁷⁵⁻⁷⁷ A protocol for the functionalization of NCs (both iron oxide and cobalt ferrite) with TAT, previously developed in our group for spherical iron oxide nanocrystals, was optimized and adjusted,⁷⁸. The PEGylation was followed by the activation of the amine groups with sulfo-SMCC crosslinker and finally cysteine modified TAT sequences were bound to the maleimide moiety of the cross-linker, forming a stable bond. The peptide attachment was confirmed by the corresponding delay of the migration bands on the agarose gel (Figure 5 c-d) and by the increased hydrodynamic radius from 91 to 250 nm, before and after the TAT functionalization. In addition a reduction in surface charge from -3 to -28 mV of the NPs was measured (Figure 5a-b), probably given by the lysine and arginine residues. Moreover, Coomassie Blue staining (Figure 5d), that is selective for the peptide sequence; enable their visualization by color confirming the TAT co-localization with the NPs thus indicating the attachment of the TAT to the NCs surface. Starting from the published procedure⁷⁸, in which spherical NPs were used, many attempt were done to attach the TAT to NCs bigger than 16 nm but the aggregation of the NPs during the reaction was the principal problem. The procedure presents two separation steps with gel chromatography columns, to ensure the passage through the column and so the purification from the excess of the unbound moieties, the NPs has to be monodisperse. For this reason only NCs with low interparticles interactions, smaller than 16 nm were used, giving the attended results in terms of funcionalization quality.

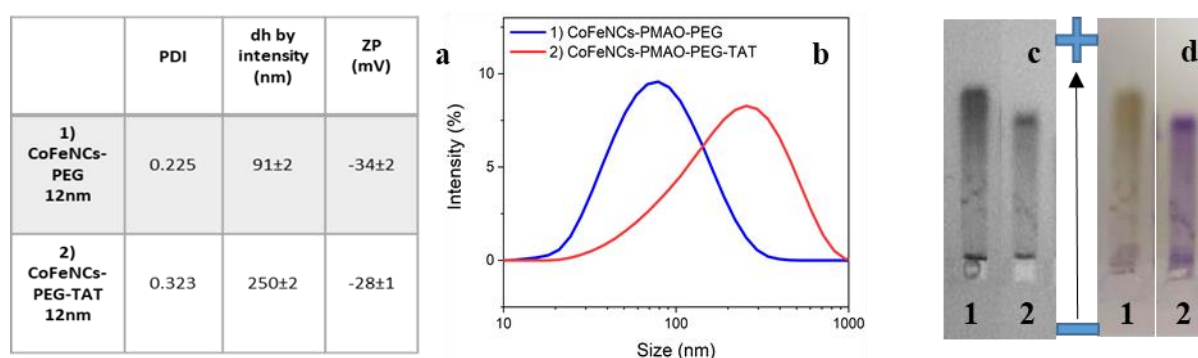


Figure 5. a) DLS table, b) Size graph by intensity and gel electrophoresis in TBE at 100V for 45min of a 2% agarose gel loaded c) without and d) with comassie blue staining of CoFeNCs PEGylated or with TAT (each value is the result of three measurements repetition).

2.2.5 BBB model study

Different *in vitro* BBB models can be found in literature.^{79, 80} These models have become essential as a tool to determine the ability of NPs to cross the BBB, enabling identification and evaluation of the optimal formulations for *in vivo* studies. For this study, a model based on the use of transwell inserts was chosen (Figure 6). A polyester membrane (3.0 μm pore size) constitutes the insert, which divides horizontally a standard well in two chambers: the apical and the basolateral. On top of the membrane, treated with type I collagen, mouse endothelial cells (bEnd3) were seeded enabling to form a monolayer. This model mimics a brain capillary, in which the endothelium divides the blood stream (apical compartment) from the brain (basolateral compartment).

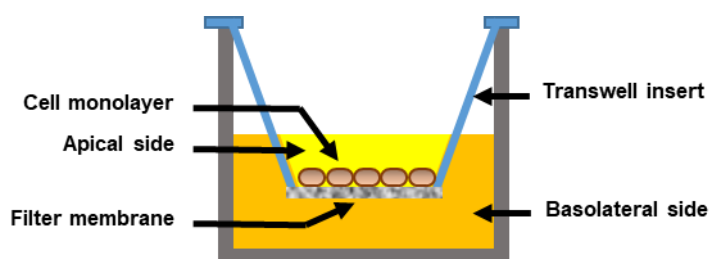


Figure 6 Scheme of the BBB model used in this work: a transwell insert with a 3 μm pore size of polyester membrane divides the well in two chambers, the apical and the basolateral chambers. The BBB is formed by a cell monolayer of bEnd3 (mouse brain endothelial) grown on a collagen type I layer that divide the cells from the polymeric membrane.

To evaluate the correct growing of the BBB model, different physiological tests were carried out. First of all, the TEER was measured. It is well known that there is a logarithmic relationship between the number of TJ strands and the TEER.^{34,81,82} Therefore, the complexity of the strands network can be used to predict the BBB permeability.⁸³

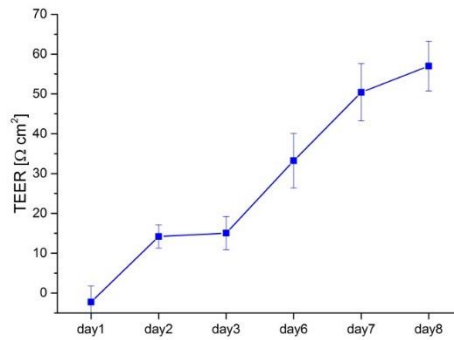


Figure 7 Graph of the transepithelial electrical resistance (TEER) values. The values were raising over a period of 8 days indicating the growing and the formation of a functional cells barrier (each value is the result of three measurements repetition).

Figure 7 shows the TEER vales. The values were raising over a period of 8 days, confirming the development of a healthy cellular barrier. To evidence the expression of TJ proteins, immunofluorescence was performed after 7-8 days from the bEnd3 seeding. In particular, Claudine 5 proteins (in red, Figure 8a) and the adherens junction proteins VE-Cadherin (in green, Figure 8b) were targeted with primary antibodies rabbit anti-Claudin-5 or VE-Cadherin and secondary antibodies Alexa 568 and Alexa 488. In Figure 8, it is clearly evident that the cells form a compact cells monolayer and the two stained proteins at the edge of the cells marked very well the TJs indicating a physiological protein expression. Additionally, was tried to target the TJ proteins zonula occludens 1(ZO-1) to compare the results with the Claudine 5 staining, but was found that with the bEnd3 cells works better the first two mentioned proteins.

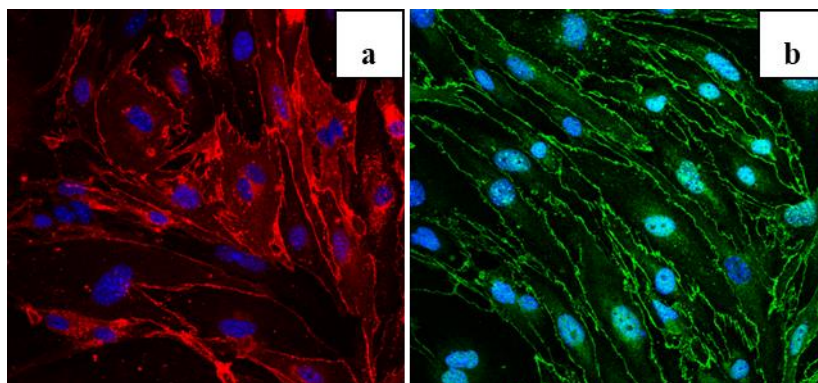


Figure 8 Junction immunostaining of bEnd3 cells, confocal images of **a**) Claudine 5 (red) and **b**) VE-Cadherin proteins (green) were stained with primary antibodies rabbit anti-Claudin-5 or VE-Cadherin and secondary antibodies Alexa 568 and Alexa 488 after 7 days of incubation. The TJ proteins are well expressed.

After eight days of incubation, the cell membrane was tested for the para-cellular transport assay, which is to evaluate the passage of fluorescent dye (FD-4kDa) molecules between adjacent endothelial cells. As it is visible from Figure 9, the transwell membrane treated only with the collagen (used as a reference) allowed the fast passage of the dye during the 4 hours of the experiment. Contrary, once the cell layer is present the transportation of the dye through the barrier became almost negligible. These outcomes prove the suitability of the model chosen for producing a good platform to test the NPs for brain application.

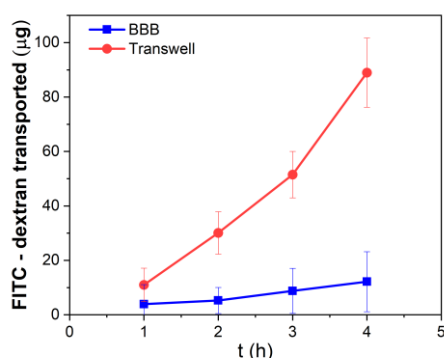


Figure 9 Permeability assay done with the FD4 dye on the transwell membrane treated with the collagen (type I) and on the complete model with the bEnd3 seeded. The permeability was evaluated by measuring the amount of the dye found in the basolateral chamber. The fluorescence of FD-4 kDa was determined using a spectrofluorimeter with an excitation/emission wavelength of 490/515 nm

2.2.6 Main features affecting NPs transportation through the BBB.

MNPs coating

NPs are gaining attention for the transportation of drugs through the BBB, thanks to their physico-chemical features and to the possibility of multi-functionalization.^{2,39} The interest was focus on magnetic NPs, since they can be manipulated by an external magnetic field, which can permeate the human tissue. However, due to the delicate brain environment, the NPs coating and functionalization had to be carefully chosen. A first preliminary study on the passive transportation (PP) of IONCs through the BBB was carried out. Two IONCs samples with different coating were tested: PMAO and PMAO functionalized with diamine-PEG. The PEGylation reduces opsonization and elimination of NPs, thus increasing blood circulation time, increasing the probability that the NPs will reach the brain before being recognized as foreign and being cleared from the body.⁸⁴ The experiment was conducted 7 days after the cells

seeding on the transwell membrane. After additionally 48 hours of incubation with the two different coated samples, the passage was evaluated quantitatively by elemental analysis, measuring the amount of iron found in the media of the apical compartment compared with the iron found in the media of the basolateral one.

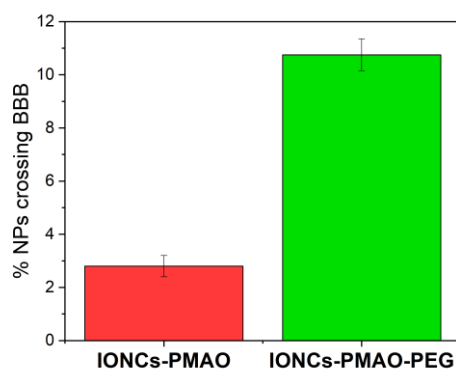


Figure 10 Percentage of IONCs-PMAO and IONCs-PMAO-diamine PEG that pass the BBB in a PP experiment. The passage was evaluated quantitatively by elemental analysis, measuring the amount of iron found in the media of the apical compartment compared with the iron found in the media of the basolateral one. The experiment was conducted after 48h of incubation with the two samples.

The PEGylation of the NP surface increases the sample's stability in culture media and prevents the aggregation on the transwell membrane, thus increasing of five times the passage of NPs through the epithelial layer (Figure 10). Given these results, it was decided to use only samples functionalized that had the PEG attached at the PMAO surface. Unfortunately, was not possible to test the MNPs functionalized with TAT on the BBB model. Further experiments are planned to test them.

MNPs composition

The permeability of the BBB between TJ is known to increase in response to a physiologically relevant temperature raise (38–39°C).^{59,85} In this temperature range it is possible to observe a reversible disruption of the barrier on the surface of the brain. To verify if the heat induced by our MNPs under AMF was able to increase the BBB's permeability we have focused on our cubic shaped NPs of size below 15 nm. Their magnetic properties should permit to reach the target temperature (40 °C, a little higher than the one reported above to ensure the correct local temperature) as fast as possible and maintain that temperature for the entire duration of the MHT (30 min same time used by *tabatabei et al.*). Moreover, it was desirable to achieve this heat performance using the smallest MNPs dose possible. As a first check, the heat performance of IONCs and CoFeNCs were compared in complete biological media. These tests

were done using a fixed frequency of 120 kHz, varying the applied field and the concentration of the NCs to attain the requested performance. The CoFeNCs (13nm in cube edge) at a concentration of 2 g_(Co+Fe)/L (345 nM) reached the best results. They could heat up to 40 °C in 300 s under an applied field of only 20 kA/m (Figure 11b). The IONCs (15 nm) at a concentration of 3 g/L (436 nM) reached the target temperature after 1500 s applying a field of 32 kA/m (Figure 11a). Therefore, CoFeNCs having reached the same temperature at the same fixed frequency but at lower field intensity were chosen for the following experiments on the BBB model.

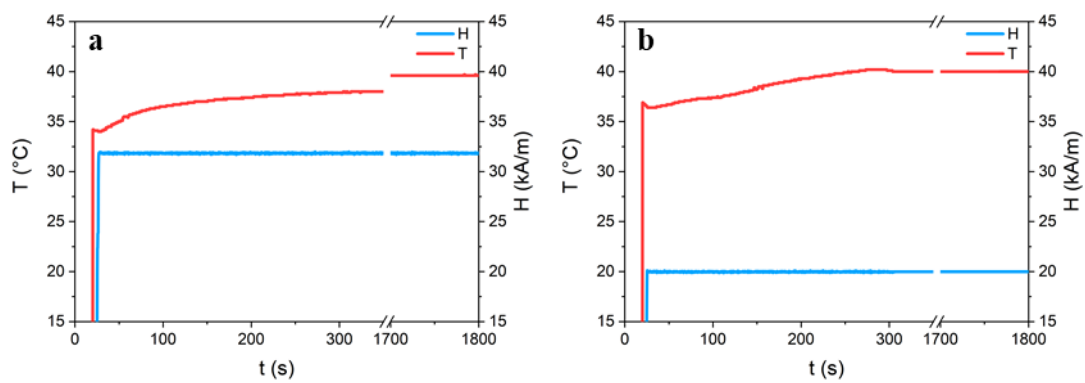


Figure 11 The heat performance of **a)** IONCs and **b)** CoFeNCs were compared in complete biological media. Test done using a fixed frequency of 120 kHz, varying the applied field. CoFeNCs (13nm in cube edge) at a concentration of 2 g_(Co+Fe)/L could heat up to 40 C in 300s under an applied field of only 20 kA/m. The IONCs (15 nm) at a concentration of 3 g/L reached the target temperature after 1500 s applying a field of 32 kA/m. Therefore, CoFeNCs having reached the same temperature at the same fixed frequency but at lower field intensity were chosen for the following experiments on the BBB model.

2.2.7 NPs passage across the BBB.

Before performing the experiment to assess the permeability of the BBB model to our NPs under MHT, the stability of CoFeNCs coated with PMAO-PEG were tested in supplemented cell media by measuring the DLS hydrodynamic diameter of the NPs over an incubation time of 48 hours at 37 °C. The hydrodynamic size of the sample, measured by DLS did not change during the two days of test (Figure 12a) and there was no visible NPs aggregation or sedimentation as shown by Figure 12b. In which it was not visible sign of color change looking to the bottom of the cuvettes and no change in media transparency.

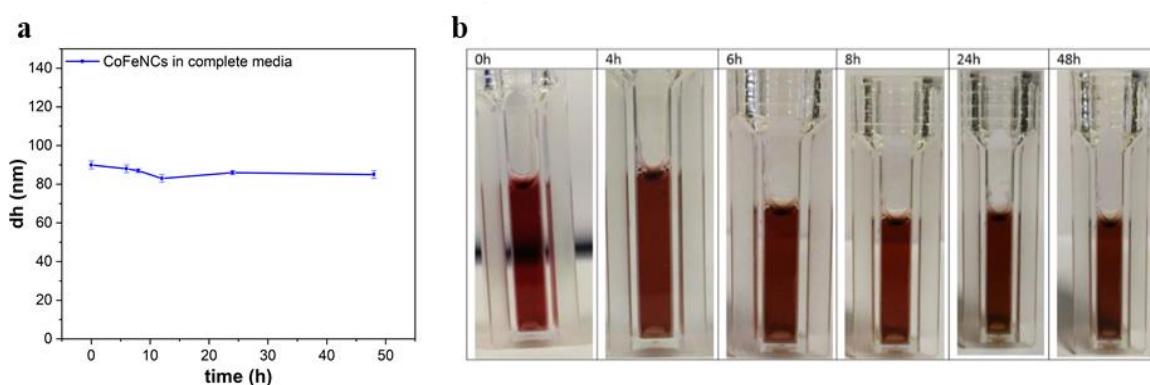


Figure 12 a) Hydrodynamic diameter (intensity average) monitoring study of CoFeNCs PMAO-PEG in biological medium in the presence of 10% FBS, over a total incubation period of **b)** 48h and picture of the cuvette taken at the same time point.

The barrier in presence of the MNPs was exposed to two cycles of MHT (30 min each). Since the thermal stimuli brakes the proteins that form the TJ between cells, 20 – 24 h were waited between the two treatments to allow the cells to recover from the temporary damage. As a control for the model used in the study, the passive passage (PP) of the MNCs was evaluated in comparison to the one subjected to thermal treatment. The passage of the MNPs through the BBB was quantified by elemental analysis. The development of a suitable protocol was required, in a first stage of this study, to understand which were the proper conditions to physically perform the experiments ensuring the right test conditions. Thus, a custom-made support for the Transwell was produced, allowing inserting each well individually inside the magnetic hyperthermia device and positioning them precisely in the center of the magnetic field. The use of single wells supports reduced also the risk of contamination and cross-contamination. The concentration of NPs used for the experiments was precisely tuned to

increase the temperature, under AMF, to 39 - 40°C and not higher, in order to avoid cellular damage and membrane breakage.

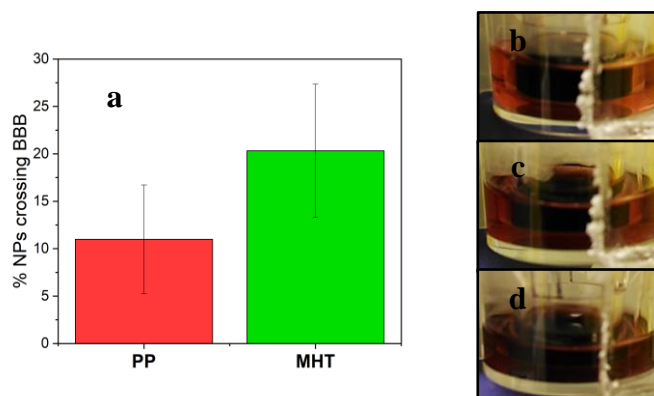


Figure 13 CoFeNCs PMAO-PEG transportation across BBB, in terms of **a**) transportation percentage of nanoparticles in case of passive passage (PP) and MHT treatment (MHT), evaluated measuring the amount of iron in the basolateral chamber by ICP after 48 hours of incubation with 2 g_(Co+Fe)/L of CoFeNCs-PMAO-PEG. Images of custom made Transwell support, from up to down: **b**)CTRL, **c**) PP test sample and **d**) MHT test sample. It is visible how the basolateral media became darker after the MHT.

The results revealed the efficacy of the MHT, which increases the NCs passage across the BBB more than two times comparing to the passive one (Figure 13a). The difference in the amount of NCs passage can be also seen by inspecting and comparing the color difference of the media in the basolateral chamber (Figure 13b-d). The chamber treated with hyperthermia shows a darker media with respect to the PP due to the higher content in NCs. The same outcome was observed from the measure of the amount of iron found in the basolateral chamber for the passive and the MHT Transwell. The increased permeability of the endothelial cells when exposed the thermal treatment was clearly confirmed (Figure 14a). These results are consistent with the ones reported in literature for the BBB passage of large dye molecules boosted by MHT.⁶¹ Moreover, there was a significant difference in the amount of iron found in the membranes and the cells layers by elemental analysis, after the digestion. The Fe content was four times higher in the samples exposed to hyperthermia than those used for the PP (Figure 14b).

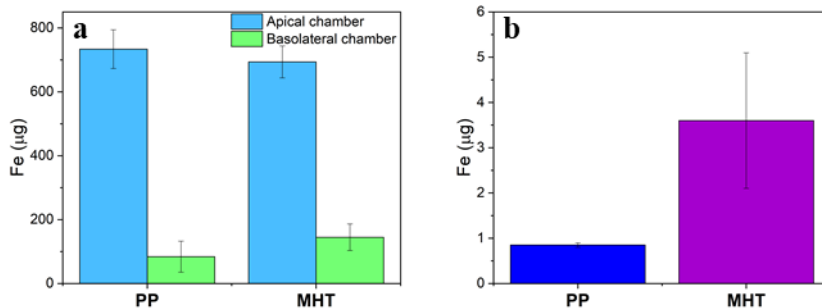


Figure 14 CoFeNCs PMAO-PEG transportation across BBB, in terms of passive passage (PP) and MHT treatment, evaluated by ICP after 48 hours of incubation with 2 g_(Co+Fe)/L of CoFeNCs. **a)** comparison between the Fe content found in the apical and in the basolateral chamber. **b)** Fe content found in the BBB layer composed by the cell layer, the collagen layer and the polyester membrane.

This also indicates the enhanced permeability of the barrier promoted by the thermal treatment. We have also confirmed this result by using transmission electron microscopy and identifying the presence of the MNCs inside the layer composed by cells, collagen and polymeric membrane that eventually are trapped in the collagen layer, or into the membrane or perhaps internalized by the endothelial cells. Thus, after the experiments were completed, the barriers were fixed in a resin matrix, cut and analyzed by TEM (Figure 15). Interestingly, it was found that mostly only the para-cellular passage was occurring, and only few NPs were found inside cells. The majority of the NCs were located into the collagen layer and inside the Transwell membrane (Figure 15a), issue that could occur with this type of BBB model.⁸⁶ In this way, was possible to ascribe the increase of iron only to promote NP permeability driven by the MHT.

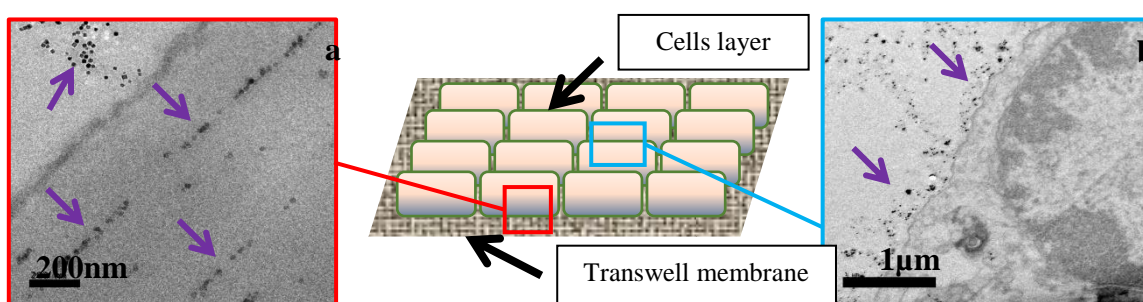


Figure 15 TEM images of **a)** the collagen/ membrane layer and **b)** of the cell layer of CoFeNCs PMAO-PEG across BBB, taken after 48h and 2 cycle of MHT(30 min each) The purple arrows indicate the location of the NCs. In image **a)** the NCs are trapped into the collagen and in the pores of the polymeric membrane. In image **b)** the NCs are located on top of the cell and none are visible inside.

2.2.8 Evaluation of BBB recovery

To evaluate the recovery of the cell barrier upon exposure to heat generated by the NCs under the MHT, the measure of the “tightness” of the BBB model was determined based on the flux of a fluorescent molecule of known molecular weight across the barrier, measured by the change in fluorescence of the media on the basolateral chambers.⁸⁶ Thus, soon after the MHT experiments the permeability of the BBB to a fluorescent dye (FD-4kDa) was studied. This assay was required to understand if the barrier damages caused by the temperature increase during MHT were recovered after treatment. This is considered a standard procedure to evaluate the status of the barrier before and after the exposure to a specific drug.^{87,88} The results showed a significant reduction of dye passage through the cell layer. No significant difference in amount of dye was measured in the basolateral chamber between MHT, PP and the not treated control (Figure 16), meaning that the BBB functions were preserved. Moreover, since the assays were carried out one hour after the last cycle of hyperthermia treatment, was proved that the recovery happens relatively fast.

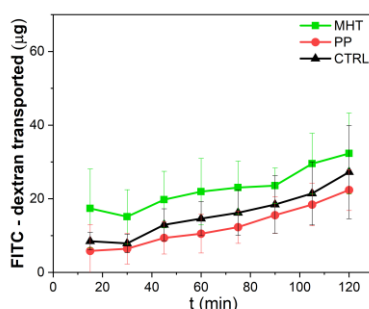


Figure 16 FD4 assay graphs: control, passive passage and magnetic hyperthermia treatment enhanced passage of CoFeNCs after two cycle of hyperthermia, 9 days after cells seeding. No significant difference were visible between the three conditions, proving that the recovery from the heat damage happens relatively fast.

2.2.9 Insulin fibrils degradation by Ferulic acid

Since the final goal of this study is the treatment and disruption of the peptide plaques, common in many neurodegenerative diseases, the effect of Ferulic Acid (FA) on insulin fibrils was studied. Indeed the final aim it would have been to associate the FA to the NCs surface thus enabling the delivery MHT mediated. As a first preliminary aim, FA was chosen as disaggregating agent for insulin fibrils, prepared by Prof. Annalisa Relini. These were chosen as model system being easier to handle than amyloid fibrils and, at the same time, show a similar behavior to amyloid fibrils.⁸⁹ To perform this test, the insulin fibrils were incubated at 37 °C for 24 and 72 hours with FA. The FA was tested at different concentrations from 14 μM to 56 μM , to investigate which was the correct amount of compound that effectively disaggregate the fibrils. The results of these preliminary tests seemed promising. Looking at the TEM images of the insulin fibers, acquired after 24 and 72 h, a reduction in length and volume of them is visible (Figure 17 Fibril + FA 28-56 μM). In particular, the insulin fibril degradation starts to be visible after 72 h exposure to 28 μM of FA, but doubling the FA concentration to 56 μM the effect was occurring already after 24 h. Hence, the fiber reduction was found to be more pronounced increasing the FA concentration. These results are reproducing the data collected and published by the work of *Jayamani and colleagues*. Indeed in their work, the author found that FA can inhibit insulin fibril formation in vitro, and the efficiency of the compound is concentration dependent: reduces at lower concentration and inhibits at higher concentrations.⁸⁹ Interestingly, they also showed results confirming that FA protects the native structure of insulin and thereby prevents the conformational changes required for amyloid fibrils formation.⁸⁹

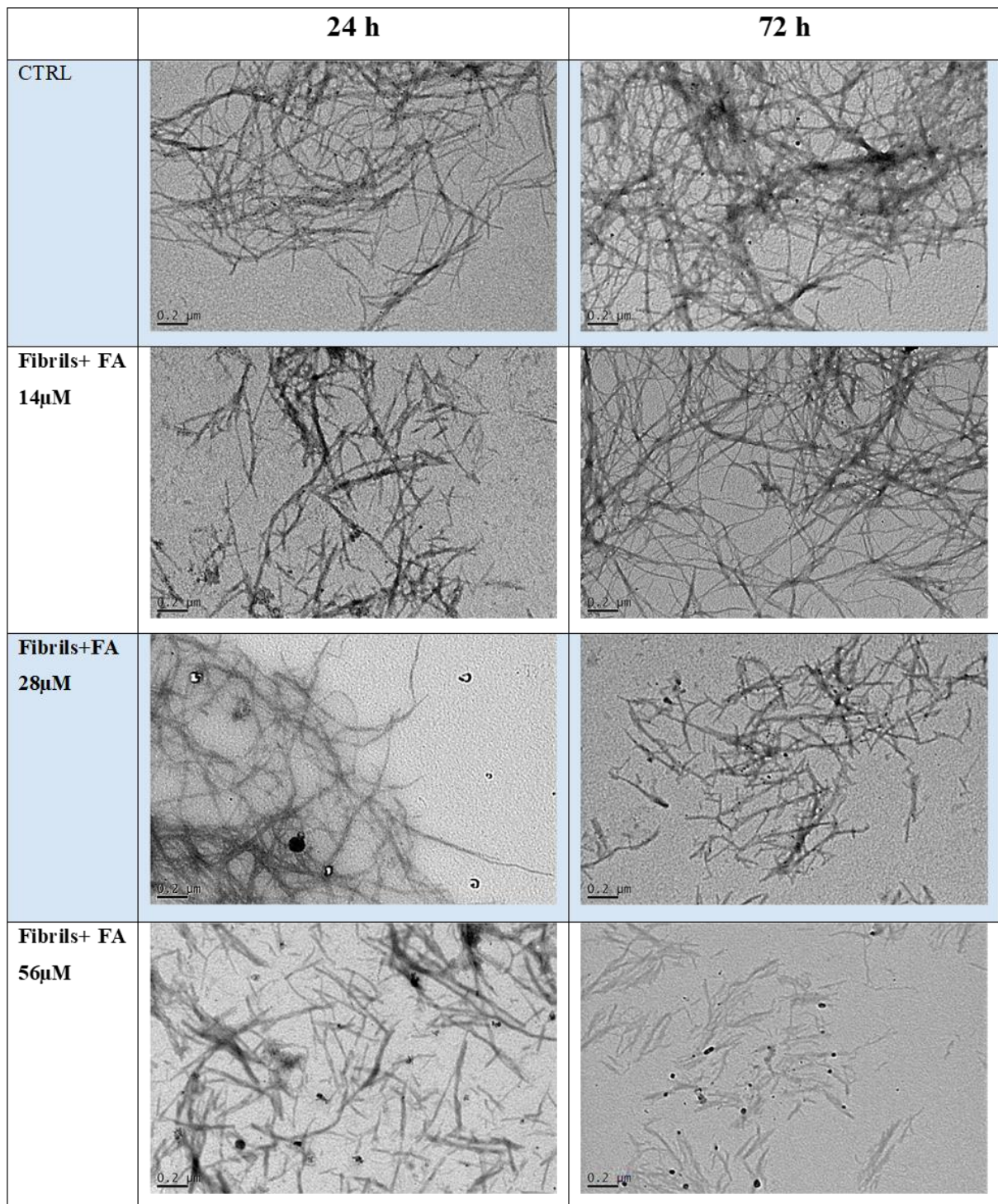


Figure 17 Insulin fibril disaggregation by Ferulic Acid. Here are visible the TEM images of insulin fibril (100 μM) treated with different amount of Ferulic Acid (0-14-28-56 μM) after 24 and 72 hours of incubation at 37°C.

2.3 Conclusion and outlook

In this chapter, the results collected to implement a functional *in-vitro* model of BBB suitable for permeability studies are reported. Using our nanocubes, the possibility to increase the MNPs transportation through BBB using heat as the trigger stimulus to open the TJs without damaging permanently the barrier was proved. To achieve this result was first investigated the proper coating for the NPs, revealing that the functionalization with PEG enhanced the stability in biological media and the BBB passive transportation of the MNPs. Then a comparison of the heating performances in biological media between IONCs and CoFeNCs was done. The Cobalt ferrite NCs were chosen thanks to their outstanding heating performances and so the possibility to reduce their dose. Moreover, the NCs were successfully functionalized with TAT peptide. This could enhance the BBB passage taking advantage of the trans-cellular pathway in combination with the MHT; this strategy will be further exploited. Finally, a promising method to break up peptide plaques using FA was reported. The insulin fibers showed a sensible reduction in length and volume when incubated with FA. Furthermore, the FA efficacy on peptide fibers showed a strong dependence to its concentration, which increases with the increase of compound's dose. The work could be carried on, finding the proper strategy to deliver the FA to the brain. A promising way could be loading the compound on MNPs coated with a thermo-responsive polymer, studying its release ability under hyperthermia. Moreover, the effect of FA on Amyloid- β aggregates has to be studied. The final goal will be to merge all these puzzle pieces, testing a more complex model of BBB (e.g. adding an astrocytes layer), using the NCs with the best magnetic performances, poly-functionalized to enhance the passage through the barrier and having the right coating to encapsulate and release FA, the disaggregating agent. Then, overcome the BBB, the release of the FA to destabilize the A β aggregated fibrils will be reached. Further studies are also needed to investigate the combined effect on cell of CoFeNCs cytotoxicity and MHT. The use of cobalt ferrite MNCs for brain diseases treatment presents some limitations due to the intrinsic toxicity of the Co ions. This is the reason why in the previous chapter different magnetic materials were prepared. On the other hand, if the cytotoxic cobalt ions can be slowly released, this intrinsic cytotoxicity may be combined with MHT to kill undesirable tumor cells by the synergic toxicity action.

2.4 Experimental section

Synthesis of iron oxide nanocubes

Fe₃O₄ nanocubes (IONCs) were synthesized by thermal decomposition following an established procedure with suitable modifications. The protocol rely on the synthesis of particles of 15 nm in size. In a 100 mL three-neck flask connected to a standard Schlenk line, 1 mmole (353 mg) of Fe(acac)₃ and 5.5 mmoles (950 mg) of decanoic acid were dissolved in a mixture of 10 mL squalane and 15 mL benzyl ether. The resulting solution was degassed at 65 °C for 2 h reaching 16-25 μBar vacuum after 2 h. After switching to N₂ flow, the temperature of the mixture was increased to 200 °C at a rate of 5 °C/min and kept at 200 °C for 1.5 h. Then, the reaction temperature was increased to 305 °C at a rate of 7.5 °C/min keeping the mixture refluxing for 1 h. The flask was than cooled down to room temperature (RT) under inert atmosphere. The black colloidal solution was washed 2 times with excess amount of acetone (45 mL) and centrifuged at 4500 rpm for 20 min to collect the particle as black precipitate. The final particles were dispersed in chloroform (8 mL) for further experiments.

Synthesis of cobalt ferrite nanocubes

Co_xFe_{3-x}O₄ nanocubes (CoFeNCs) were synthesized by thermal decomposition following an established procedure, with suitable modifications. The protocol relies on the synthesis of particles of 17 nm in size with 0.65 Co stoichiometry. In a 100 mL three-neck flask connected to a standard Schlenk line, 0.46 mmoles (115 mg) of Co(acac)₂, 1 mmole (353 mg) of Fe(acac)₃ and 6 mmoles (1033 mg) of decanoic acid were dissolved in a mixture of 12 mL squalane and 13 mL benzyl ether. The resulting deep red solution was degassed at 65 °C for 2 h reaching 16-20 μBar vacuum after 2 h. After switching to N₂ flow (120 bubbles/min in the shlenk's bubbler), the temperature of the mixture was increased to 200 °C at a rate of 5 °C/min and kept at 200 °C for 1.5 h. After, the reaction temperature was increased to 305 °C at a rate of 7.5 °C/min keeping the mixture refluxing for 1 h. The flask was then cooled down to room temperature under inert atmosphere. The black colloidal solution was washed 2 times with excess amount of acetone (45 mL) and centrifuged at 4500 rpm for 20 min to collect the particle as black precipitate. The final particles were dispersed in chloroform (8 mL) for further experiments.

Phase transfer of the NCs in water with poly(maleic anhydride-alt-1-octadecene).

The synthesized, hydrophobic NCs dispersed in chloroform were transferred to water, using poly(maleic anhydride-alt-1-octadecene) (PMAO), following a protocol developed by our group with suitable modifications.^{90,91} NCs of 15 nm in size at a concentration of about 400 nM (were diluted with an excess of chloroform (70 mL) and sonicated for 5 minutes. A certain amount of PMAO polymer solution in chloroform (137 mM, concentration referred to the monomer units) was added, respecting a ratio of 500 molecules of monomer unit per nm² of NC surface. The solvent was evaporated at the Rotavapor (140 rpm, 50 °C) following three steps of evaporation under reduced pressure: 800 mBar for 30 minutes, 700 mBar for 30 minutes and finally 600 mBar until complete solvent evaporation was achieved. The dried sample was then soaked in 20 mL of borate buffer and sonicated at 65 °C for 1 h until complete solubilization was verified. The water soluble NCs were concentrated by an ultrafiltration system. The sample volume was reduced to nearly 3 mL under continuous shaking at 150 rpm for 15 min at RT. Subsequently, the sample was loaded on top of a sucrose gradient (2 mL of 20 %, 3 mL of 40 % and 3 mL of 60 % in an ultra-centrifugal tube, from top to bottom) and centrifuged at 20,000 rpm for 45 min. The excess of polymer (visible under UV lamp) found at the top of the sucrose gradient at 20 % was removed, by collecting it with a syringe. Instead, the nanocubes, usually found in the 40 % to 60 % fraction of the sucrose gradient were collected and further washed with pure water (MilliQ) three times to remove the excess of sucrose and finally concentrated to a final volume of about 4 mL in water.

Poly(ethylene glycol) functionalization

The functionalization of the polymeric shell of nanocubes with poly(ethylene glycol) (PEG) was carried out following a procedure developed in our group, with minor modifications.⁹² A solution of CoFeNCs of 0.1 μM was mixed with the same volume of 0.125 M 1-ethyl-3-(3-dimethylaminopropyl)carbodiimide hydrochloride (EDC) and a diamine-PEG (NH₂-PEG-NH₂) 0.1 mM solution in pure water. The amount of PEG was kept as 1000 fold excess compared to NPs molar concentration. The mixture was vigorously shaken for one minute and left under gently shaking at 150 rpm for 2 h RT. Finally, the solution was diluted 3 times to quench the reaction and washed in pure water using centrifugal filters. The final sample was collected in few microliters of water.

Cell penetrating peptide functionalization

Following a protocol developed in our group,⁶⁶ the modified HIV Transactivating Transcriptional Activator (TAT) peptide was grafted to the surface of the NCs PMAO shell. The Cys-TAT (GYGRKKRRQRRRG-amide) was attached to the PEGylated IONCs and CoFeNCs. With respect to the published protocol, the amount of reagents and the shaking velocity were adapted for the functionalization of NCs. Thus, 500 μ L of a 100 nM solution of NCs were mixed with the same volume of a 50 μ M water solution of Sulfo-SMCC (sulfosuccinimidyl 4-(N-maleimidomethyl)cyclohexane-1-carboxylate). The solution was left under shaking (150 rpm) for 40 minutes at 4°C. At the end of the reaction, the solution was purified from the excess of Sulfo-SMCC using a Sephadex G-25 column and concentrated by centrifugation to 500 μ L. This solution was mixed with 500 μ L of 15 μ M Cys-TAT solution in water and left overnight under gentle agitation (150 rpm) at 4°C. Also in this case the excess of peptide was removed with a Sephadex column and concentrated by centrifugation to the requested volume.

Elemental analysis

Inductively coupled plasma optical emission spectroscopy (ICP-OES) analysis was performed on an iCAP 6000 spectrometer (ThermoScientific) to quantify the concentration of the elements of interest. Briefly, 25 μ L samples were digested in 2.5 mL of aqua regia (HCl:HNO₃ ratio is 3:1 (v/v)) overnight and diluted with 25 mL of milliQ water prior to the measurement.

Transmission electron microscopy

Transmission electron microscopy (TEM) was carried out on a JEOL JEM-1011 with an acceleration voltage of 100 kV. The sample preparation was conducted by drop-casting a droplet of the sample solution onto a 400 mesh ultra-thin carbon-coated copper grid with subsequent removal of the solvent by evaporation at RT.

Dynamic Light Scattering and gel electrophoresis

The hydrodynamic size was estimated by using dynamic light scattering (DLS) from Malvern Instruments Zetasizer-nano. The scattered intensity was collected at 173° back scattered geometry with 632 nm laser source. For each sample 3 measurements were taken with 10 acquisitions each. Gel electrophoresis was used to observe the NCs migration in a solid agarose

matrix after the water transfer procedure to confirm the absence of free polymer in solution. The free polymer migrates faster than the NCs and can be detected under a UV light. The electrophoresis was run on 1% agarose gel in tris-borate-EDTA(TBE) buffer applying a voltage of 100 V or 45 minutes.

NPs stability test in media

The stability test in complete biological media of the CoFeNCs-PMAO-PEG was performed. 50 μ L of NCs (3g_{Co+Fe}/L) were diluted in 850 μ L of biological media supplemented with 10% of fetal bovine serum (FBS) in a clear cuvette for DLS. The samples were incubate at 37 °C for the entire duration of the experiment. At time 0-4-6-8-24-48 hours the hydrodynamic diameter was measured by DLS.

Magnetic characterization

Magnetic measurements were performed on a MPMS superconducting quantum interference device (SQUID) from Quantum Design Inc. Hysteresis curves were recorded within the magnetic field of ± 70 kOe at 5 K and 298 K.

Calorimetric measurements of Specific absorption rate

A commercially available magnetic nano-heating device (DM100 Series, nanoscale Biomagnetics) was used to evaluate the SAR values under quasi-adiabatic conditions. The water soluble NCs were exposed to an alternating magnetic field (from 12 up to 32 kA/m) at 3 different frequencies: 105, 220 and 300 kHz. All measurements were performed using 300 μ L of sample in water (at a concentration of 4 g/L) and the SAR values were normalized using the iron concentration determined by elemental analysis (g/L). SAR values were calculated according to the following equation:

$$\text{SAR} \left(\frac{\text{W}}{\text{g}} \right) = \frac{\text{C}}{\text{m}} \cdot \frac{\text{dT}}{\text{dt}}$$

Where C is the specific heat capacity of water (4185 J/kgK) and m is the concentration (g/L) of magnetic material in solution. To calculate the parameter dT/dt, temperature data points collected within the first 60 seconds were used to obtain the slope of the curve deriving from

the linear fitting of these points. Each data point is given as the mean of at least three independent measurements.

In-Vitro model of Blood Brain Barrier

bEnd.3 were seeded at a density of 50000 cells/well on Transwell® filter (1.2 cm² for the 12-well polycarbonate plate with pore size of 3.0 µm), previously coated with type I collagen (0.1 mg/mL) in order to promote cell adhesion and growth as a monolayer. Cells were cultured in an incubator at 37 °C with 5 % CO₂, 95 % air and saturated humidity. The culture medium was changed every two days.^{93 86} Trans-endothelial electrical resistance (TEER) was measured using a Millicell-ERS (Electrical Resistance System). The measurements were done evaluating the electrical resistance of the cells layer using two electrodes: one plunged in the apical compartment and one in the basolateral.

Immunofluorescence staining of tight junction proteins

Immunofluorescence staining assay was performed after 7 days of culturing *in-vitro*. Briefly, cells were washed once with 1× PBS solution, fixed with 4 % paraformaldehyde (PFA) at RT and permeabilized with 0.1 % Triton X-100 in PBS for 5 min. In order to prevent non-specific binding, a blocking solution of PBS containing 0.05 % Tween 20 and 2 % BSA was added for 30 min. Primary antibodies rabbit anti-Claudin-5 or VE-Cadherin (Millipore, Billerica, MA, USA) diluted 1:200 in blocking solution were used and incubated for 45 minutes at RT. After, the samples were washed 3 times in PBS and incubated with secondary antibodies Alexa 568 and Alexa 488 for 45 minutes at RT.⁹⁴⁹⁵ The cells nuclei were labeled with DAPI using prolong anti-fade reagent and the fluorescence microscopy imaging was carried out using a Nikon Eclipse E4000 (Nikon Instruments Inc., USA). Photographic images were visualized by NIS Elements Viewer (Nikon Instruments Inc., USA).

NPs passage across the BBB

NPs passage assay

bEnd.3 monolayers were used for migration assays 7–10 day's post-transwell seeding. the following protocol was set: 500 µL of DMEM medium was poured onto the transwell apical compartment containing IONCs-PMAO-PEG (3 g/L) or CoFeNCs-PMAO-PEG (2 g/L), respectively. while the basolateral compartment contained 1500 µL of medium. The passive

passage of the NPs was evaluated after 24 h of incubation at 37°C by elemental analysis. At the same time the enhanced passage due to the application of Hyperthermia treatment was evaluated. The thermal treatment was repeated two times after 1 and 23 hours of incubation with the NCs. The two cycles of 30 min each were carried out using a commercially available magnetic nano-heating device (DM3 Series, nanoscale Biomagnetics). The treatments were done using an alternating magnetic field under the allowed biological limit (frequency 110 kHz, field 20-30 kA/m). For both assays the passage was quantified by ICP, measuring the apical media, the basolateral and the cell layer which were collected separately. All the fractions were digested as explained below in the ICP analysis part.

Dye permeability study

At the end of the transport assay the chambers were rinsed with fresh media and the integrity of the BBBs as well as the permeability were evaluated. In case of fluorescein isothiocyanate–dextran (FD-4 kDa) assay 100 µL of medium was removed from each basolateral compartment every hour, in case of FD-4 kDa and divided in aliquots onto black flat-bottomed 96-well plates and replaced with fresh medium.⁸⁶ The fluorescence of FD-4 kDa was determined using a plate reader spectrofluorimeter with an excitation/emission wavelength of 490/515 nm.

Internalization study

For quantifying the amount of iron internalized by the cells, the bEnd3 cells seeded on the transwell membrane were rinsed with phosphate-buffered saline and detached using trypsin. Cells were collected by centrifugation (1000 rpm for 4 minutes). Iron content was determined via ICP. For that purpose, after treatment with the NPs the cells were digested in a solution of hydrogen peroxide (500 µL) and nitric acid (300 µL) for 5 h, sonicating the mixture at 65 °C to dissolve the organic matrix. Soon after, 900 µL of hydrochloric acid were added to the solution and left overnight to digest the remaining nanoparticles.

Insulin fibrils degradation by Ferulic acid

The insulin fibrils were produced by Prof. A. Relini from the University of Genova. To obtain a solution of 5 mM of Ferulic Acid (FA), 30 mg of the natural compound were dissolved in 30 mL of PBS with 40 µL of 2 M NaOH and then sonicated for a few minutes. For the degradation study 100 µL of Insulin fibrils in PBS (100 µM) were incubated with 100 µL of

FA at different concentrations (from 14 μM to 56 μM). The samples were incubated at 37 $^{\circ}\text{C}$ for 72 hours. After 24 and 72 hours the solutions were observed qualitatively at TEM.

2.5 References

1. Cruts, M., Theuns, J. & Van Broeckhoven, C. Locus-specific mutation databases for neurodegenerative brain diseases. *Hum. Mutat.* **33**, 1340–1344 (2012).
2. Re, F., Gregori, M. & Masserini, M. Nanotechnology for neurodegenerative disorders. *Maturitas* **73**, 45–51 (2012).
3. Saba, L. *Imaging in neurodegenerative disorders*.
4. Schain, M. & Kreisl, W. C. Neuroinflammation in Neurodegenerative Disorders—a Review. *Curr. Neurol. Neurosci. Rep.* **17**, 25 (2017).
5. Bozyczko-Coyne, D. & Williams, M. Neurodegeneration. *Compr. Med. Chem. II* 193–228 (2007). doi:10.1016/B0-08-045044-X/00168-1
6. Farrer, M. J. Genetics of Parkinson disease: paradigm shifts and future prospects. *Nat. Rev. Genet.* **7**, 306–318 (2006).
7. Goedert, M. & Spillantini, M. G. REVIEWS A Century of Alzheimer ' s Disease. *Science (80-.)*. **314**, 777–781 (2006).
8. Selkoe, D. J. Alzheimer's Disease: Genes, Proteins, and Therapy. *Physiol. Rev.* **81**, 741–766 (2001).
9. Bertram, L. & Tanzi, R. E. The genetic epidemiology of neurodegenerative disease. *J. Clin. Invest.* **115**, 1449–57 (2005).
10. Isacson, O., Seo, H., Lin, L., Albeck, D. & Granholm, A.-C. Alzheimer's disease and Down's syndrome: roles of APP, trophic factors and ACh. *Trends Neurosci.* **25**, 79–84 (2002).
11. Lai, F. & Williams, R. S. A Prospective Study of Alzheimer Disease in Down Syndrome. *Arch. Neurol.* **46**, 849–853 (1989).
12. Glenner, G. G. & Wong, C. W. Alzheimer's disease and Down's syndrome: Sharing of a unique cerebrovascular amyloid fibril protein. *Biochem. Biophys. Res. Commun.* **122**, 1131–1135 (1984).
13. Alzheimer's disease: Initial report of the purification and characterization of a novel cerebrovascular amyloid protein. *Biochem. Biophys. Res. Commun.* **120**, 885–890 (1984).
14. Kang, J. *et al.* The precursor of Alzheimer's disease amyloid A4 protein resembles a cell-surface receptor. *Nature* **325**, 733–736 (1987).
15. Masters, C. L. *et al.* Amyloid plaque core protein in Alzheimer disease and Down syndrome. *Proc. Natl. Acad. Sci. U. S. A.* **82**, 4245–9 (1985).

16. Iwatsubo, T. *et al.* Visualization of A β 42(43) and A β 40 in senile plaques with end-specific A β monoclonals: Evidence that an initially deposited species is A β 42(43). *Neuron* **13**, 45–53 (1994).
17. Ermak, G. & Davies, K. J. . Calcium and oxidative stress: from cell signaling to cell death. *Mol. Immunol.* **38**, 713–721 (2002).
18. LaFerla, F. M. Calcium dyshomeostasis and intracellular signalling in alzheimer’s disease. *Nat. Rev. Neurosci.* **3**, 862–872 (2002).
19. Gibson, G. E. Interactions of oxidative stress with cellular calcium dynamics and glucose metabolism in Alzheimer’s disease,. *Free Radic. Biol. Med.* **32**, 1061–1070 (2002).
20. Mattson, M. P. & Chan, S. L. Neuronal and glial calcium signaling in Alzheimer’s disease. *Cell Calcium* **34**, 385–397 (2003).
21. Barnham, K. J., Masters, C. L. & Bush, A. I. Neurodegenerative diseases and oxidative stress. *Nat. Rev. Drug Discov.* **3**, 205–214 (2004).
22. Kanegawa, N. *et al.* In vivo evidence of a functional association between immune cells in blood and brain in healthy human subjects. *Brain. Behav. Immun.* **54**, 149–157 (2016).
23. Perry, V. H. & Holmes, C. Microglial priming in neurodegenerative disease. *Nat. Rev. Neurol.* **10**, 217–224 (2014).
24. Stephenson, J., Nutma, E., van der Valk, P. & Amor, S. Inflammation in CNS neurodegenerative diseases. *Immunology* **154**, 204–219 (2018).
25. Abbott, N. J., Patabendige, A. A. K., Dolman, D. E. M., Yusof, S. R. & Begley, D. J. Structure and function of the blood–brain barrier. *Neurobiol. Dis.* **37**, 13–25 (2010).
26. Mooradian, A. D. Effect of aging on the blood-brain barrier. *Neurobiol. Aging* **9**, 31–39 (1988).
27. Gorié, N., Van Cauwenberghe, C., Libert, C. & Vandembroucke, R. E. The effect of aging on brain barriers and the consequences for Alzheimer’s disease development. *Mamm. Genome* **27**, 407–420 (2016).
28. Ronaldson, P. T. & Davis, T. P. Targeting blood-brain barrier changes during inflammatory pain: An opportunity for optimizing CNS drug delivery. *Ther. Deliv.* **2**, 1015–1041 (2011).
29. Reese, T. S. & Karnovsky, M. J. Fine structural localization of a blood-brain barrier to exogenous peroxidase. *J. Cell Biol.* **34**, 207–17 (1967).
30. Abbott, N. J., Rönnbäck, L. & Hansson, E. Astrocyte–endothelial interactions at the blood–brain barrier. *Nat. Rev. Neurosci.* **7**, 41–53 (2006).

31. Wolburg, H. & Lippoldt, A. Tight junctions of the blood–brain barrier: development, composition and regulation. *Vascul. Pharmacol.* **38**, 323–337 (2002).
32. Hawkins, B. T. & Davis, T. P. The blood-brain barrier/neurovascular unit in health and disease. *Pharmacol. Rev.* **57**, 173–85 (2005).
33. Ballabh, P., Braun, A. & Nedergaard, M. The blood–brain barrier: an overview: Structure, regulation, and clinical implications. *Neurobiol. Dis.* **16**, 1–13 (2004).
34. Kniesel, U. & Wolburg, H. Tight Junctions of the Blood–Brain Barrier. *Cell. Mol. Neurobiol.* **20**, 57–76 (2000).
35. Grieb, P., Forster, R. E., Strome, D., Goodwin, C. W. & Pape, P. C. O₂ exchange between blood and brain tissues studied with ¹⁸O₂ indicator-dilution technique. *J. Appl. Physiol.* **58**, 1929–41 (1985).
36. Zhang, Y. & Pardridge, W. M. Rapid transferrin efflux from brain to blood across the blood-brain barrier. *J. Neurochem.* **76**, 1597–1600 (2001).
37. Triguero, D., Buciak, J. & Pardridge, W. M. Capillary Depletion Method for Quantification of Blood?Brain Barrier Transport of Circulating Peptides and Plasma Proteins. *J. Neurochem.* **54**, 1882–1888 (1990).
38. Cefalu, W. T. & Pardridge, W. M. Restrictive Transport of a Lipid-Soluble Peptide (Cyclosporin) Through the Blood?Brain Barrier. *J. Neurochem.* **45**, 1954–1956 (1985).
39. Masserini, M. Nanoparticles for Brain Drug Delivery. *ISRN Biochem.* **2013**, 1–8 (2013).
40. Berry, C. C. & Curtis, A. S. G. Functionalisation of magnetic nanoparticles for applications in biomedicine. *J. Phys. D. Appl. Phys.* **36**, R198–R206 (2003).
41. Chen, Y. & Liu, L. Modern methods for delivery of drugs across the blood-brain barrier. *Adv. Drug Deliv. Rev.* **64**, 640–665 (2012).
42. Re, F., Gregori, M. & Masserini, M. Nanotechnology for neurodegenerative disorders. *Nanomedicine Nanotechnology, Biol. Med.* **8**, S51–S58 (2012).
43. Lockman, P. R., Mumper, R. J., Khan, M. A. & Allen, D. D. Nanoparticle Technology for Drug Delivery Across the Blood-Brain Barrier. *Drug Dev. Ind. Pharm.* **28**, 1–13 (2002).
44. Tiwari, G. *et al.* Drug delivery systems: An updated review. *Int. J. Pharm. Investig.* **2**, 2–11 (2012).
45. Gupta, A. K. & Gupta, M. Synthesis and surface engineering of iron oxide nanoparticles for biomedical applications. *Biomaterials* **26**, 3995–4021 (2005).

46. Sharifi, I., Shokrollahi, H. & Amiri, S. Ferrite-based magnetic nanofluids used in hyperthermia applications. *J. Magn. Magn. Mater.* **324**, 903–915 (2012).
47. Josephson Lee, Lewis Jerome, Jacobs Paula, Hahn Peter, S. D. The effect of iron oxides on proton relaxivity. *Magn. Reson. Imaging* **6**, 647–653 (1988).
48. Bauer, L. M., Situ, S. F., Griswold, M. A. & Samia, A. C. S. High-performance iron oxide nanoparticles for magnetic particle imaging-guided hyperthermia (hMPI). *Nanoscale* **8**, 12162–12169 (2016).
49. Mourtas, S. *et al.* Curcumin-decorated nanoliposomes with very high affinity for amyloid- β 1-42 peptide. *Biomaterials* **32**, 1635–1645 (2011).
50. Gobbi, M. *et al.* Lipid-based nanoparticles with high binding affinity for amyloid- β 1-42 peptide. *Biomaterials* **31**, 6519–6529 (2010).
51. Srinivasan, M., Sudheer, A. R. & Menon, V. P. Ferulic Acid: Therapeutic Potential Through Its Antioxidant Property. *J. Clin. Biochem. Nutr.* **40**, 92–100 (2007).
52. Picone, P. *et al.* Ferulic acid inhibits oxidative stress and cell death induced by Ab oligomers: Improved delivery by solid lipid nanoparticles. *Free Radic. Res.* **43**, 1133–1145 (2009).
53. Skaat, H., Sorci, M., Belfort, G. & Margel, S. Effect of maghemite nanoparticles on insulin amyloid fibril formation: Selective labeling, kinetics, and fibril removal by a magnetic field. *J. Biomed. Mater. Res. Part A* **91A**, 342–351 (2009).
54. Venkitaramani, D. V *et al.* Beta-amyloid modulation of synaptic transmission and plasticity. *J. Neurosci.* **27**, 11832–7 (2007).
55. Palop, J. J. *et al.* Aberrant Excitatory Neuronal Activity and Compensatory Remodeling of Inhibitory Hippocampal Circuits in Mouse Models of Alzheimer’s Disease. *Neuron* **55**, 697–711 (2007).
56. Chen, R., Romero, G., Christiansen, M. G., Mohr, A. & Anikeeva, P. Wireless magnetothermal deep brain stimulation. *Science (80-)*. (2015).
57. Bellavance, M.-A., Blanchette, M. & Fortin, D. Recent Advances in Blood–Brain Barrier Disruption as a CNS Delivery Strategy. *AAPS J.* **10**, 166–177 (2008).
58. Pardridge, W. M. Drug Transport across the Blood–Brain Barrier. *J. Cereb. Blood Flow Metab.* **32**, 1959–1972 (2012).
59. Dokladny, K., Moseley, P. L. & Ma, T. Y. Physiologically relevant increase in temperature causes an increase in intestinal epithelial tight junction permeability. *Am. J. Physiol. Liver Physiol.* **290**, G204–G212 (2006).

60. Kiyatkin, E. A. & Sharma, H. S. Permeability of the blood–brain barrier depends on brain temperature. *Neuroscience* **161**, 926–939 (2009).
61. Tabatabaei, S. N., Girouard, H., Carret, A.-S. & Martel, S. Remote control of the permeability of the blood–brain barrier by magnetic heating of nanoparticles: A proof of concept for brain drug delivery. *J. Control. Release* **206**, 49–57 (2015).
62. Bhaskar, S. *et al.* Multifunctional Nanocarriers for diagnostics, drug delivery and targeted treatment across blood-brain barrier: perspectives on tracking and neuroimaging. *Part. Fibre Toxicol.* **7**, 3 (2010).
63. Weiss, J. M., Nath, A., Major, E. O. & Berman, J. W. HIV-1 Tat Induces Monocyte Chemoattractant Protein-1-Mediated Monocyte Transmigration Across a Model of the Human Blood-Brain Barrier and Up-Regulates CCR5 Expression on Human Monocytes. (2018).
64. Sancini, G. *et al.* Functionalization with TAT-Peptide Enhances Blood-Brain Barrier Crossing In vitro of Nanoliposomes Carrying a Curcumin-Derivative to Bind Amyloid-B Peptide. *J. Nanomed. Nanotechnol.* **04**, 1–8 (2013).
65. Gupta, A. K. & Gupta, M. Synthesis and surface engineering of iron oxide nanoparticles for biomedical applications. *Biomaterials* **26**, 3995–4021 (2005).
66. Quarta, A., Curcio, A., Kakwere, H. & Pellegrino, T. Polymer coated inorganic nanoparticles: tailoring the nanocrystal surface for designing nanoprobe with biological implications. *Nanoscale* **4**, 3319 (2012).
67. Chen, M., Yamamuro, S., Farrell, D. & Majetich, S. A. Gold-coated iron nanoparticles for biomedical applications. *J. Appl. Phys.* **93**, 7551–7553 (2003).
68. Santra, S. *et al.* Synthesis and Characterization of Silica-Coated Iron Oxide Nanoparticles in Microemulsion: The Effect of Nonionic Surfactants. (2001). doi:10.1021/LA0008636
69. Materia, M. E. *et al.* Mesoscale Assemblies of Iron Oxide Nanocubes as Heat Mediators and Image Contrast Agents. *Langmuir* **31**, 808–816 (2015).
70. Bigall, N. C. *et al.* Colloidal ordered assemblies in a polymer shell - A novel type of magnetic nanobeads for theranostic applications. *Chem. Mater.* **25**, 1055–1062 (2013).
71. Owens, D. E. & Peppas, N. A. Opsonization, biodistribution, and pharmacokinetics of polymeric nanoparticles. *Int. J. Pharm.* **307**, 93–102 (2006).
72. Jokerst, J. V., Lobovkina, T., Zare, R. N. & Gambhir, S. S. Nanoparticle PEGylation for imaging and therapy. *Nanomedicine* **6**, 715–728 (2011).
73. Otsuka, H., Nagasaki, Y. & Kataoka, K. PEGylated nanoparticles for biological and pharmaceutical applications.

Adv. Drug Deliv. Rev. **64**, 246–255 (2012).

74. Sperling, R. A., Pellegrino, T., Li, J. K., Chang, W. H. & Parak, W. J. Electrophoretic separation of nanoparticles with a discrete number of functional groups. *Adv. Funct. Mater.* **16**, 943–948 (2006).
75. Ming Zhao, *, †, Moritz F. Kircher, †, Lee Josephson, and & Weissleder, R. Differential Conjugation of Tat Peptide to Superparamagnetic Nanoparticles and Its Effect on Cellular Uptake. (2002). doi:10.1021/BC0255236
76. Lewin, M. *et al.* Tat peptide-derivatized magnetic nanoparticles allow in vivo tracking and recovery of progenitor cells. *Nat. Biotechnol.* **18**, 410–414 (2000).
77. Torchilin, V. P. Tat peptide-mediated intracellular delivery of pharmaceutical nanocarriers. *Adv. Drug Deliv. Rev.* **60**, 548–558 (2008).
78. Quarta, A., Curcio, A., Kakwere, H. & Pellegrino, T. Polymer coated inorganic nanoparticles: tailoring the nanocrystal surface for designing nanoprobe with biological implications. *Nanoscale* **4**, 3319 (2012).
79. Naik, P. & Cucullo, L. In vitro blood-brain barrier models: Current and perspective technologies. *J. Pharm. Sci.* **101**, 1337–1354 (2012).
80. Mc Carthy, D. J., Malhotra, M., O'Mahony, A. M., Cryan, J. F. & O'Driscoll, C. M. Nanoparticles and the blood-brain barrier: Advancing from in-vitro models towards therapeutic significance. *Pharm. Res.* **32**, 1161–1185 (2015).
81. Claude, P. & Goodenough, D. A. Fracture faces of zonulae occludentes from "tight" and "leaky" epithelia. *J. Cell Biol.* **58**, 390–400 (1973).
82. Claude, P. Morphological factors influencing transepithelial permeability: A model for the resistance of the Zonula Occludens. *J. Membr. Biol.* **39**, 219–232 (1978).
83. Marcial, M. A., Carlson, S. L. & Madara, J. L. Partitioning of paracellular conductance along the ileal crypt-villus axis: A hypothesis based on structural analysis with detailed consideration of tight junction structure-function relationships. *J. Membr. Biol.* **80**, 59–70 (1984).
84. Leyva-Gómez, G. *et al.* Nanoparticle technology for treatment of Parkinson's disease: the role of surface phenomena in reaching the brain. *Drug Discov. Today* **20**, 824–837 (2015).
85. Kiyatkin, E. A. & Sharma, H. S. Permeability of the blood-brain barrier depends on brain temperature. *Neuroscience* **161**, 926–939 (2009).
86. Ragnai, M. N. *et al.* Internal benchmarking of a human blood-brain barrier cell model for screening of nanoparticle uptake and transcytosis. *Eur. J. Pharm. Biopharm.* **77**, 360–367 (2011).
87. Nagpal, K., Singh, S. K. & Mishra, D. N. Drug targeting to brain : a systematic approach to study the factors ,

- parameters and approaches for prediction of permeability of drugs across BBB. 1–29 (2013).
88. Gaillard, P. J. & Boer, A. G. De. Relationship between permeability status of the blood – brain barrier and in vitro permeability coefficient of a drug. **12**, 95–102 (2000).
 89. Jayamani, J., Shanmugam, G., Ramaprasad, E. & Singam, A. Inhibition of insulin amyloid fibril formation by ferulic acid, a natural compound found in many vegetables and fruits. *RSC Adv.* **4**, 62326–62336 (2014).
 90. Di Corato, R. *et al.* Water solubilization of hydrophobic nanocrystals by means of poly(maleic anhydride-alt-1-octadecene). *Journal of Materials Chemistry* **18**, 1991 (2008).
 91. Pellegrino, T. *et al.* Hydrophobic nanocrystals coated with an amphiphilic polymer shell: A general route to water soluble nanocrystals. *Nano Lett.* **4**, 703–707 (2004).
 92. Sperling, R. a., Pellegrino, T., Li, J. K., Chang, W. H. & Parak, W. J. Electrophoretic Separation of Nanoparticles with a Discrete Number of Functional Groups. *Adv. Funct. Mater.* **16**, 943–948 (2006).
 93. Dan, M., Bae, Y., Pittman, T. a. & Yokel, R. a. Alternating Magnetic Field-Induced Hyperthermia Increases Iron Oxide Nanoparticle Cell Association/Uptake and Flux in Blood-Brain Barrier Models. *Pharm. Res.* **32**, 1615–1625 (2015).
 94. Brown, R. C., Morris, A. P. & Neil, R. G. O. Tight junction protein expression and barrier properties of immortalized mouse brain microvessel endothelial cells. **30**, (2006).
 95. Iii, B. M. & Fu, B. M. Permeability of Endothelial and Astrocyte Cocultures: In Vitro Blood–Brain Barrier Models for Drug Delivery Studies. **38**, 2499–2511 (2014).

Appendix

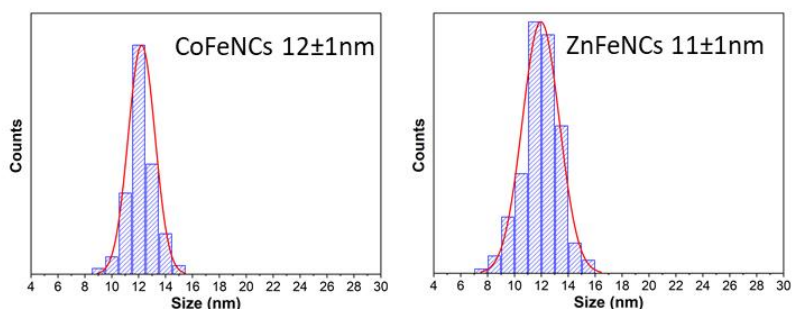


Figure A1 Size distribution of $Co_{0.6}Fe_{2.4}O_4$ and $Zn_{0.18}Fe_{2.82}O_4$, displayed in Figure 9b and Figure 18b of the first chapter, respectively. In particular, these two samples were used for further characterizations.

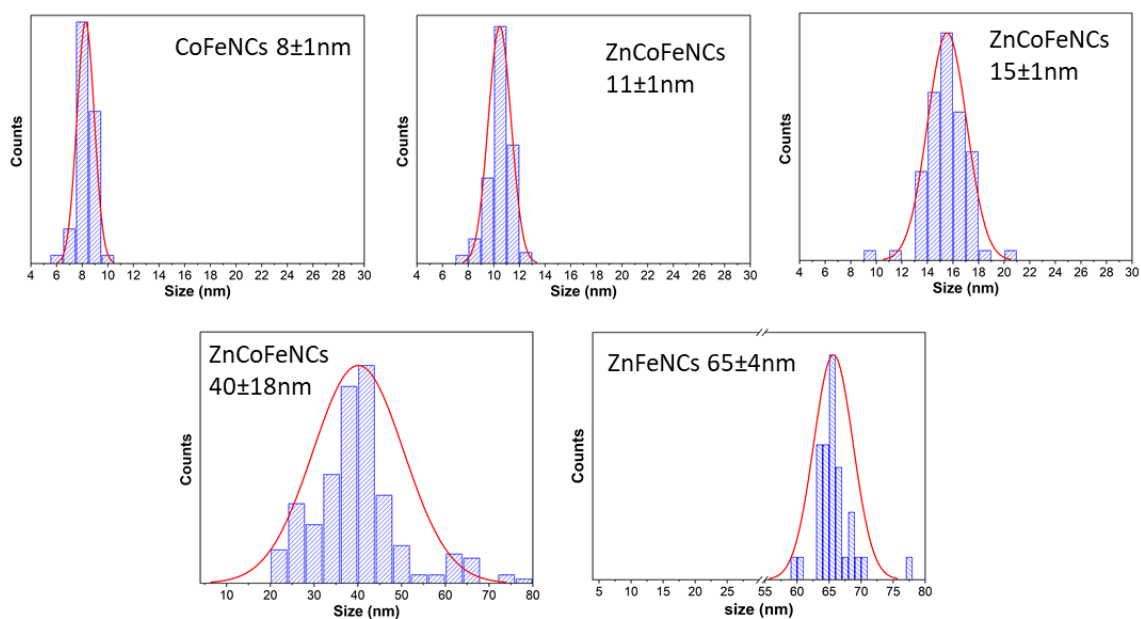


Figure A2 Size distributions of samples in Figure 19 of the first chapter, relative to the synthesis of ZnCoFeNCs varying the Co to Zn feed molar ratios (only Co, 4, 1, 0.25 and only Zn).

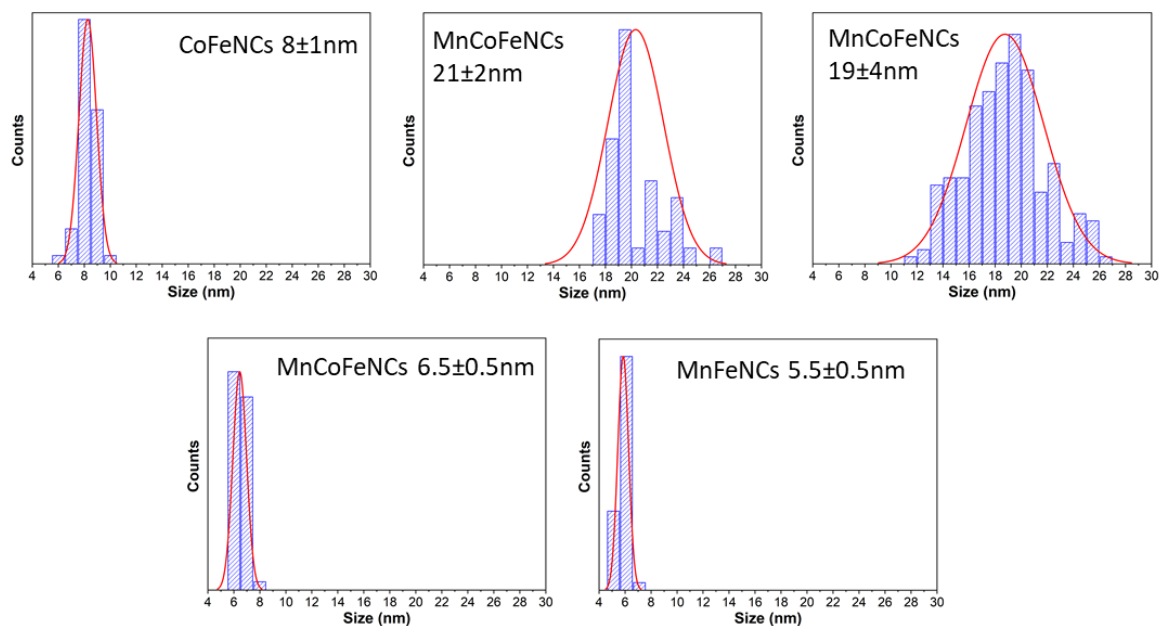


Figure A3 Size distributions of samples in Figure 20 of the first chapter, relative to the synthesis of MnCoFeNCs varying the Co to Mn feed molar ratios (only Co, 4, 1, 0.25 and only Mn).

Table A1 Elemental analysis by EDS of 12 ± 1 nm $Zn_xFe_{3-x}O_4$, 15 ± 2 nm $Zn_xCo_yFe_{3-(x+y)}O_4$, 10 ± 1 nm $Mn_xCo_yFe_{3-(x+y)}O_4$ nanocubes.

| Sample | Element | Atomic % | Error Wt% |
|--|---------|----------|-----------|
| 12 ± 1 nm $Zn_xFe_{3-x}O_4$ | Fe | 95 | 3 |
| | Zn | 5 | 5 |
| 15 ± 2 nm $Zn_xCo_yFe_{3-(x+y)}O_4$ | Fe | 90 | 3 |
| | Co | 7 | 4 |
| | Zn | 3 | 4 |
| 10 ± 1 nm $Mn_xCo_yFe_{3-(x+y)}O_4$ | Fe | 72 | 3 |
| | Co | 22 | 3 |
| | Mn | 6 | 4 |

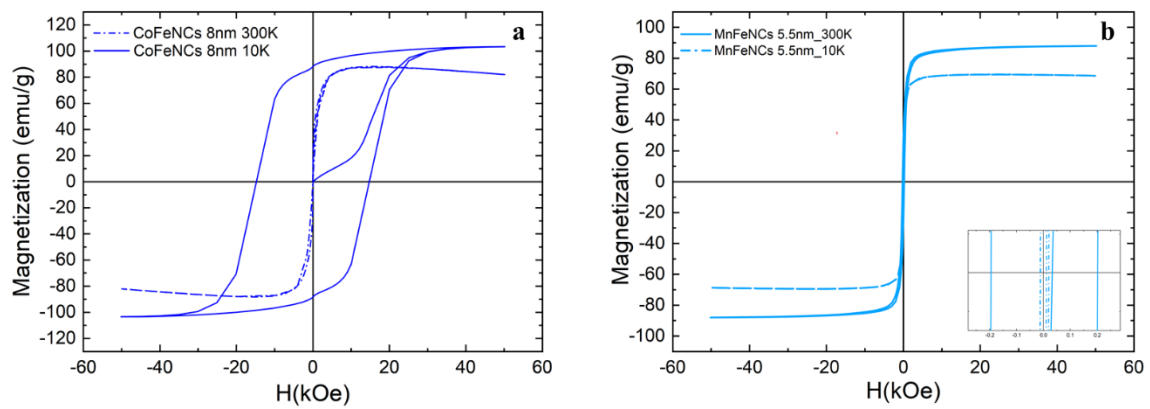


Figure A4 Magnetization vs applied magnetic field curves for different ferrite samples: **a)** $Co_{0.5}Fe_{2.5}O_4$ 8 ± 1 nm and **b)** $Mn_{0.6}Fe_{2.4}O_4$ 5.5 ± 0.5 nm.

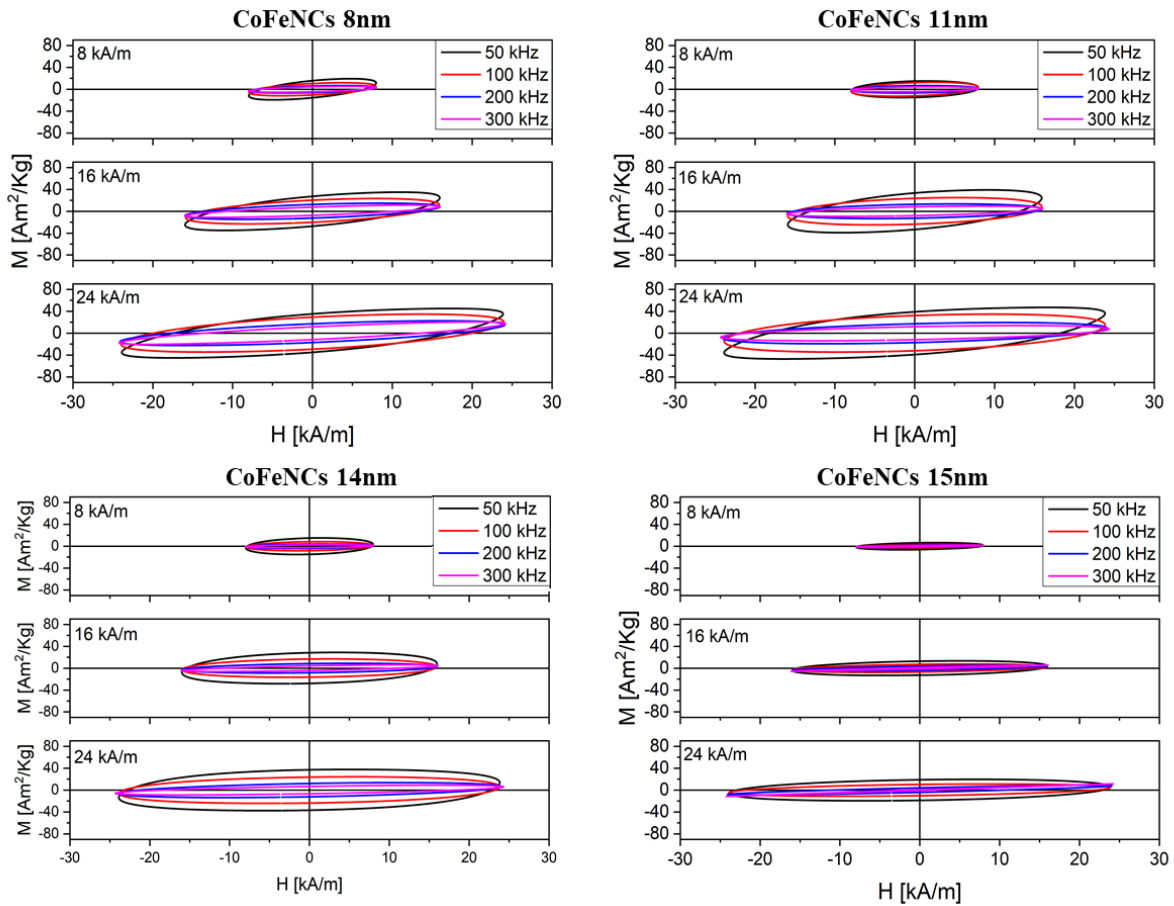


Figure A5 Experimentally measured AC Hysteresis loops for CoFeNCs of different sizes (8 ± 1 nm, 11 ± 1 nm, 14 ± 2 nm, 15 ± 2 nm). Each sample was concentrated at 2g/L. The loops were taken at three different fields (8-16-24 kA/m) and four frequency (50-100-200-300 kHz).

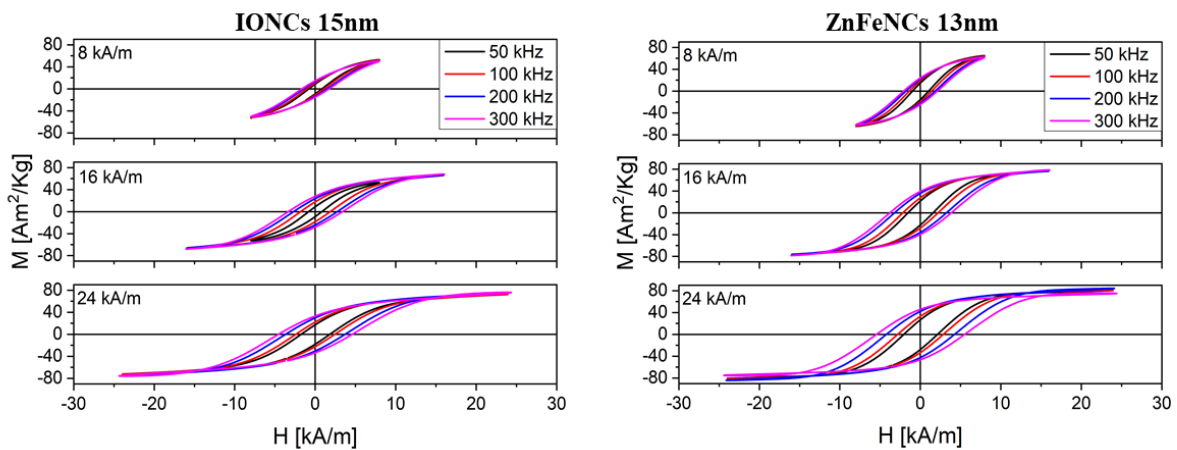


Figure A6 Experimentally measured AC Hysteresis loops for IONCs (15 ± 1 nm) and ZnFeNCs (13 ± 1 nm). Both samples were concentrated at 2g/L. The loops were taken at three different fields (8-16-24 kA/m) and four frequency (50-100-200-300 kHz).

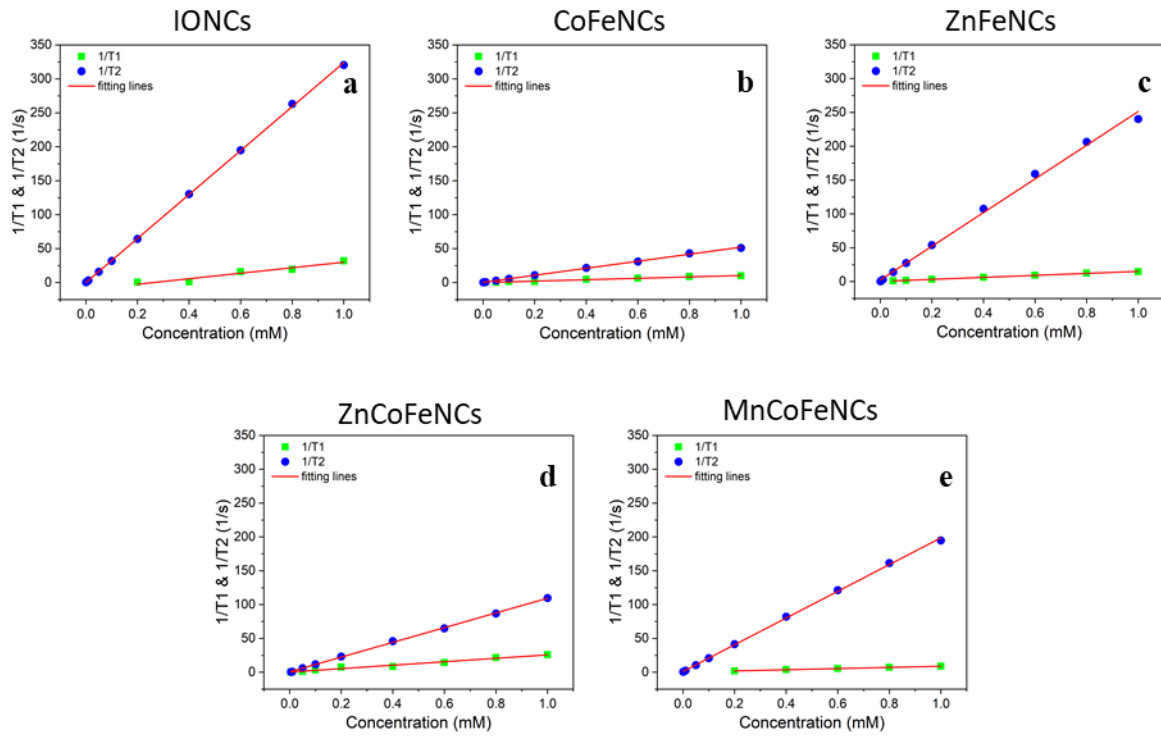


Figure A7 Experimentally measured longitudinal and transverse relaxation rates and the corresponding calculated regression slopes for the different ferrite NCs at 0.5T, varying the NPs concentration. **a)** IONCs 14 ± 2 nm, **b)** CoFeNCs 9 ± 1 nm, **c)** ZnFeNCs 12 ± 1 nm, **d)** ZnCoFeNCs 12 ± 1 nm, **e)** MnCoFeNCs 15 ± 4 nm.

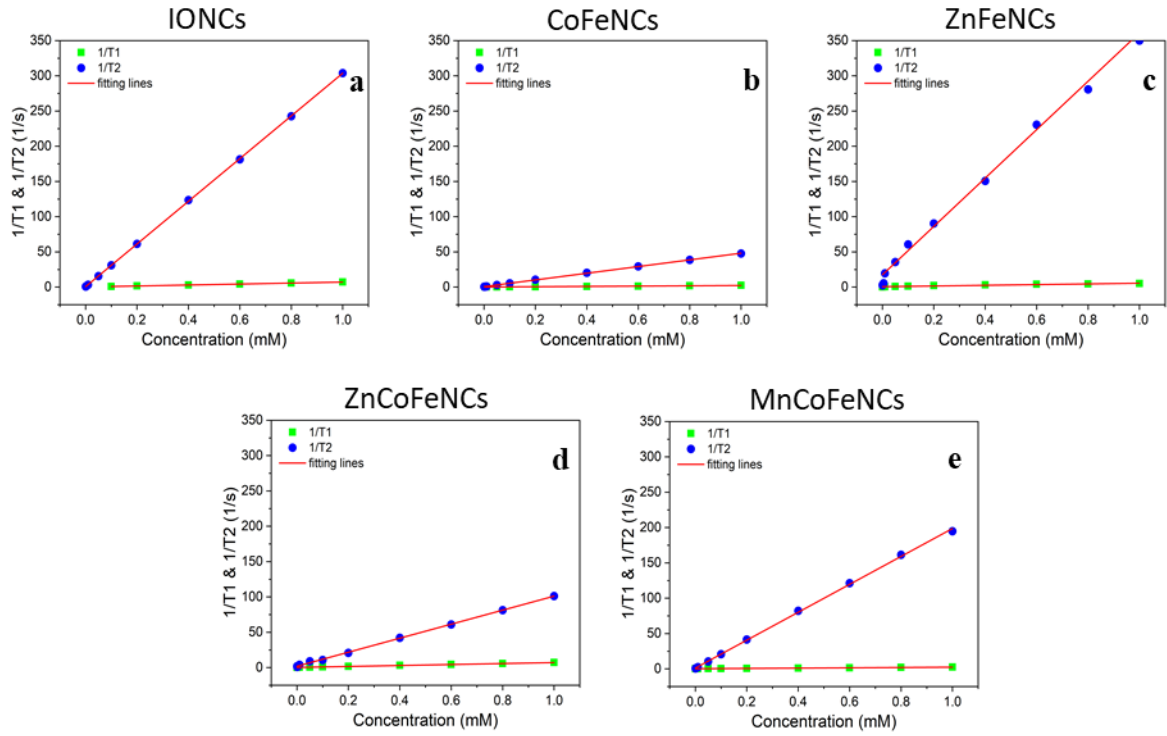


Figure A8 Experimentally measured longitudinal and transverse relaxation rates and the corresponding calculated regression slopes for the different ferrite NCs at 1.5T, varying the NPs concentration. **a)** IONCs 14 ± 2 nm, **b)** CoFeNCs 9 ± 1 nm, **c)** ZnFeNCs 12 ± 1 nm, **d)** ZnCoFeNCs 12 ± 1 nm, **e)** MnCoFeNCs 15 ± 4 nm.

List of abbreviations

| | |
|-----------|---|
| A β | Amyloid β |
| ACHLs | AC hysteresis loops |
| AD | Alzheimer's disease |
| AMF | alternating magnetic field |
| BBB | blood brain barrier |
| bEnd3 | mouse brain endothelial cell line |
| CoFeNCs | cobalt ferrite nanocubes |
| CNS | central nervous system |
| Dh | hydrodynamic diameter |
| DLS | dynamic light scattering |
| DMEM | Dulbecco's modified eagle's medium |
| EDC | 1-ethyl-3-(3-dimethylaminopropyl)carbodiimide hydrochloride |
| FA | ferulic acid |
| FBS | fetal bovine serum |
| FDA | food and drug administration |
| FFR | field free region |
| FOV | field of view |
| FWHM | full width at half maximum |

| | |
|-----------|--|
| GL261 | mouse glioblastoma cells |
| HL | hysteresis loop |
| HRTEM | high resolution transmission electron microscopy |
| ICP | inductively coupled plasma |
| IONCs | iron oxide nanocubes |
| IONPs | iron oxide nanoparticles |
| LSI | linear and shift invariant |
| MHT | magnetic hyperthermia treatment |
| MnFeNCs | manganese ferrite nanocubes |
| MnCoFeNCs | manganese-cobalt ferrite nanocubes |
| MNBs | magnetic nanobeads |
| MNCs | magnetic nanocubes |
| MNPs | magnetic nanoparticles |
| MPI | magnetic particle imaging |
| MPS | magnetic particles spectrometry |
| MRI | magnetic resonance imaging |
| NCs | nanocubes |
| NPs | nanoparticles |
| PBS | phosphate buffer saline |
| PDI | polydispersity index |

| | |
|----------|---|
| PEG | poly(ethylene) glycol |
| PMAO | poly(maleic anhydride- <i>alt</i> -1-octadecene) |
| PP | passive passage |
| PSF | point spread function |
| PS | penicillin streptomycin |
| RDI | reference daily intake |
| Rf | radio frequency |
| ROS | reactive oxygen species |
| RT | room temperature |
| SAR | specific absorption rate |
| SNR | signal to noise ratio |
| SQUID | superconducting quantum interference device |
| STEM-EDS | X-ray spectroscopy in scanning transmission electron microscopy |
| TAT | trans-activating transcriptional activator peptide |
| TBE | tris-borate-EDTA |
| TEM | transmission electron microscopy |
| TEER | trans-endothelial electrical resistance |
| THF | tetrahydrofuran |
| TJ | tight junction |
| XRD | X-ray diffraction |

| | |
|-----------|-------------------------------|
| ZnFeNCs | zinc ferrite nanocubes |
| ZnCoFeNCs | zinc-cobalt ferrite nanocubes |
| ZP | zeta potential |

Acknowledgements

I would like to show my gratitude to everyone that somehow contributed or made part of this work.

First of all, for the guidance and the supervising during my PhD at IIT, I thank my supervisor Dr. Teresa Pellegrino. I am thankful also for her support and encouragement for all the collaboration I did abroad.

For helping me during this three years to develop the herein project presented and made me love science, I would like to thank Dr. Soraia Fernandes, Dr. Tommaso Avellini, Dr. Markus Barthel, Dr. Alberto Curcio.

For proofreading any part of this thesis, I am grateful to Dr. Soraia Fernandes and Dr. Pablo Guardia.

For providing me the insulin fibrils and for the fruitful discussions, I am grateful to Prof. Annalisa Relini. For the measurements on my samples and for introducing me to the interesting world of MPI, I would like to thank Prof. Anna Cristina Samia. I am grateful to Dr. Francisco Teran for the precious advices and the nice discussions. I would like also to thank Dr. Mattia Bramini for teaching me how to culture an in-vitro BBB model, Dr. Soraia Fernandes, for the FACS measurements, Dr. Tiziano Catelani, for the precious TEM images of the cells, Rosaria Brescia for the HRTEM images and STEM-EDS analysis, Dr. Pablo Guardia and Sergio Fiorito, for the SQUID and XRD measurements and Filippo Drago for the ICP-AES analysis.

A huge thanks goes to my colleagues Sahitya Kumar Avugadda (the free bird), Gabriele La Rosa, , Helena Gavilan Rubio, Emille Martinazzo Rodriguez, Tamara Fernandez Cabada, Than Binh Mai, Pablo Guardia and Francesco De Donato, for their support and their help. They are not only colleagues but also good friends.

A special thanks goes to the group “gordinho che dorme”, Soraia Fernandes (the boss), Sergio Fiorito, Simone Nitti (he showed me the “way” of the cubes), Marco Cassani, Giammarino Puglese and Filippo drago, they made my everyday life fun.

I want to say thanks to all the IIT friends, in particular to Federico, Lea, Carmine, Graziella, Luca, Menjiao, Alberto, Marco, Iulia and Dimitry.

I would like to express a really special thanks to my beloved wife Marta. She always supports me in my decisions and makes my life worth living. I can not express how big is my gratitude for her. She is my shining sun on a cold day.

Last but not the least, I would like to thank my family:

my parents Andrea and Cinzia for providing me with unfailing support and continuous encouragement throughout my years of study. I always knew that you believed in me and wanted the best for me.

my father in law Andrea, my mother in law Nicoletta and my sister in law Alessandra for their love and moral support.

Curriculum vitae

Name NICCOLO' SILVESTRI
E-mail niccolo.silvestri@gmail.com
Nationality Italian
Date of Birth 30/11/1988

EDUCATION

2015 - present **PhD in Nanochemistry.**
Istituto Italiano di Tecnologia (IIT), Genoa, Italy
Department: Nanomaterials for Biomedical applications,
Project: "Magnetic nanoparticles for brain diseases".
Supervisor: Dr. Teresa Pellegrino

2012 -2015 **Master's degree in Rehabilitation engineering and biomaterials.**
University of Genoa, Genoa, Italy
Thesis: " *Functionalization of superparamagnetic nanoparticles for therapeutic treatment of tumors and neurodegenerative disorders*"
Supervisors: Dr. Teresa Pellegrino (IIT, D3), Dr Alessia Petrelli (IIT,D3), Prof. Carmelina Ruggiero (University of Genoa, Dibris),

2007-2013 **Bachelor's degree in Biomedical Engineering.**
University of Genoa, Genoa, Italy
Thesis: " *Study of a biomechanical model of postural stability*"
Supervisor: Prof. Giovanni Battista Rossi(*University of Genoa, Dimec*).

RESEARCH EXPERIENCE

From 9January2018 to 23January2018 **iMdea Nanoscience center, Madrid, Spain**
Cost Action TD1402
Department: Magnetic nanoparticles for biomedical applications.
– Magnetic characterization of nanoparticles.

From July 2017 to September 2017 **Lawrence Berkeley National Laboratory, Berkeley, California, USA**
Marie Curie Action, Compass Project
Department: Molecular Foundry – Inorganic Facility.
– Synthesis of Upconverting nanoparticles.
– Magnetic Nanobeads production

From November 2015 to present **Istituto Italiano di Tecnologia (IIT), Genoa, Italy**
Department: Nanomaterials for Biomedicals.
– Synthesis of magnetic nanoparticles for drug delivery to brain for brain disease.
– Nanoparticles functionalization
– Study of Blood Brain Barrier *in-vitro*

From April 2015 to September 2015 **Istituto Italiano di Tecnologia (IIT), Genoa, Italy**
Department: Nanomaterials for Biomedicals.
– Synthesis of magnetic nanoparticles
– Magnetic charcterization

From October 2014 to March 2015 **Istituto Italiano di Tecnologia (IIT), Genoa, Italy**
Department: Nanomaterials for Biomedicals.
– Nanoparticles functionalization with polymers and lipids

From February 2012
to February 2013

University of Genoa, Genoa, Italy

Biomechanics of the human body.

- Mathematical and Finite Element Method model of the human body in standing state.

PUBLICATIONS

1. Sathya, A., Guardia, P., Brescia, R., **Silvestri, N.**, Pugliese, G., Nitti, S., ... & Pellegrino, T. (2016). "*Co_x Fe_{3-x}O₄ Nanocubes for Theranostic Applications: Effect of Cobalt Content and Particle Size*". Chemistry of Materials, 28(6), 1769-1780.
2. Vecchione, R., Quagliariello, V., Giustetto, P., Calabria, D., Sathya, A., Marotta, R., Profeta M, Nitti S, **Silvestri N** ... & Iaffaioli, R. V. (2017). "*Oil/water nano-emulsion loaded with cobalt ferrite oxide nanocubes for photo-acoustic and magnetic resonance dual imaging in cancer: in vitro and preclinical studies*". Nanomedicine: Nanotechnology, Biology and Medicine, 13(1), 275-286.

PRESENTATIONS

Oral presentation, **ICARO ERC Kick off meeting**, Sestri Levante, Italy, 2016.

"Cobalt Ferrite NanoCubes: Synthesis, Characterization, Biocompatibility and some issues on the magnetic hyperthermia measurements".

Oral presentation, **IIT Genova**, October 3, 2016.

"Magnetic nanoparticles for brain disease", IIT Genova, October 3, 2016.

Oral presentation, **Compass project midterm meeting**, Camogli, Italy, September 15, 2017.

"Secondment report: Magnetic Nanobeads preparation with Nimbus".

Oral presentation, **Lawrence Berkeley National Laboratory**, Berkeley, USA, August 18, 2017.

"Different Ferrite Nanocubes for Theranostic Applications: Synthesis, SAR Characterization and Nanobeads Formation".

Oral presentation, 15th **International conference on Nanoscience & Nanotechnologies (NN18)**, Thessaloniki, Greece, 5 July 2018. "Tuning the size and the composition of ferrite nanocubes towards outstanding hyperthermia performances"

Poster presentation, 12th **International Summer schools "N&N: Organic Electronics & Nanomedicine" (ISSON18)**, 30 June-7 July 2018, Thessaloniki, Greece

"Tuning the size and the composition of ferrite nanocubes towards outstanding hyperthermia performances" (**awarded for best poster presentation**)

REFERENCES

Dr. Teresa Pellegrino

Istituto Italiano di Tecnologia (IIT) Via Morego 30, 16163 Genova, Italy.

Email: teresa.pellegrino@iit.it

Prof. Liberato Manna

Istituto Italiano di Tecnologia (IIT) Via Morego 30, 16163 Genova, Italy.

Email: liberato.manna@iit.it